12-2020

Synchronized measurement data conditioning and real-time applications

Xianda Deng
University of Tennessee, Knoxville, xdeng6@vols.utk.edu

To the Graduate Council:

I am submitting herewith a dissertation written by Xianda Deng entitled "Synchronized measurement data conditioning and real-time applications." I have examined the final electronic copy of this dissertation for form and content and recommend that it be accepted in partial fulfillment of the requirements for the degree of Doctor of Philosophy, with a major in Electrical Engineering.

Yilu Liu, Major Professor

We have read this dissertation and recommend its acceptance:

Hairong Qi, Fangxing Li, Di Shi

Accepted for the Council:

Dixie L. Thompson

Vice Provost and Dean of the Graduate School

(Original signatures are on file with official student records.)

Synchronized measurement data conditioning and real-time applications

A Dissertation Presented for the

Doctor of Philosophy

Degree

The University of Tennessee, Knoxville

Xianda Deng

December 2020

To my beloved Victor Deng and Hannah Deng.

ACKNOWLEDGEMENTS

It was a rough journey. I am grateful to my advisor, Dr. Yilu Liu for her guidance and support. I would like to thank everyone who has helped me on this journey.

ABSTRACT

Phasor measurement units (PMU), measuring voltage and current phasor with synchronized timestamps, is the fundamental component in wide-area monitoring systems (WAMS) and reveals complex dynamic behaviors of large power systems. The synchronized measurements collected from power grid may degrade due to many factors and impacts of the distorted synchronized measurement data are significant to WAMS. This dissertation focus on developing and improving applications with distorted synchronized measurements from power grid. The contributions of this dissertation are summarized below.

In Chapter 2, synchronized frequency measurements of 13 power grids over the world, including both mainland and island systems, are retrieved from Frequency Monitoring Network (FNET/GridEye) and the statistical analysis of the typical power grids are presented. The probability functions of the power grid frequency based on the measurements are calculated and categorized.

Developments of generation trip/load shedding and line outage events detection and localization based on high-density PMU measurements are investigated in Chapters 3 and 4 respectively. Four different types of abnormal synchronized measurements are identified from the PMU measurements of a power grid. The impacts of the abnormal synchronized measurements on generation trip/load shedding events detection and localization are evaluated. A line outage localization method based on power flow measurements is proposed to improve the accuracy of line outage events location estimation.

A deep learning model is developed to detect abnormal synchronized measurements in Chapter 5. The performance of the model is evaluated with abnormal synchronized measurements from a power grid under normal operation status. Some types of abnormal

synchronized measurements in the testing cases are recently observed and reported. An extensive study of hyper-parameters in the model is conducted and evaluation metrics of the model performance are presented.

A non-contact synchronized measurements study using electric field strength is investigated in Chapter 6. The theoretical foundation and equation derivations are presented. The calculation process for a single circuit AC transmission line and a double circuit AC transmission line are derived. The derived method is implemented with Matlab and tested in simulation cases.

TABLE OF CONTENTS

LIST OF TABLES

LIST OF FIGURES

Chapter 1 Introduction

1.1 Synchrophasor measurement and frequency monitoring network

The modern power grid is the most complicated artificial system, which has been evolving in recent decades with various technologies [1]-[3]. Meanwhile, renewable energy sources have been promoting and integrated into power grids in recent years [4], [5]. Power grid structures and dynamic behaviors are becoming more complex, due to the flexibility from the new technologies and fluctuating nature of renewable energy sources [6], [7]. The changes bring challenges to the traditional power grid monitoring and management system, the supervisory control and data acquisition system (SCADA) and energy management systems (EMS) [3]. Wide-area monitoring systems (WAMS), consists of advanced measurement technology, information tools, and operational infrastructure that facilitate the understanding and management of the increasingly complex behavior exhibited by large power systems [8]. With real-time, global positioning system (GPS) time-synchronized measurements at high data rates, WAMS reveals unprecedented insights into power grid dynamics and will be the next-generation operational-management systems [3], [9]-[11]. Phasor measurement units (PMU), measuring voltage and current phasor with synchronized timestamps, are the fundamental components in WAMS [3], [12].

Frequency Monitoring Network(FNET/ GridEye), a pilot of WAMS, consisted of hundreds of low-cost and high-accuracy GPS synchronized sensors worldwide. The server of FNET/GridEye is located at the University of Tennessee. The details of FNET/GridEye architecture and synchronized measurement sensors are introduced in Chapter 2.3. Around 200 synchronized measurement sensors are deployed at Eastern interconnection (EI), Western Electricity

Coordinating Council (WECC) and Electric Reliability Council of Texas (ERCOT) in U.S., which are shown in Fig. 1.1. The synchronized measurement sensors have been collecting frequency and angle measurements and streaming them to the server at UTK for real-time applications or post-event analysis. The frequency and angle visualization at FNET/GridEye are shown in Fig. 1.2 and 1.3 respectively.

Numerous real-time synchronized measurement applications have been developed based on FNET/GridEye. FNET/GridEye has been successfully operating and monitoring interconnections in the U.S. for more than a decade. One of the major real-time applications on FNET/GridEye is events detection and location estimation. The real-time applications have detected and located more than 1000 events, which are confirmed by utilities, in the U.S.. The algorithm and successful experience of real-time events detection applications on FNET/GridEye are reported on the top journals and conferences in IEEE and filed for patents in the U.S.. The detected event results of two typical real-time applications on FNET/GridEye: generation trip events detection and islanding events detection are shown in Fig. 1.4 and 1.5.

1.2 High-density synchrophasor measurements and issues

As one of the core technologies for the next-generation energy management system, synchrophasor technology has been prompting in industry and more PMUs are deployed in the power grid. This change brings both challenges and opportunity of existing real-time events detection and location applications based on synchronized measurements in two aspects:

(1). High density of synchrophasor measurements

The most existing reported algorithms and applications of events detection based on synchrophasor measurements are tested or demonstrated with limited numbers of PMUs [13]-[20]. However, it has been reported that around 400 PMUs have been installed in a power grid,

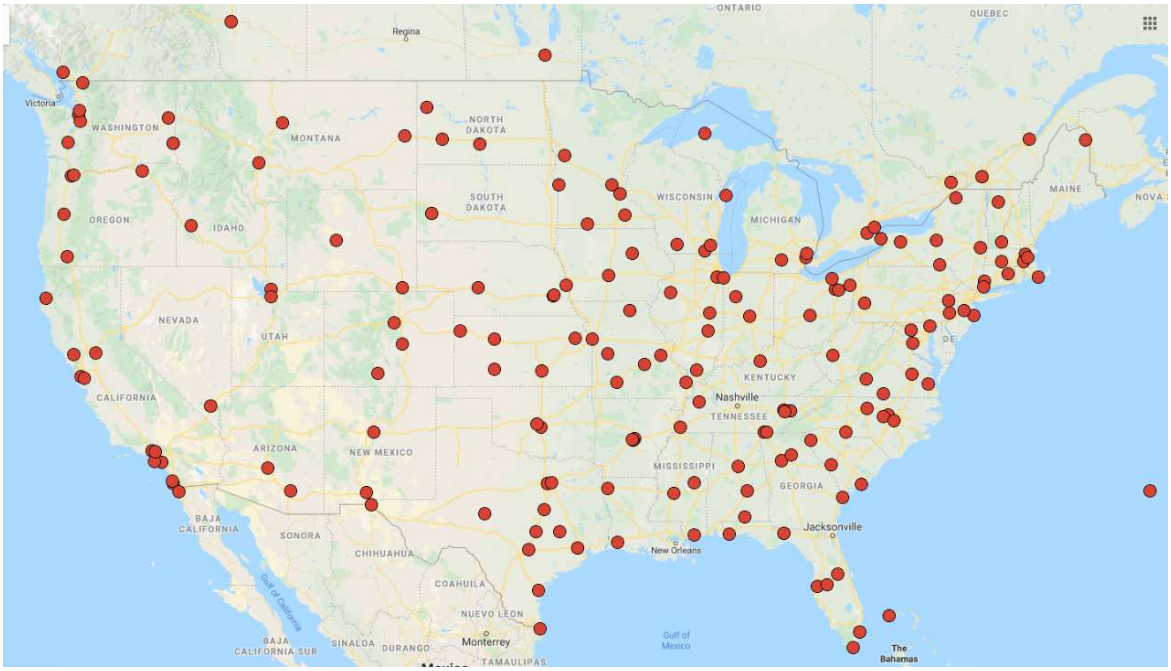

Figure 1.1. FNET/GridEye synchronized measurement sensors deployment map in U.S.

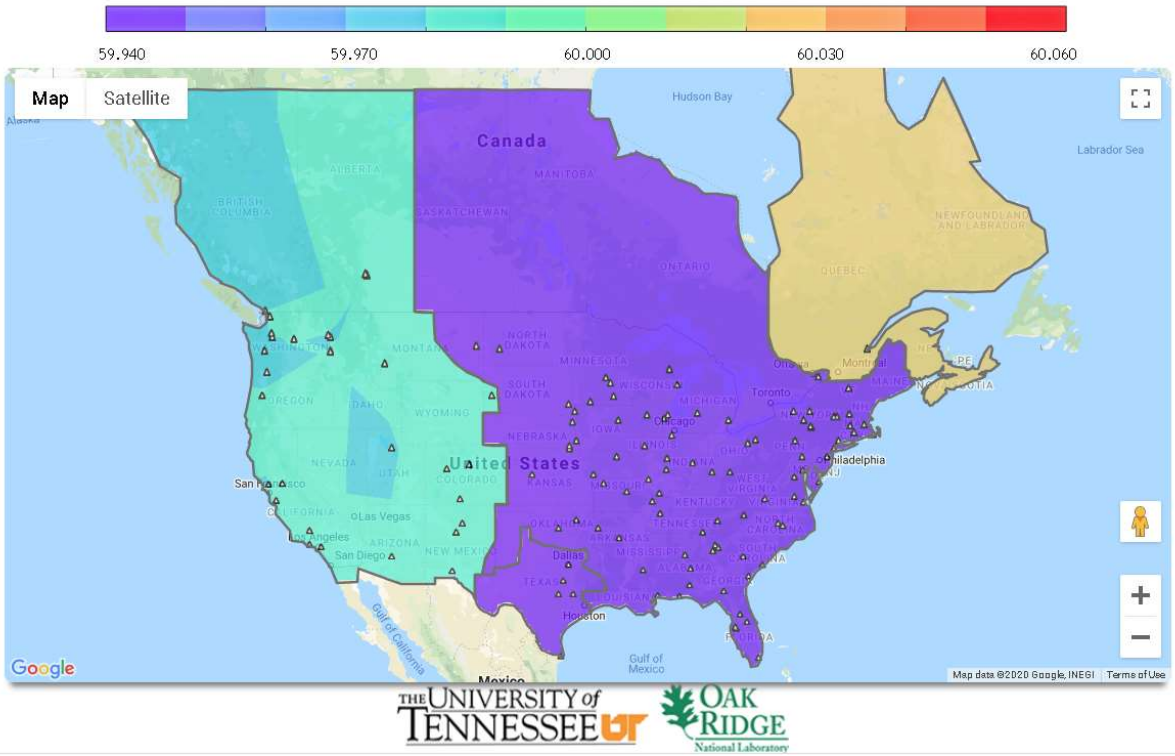

Figure 1.2. FNET/GridEye real-time frequency visualization in U.S.

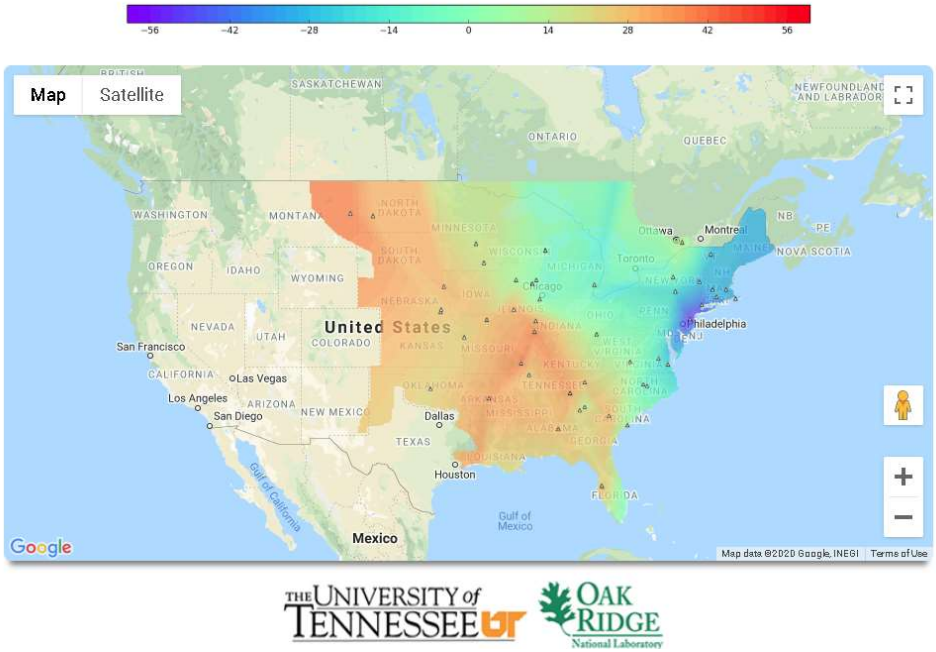

Figure 1.3. FNET/GridEye real-time frequency visualization in EI system.

Basic Event Information

Event Date	Event Time	Event Type	Estimated Amount
2020-01-31	23:36:00 UTC	Generation Trip	560 MW
Point A	Point B	Point C	Point C Prime
59.9787 Hz	59.9639 Hz	59.9545 Hz	N/A Hz
MOD-027-1 Event	Inter Connection	Estimated Reliability Coordinator	ROCOF
NO	EI	RFC	N/A
Estimated Event Location		Additional Location Information	
(39.2097, -77.4644)		near Dickerson power plant (RFC) in (Dickerson,MD,20842).	

*Due to limited knowledge on WECC and ERCOT, the magnitude estimation may not be accurate. Please verify it before use.

Location Map

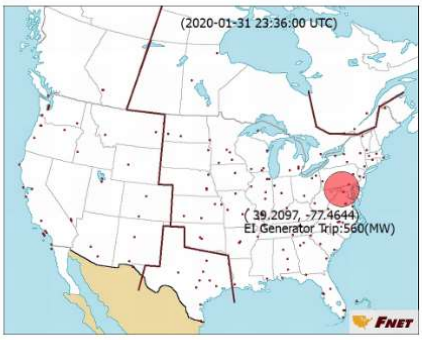

Frequency Plot of All FDRs

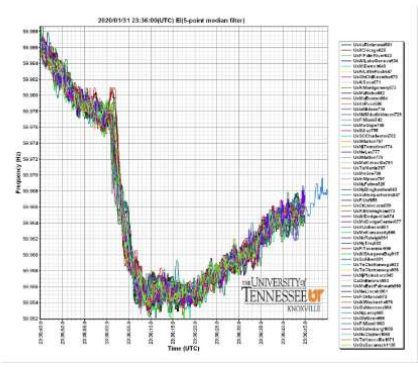

Figure 1.4. A Generation trip event detection and location report from FNET/GridEye

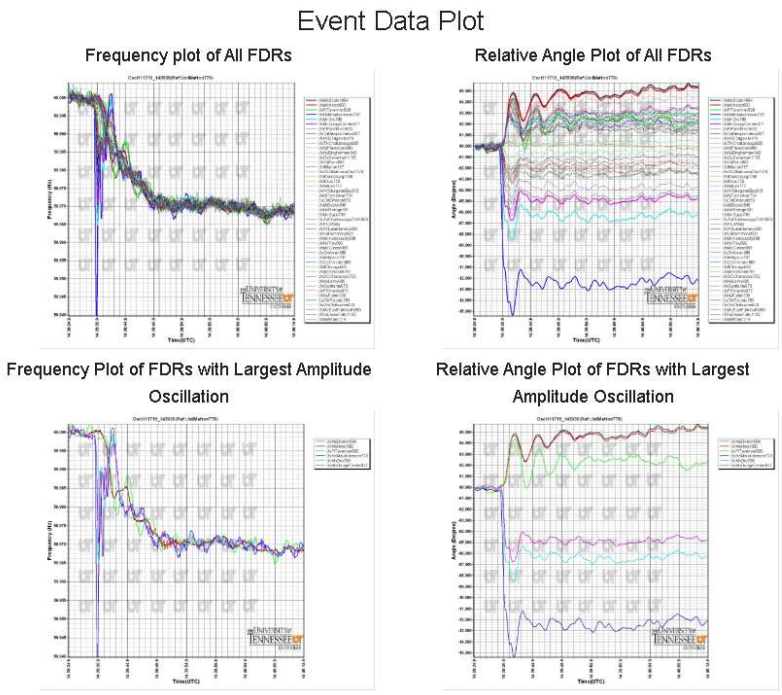

Figure 1.5. An oscillation event detection report from FNET/GridEye

which covers only one province territory in China [21]. The huge volume of high-resolution measurements brings high computation burdens to real-time applications. Additionally, the deployment of PMU in such a relatively small area also questions the validity of the existing real-time applications. The traditional method of locating events without system parameters is based on disturbance propagation speed difference or disturbance magnitude. The assumptions were made based on several synchrophasor measurements are deployed in a large area [22]-[24].

(2). Data quality issue

In operating power gird, communication failure, hardware malfunction and inappropriate configuration of PMUs may cause data quality issues in PMU measurement. Several papers have been published about recovering data quality issues in PMU measurements and improving robust algorithms with low data quality PMU measurements [25]-[31]. However, the common types of PMU measurement anomalies in the papers are random spikes and missing data. The patterns of PMU measurement anomalies from operation power gird are more sophisticated and some new types of PMU measurement anomalies are recently reported [21]. The impacts of the PMU measurement anomalies on the existing algorithms and applications have not been evaluated. Additionally, the method of detecting and classifying the recently reported anomalies is not developed.

1.3 Organization of study

This dissertation focus on different aspects of synchrophasor measurements of data conditioning and its real-time applications. The rest of the dissertation is organized as follows:

Chapter 2 presents an observation and statistical study of power grid frequency operation status worldwide with synchrophasor measurements from FNET/GridEye system. The typical

power grids at the mainland and island in four continents are analyzed. The distributions of the power grid operation frequency are calculated and categorized.

Chapter 3 presents a real-time generation trip and load shedding events detections application for a power grid with a high density of PMU deployment. New types of PMU measurement anomalies from field measurements are reported. The implementation is tested with simulation event cases, ambient cases and a generation trip event. The impacts of PMU measurement anomalies on the implementations are evaluated.

Chapter 4 proposed a line outage event location estimation method based on power flow measurements. The proposed method based on power flow distribution factor is analyzed and validated with TVA and ISO-NE system in simulation. The proposed is implemented and tested with ISO-NE system in comprehensive study simulations. A comparison between the proposed method and traditional methods without system parameters indicates the improvement of location estimation accuracy.

Chapter 5 proposed a deep learning method to identify data quality issues. Four types of data anomalies are identified in PMU frequency measurements collecting from power grid. The training and testing sample sets are created and labeled from ambient measurements from a power grid. Hyper-parameters in the proposed structure are evaluated by a tentative study. The performance of the proposed structure is demonstrated with high accuracy results and evaluation metrics.

Chapter 6 proposes a method to calculate AC transmission line voltage via electric field strength. The equations and calculation processes are derived for both single circuit and double circuit transmission lines. Electric field strength distribution of a single circuit and double circuit

transmission line from a textbook are reproduced and used to validate the derived equation and methods.

Chapter 2 Frequency Observations and Statistic Analysis of Worldwide Main Power Grids Using FNET/GridEye

2.1 Background and motivation

Renewable energy sources have been promoted all over the world in recent years, due to its clean, low-cost and inexhaustible features, compared to the traditional power generation [4]-[5]. Meanwhile, the intermittent and unpredictable natures of renewable energy sources enhance the system frequency fluctuation, which brings challenges to power system operations and grid security [32]-[36]. Numerous factors determine power grid power frequency deviation [37], e.g. system capacity, load types, regulation requirements, power imbalance and etc. To maintain the system stability and meet system frequency regulation, more reserve power sources are required to accommodate the increasing renewable energy sources in the power grids. To compromise between stability risks and expensive cost of reserve power, research has been conducted to develop new control strategies and reserve sizing techniques [37]-[39]. In another direction, some researchers proposed that a flexible frequency operation strategy would satisfy load demands with limited reserve power sources [40]. It is noticed that although many studies have been contributed into moderating the problem, there are few observations and reports about what are the present power frequency status and frequency fluctuation ranges of worldwide power grids [41]-[43]. Power frequency deviation varies in different power grids, especially for the grids on small islands. Hence, it is worthwhile to investigate the power frequency status in worldwide major power grids and what are power frequency differences between the mainland and island.

Wide-area monitoring systems (WAMS), consisting of advanced measurement technology, information tools, and operational infrastructure, facilitates the understanding and management

of the increasingly complex behavior exhibited by large power systems [44]. With the real-time, global positioning system (GPS) time-synchronized measurements at high data rates, WAMS reveals unprecedented insights into power grid dynamics and will be the next-generation operational-management systems [45]-[49]. However, the worldwide WAMS systems have not been built yet, let alone the frequency observations for the worldwide power systems.

FNET/GridEye, a kind of wide-area measurement system (WAMS), has been developed and operated over decades [47]. Hundreds of frequency disturbance recorders (FDR) are installed over the world, which is sending high time resolution measurements to FNET/GridEye servers. The FNET/GridEye servers are located at the University of Tennessee, Knoxville (UTK) and Oak Ridge National Laboratory (ORNL). With the valuable measurements, FNET/GridEye, as an independent observer, observes power grid operation frequency status in different regions over the world [47]. Based on measurements from FNET/GridEye, static analysis of the power system frequency and rate of change of frequency (ROCOF) in different power grid have been published and provided guidance in different research areas [41]-[43]. In this chapter, the frequency data of worldwide major mainland and island power grids are analyzed and studied from the view of statistics, based on FNET/GridEye measurements

Though research has been conducted on studying the power frequency in the actual power grids, a few papers reported the power frequency in the worldwide main power grids, and thus the insights for the worldwide power system frequency are seldom offered. Using the data from FDRs, this paper offers a statistical analysis of the frequency in the different regions, which is helpful for the frequency study.

2.2 Review of power system frequency recommendations and regulations

System frequency deviation may impact major components in power system and must be regulated in a limited range. Various frequency limits and thresholds are specified or recommended in standards or utility operation regulations. In this section, frequency requirements and recommendations at normal operation for different components in power system are reviewed and summarized.

(1). Under frequency load shedding (UFLS)

In [50], The North American Electric Reliability Corporation (NERC) specifies automatic UFLS schema requirements to arrest frequency decline. It requires a minimum of three frequency set points in UFLS schema. For the highest setting of the setting is

$$59.3 \text{ Hz} \leq f_{\text{high}} \leq 59.5 \text{ Hz}$$

For the lowest setting of the setting is

$$58.4 \text{ Hz} \leq f_{\text{min}}$$

The interval between the setting points is

$$0.2 \text{ Hz} \leq f_{\text{interval}} \leq 0.5 \text{ Hz}$$

In [51] NERC defines real power balancing control performance to regulate interconnection operation frequency in North America. It specifies both high and low balancing authority ACE limits for different interconnections in North America and requires balance authorities operates within the limits. Balancing authority ACE limits are determined by frequency trigger limits. The frequency trigger limits (FTLs) are calculated by

$$\boldsymbol{FTLs} = \text{Fs} - 3\varepsilon_{1I} \tag{2.1}$$

Fs is the scheduled frequency in Hz. ε_{1I} is the constant derived from a targeted frequency bound for each Interconnection land derived from data samples over a given year [50]-[51]. Scheduled frequency, ε_{1I} and FTLs specified by NERC are summarized in Table 2.1.

(2). Voltage quality and frequency regulation

Power system frequency status and deviation may result in power quality degradation and bring potential unstable issues to power system operations. Certain types of loads may be vulnerable to the power quality and hazards and losses may occur under power quality degradation. IEEE standards specify susceptive load, which may also be referred as sensitive load, in various areas and define the tolerated frequency of the susceptive load. In [52], susceptive load mainly focuses on (1). Data processing equipment and (2). Life safety and life support systems. The applications of data processing equipment are categorized for both industrial and commercial classifications. The detailed information of the data processing equipment is described and available at [52]. The susceptible loads discussed in the standard [53] include (1). Computers, (2). Process control, (3). Telecommunications, (4). Electric arc lighting and (5). Consumer electronics. Additional, power system operation frequency limits are critical to power system stability and reliability. Utilities define their own frequency regulation requirements to specify power system operation frequency arranges under different circumstances. The major IEEE standard recommendations and frequency regulation from utilities are reviewed and summarized in Table 2.2.

(2). Power generation

The main concern about power system frequency at power plants is its impacts on gas and steam turbine prime movers. Torsional vibration, which causes mechanical damage, may happen when gas and steam turbine operate at off-nominal speeds and are resonant with power

Table 2.1 Targeted frequency bound constant of interconnections in North America

Interconnection	ε1(Hz)	FTL_{Low} (Hz)	F_S(Hz)
Eastern Interconnection	0.018	59.928	59.982
Western Interconnection	0.0228	59.9088	59.9772
ERCOT Interconnection	0.030	59.88	59.97
Quebec Interconnection	0.021	59.916	59.979

Table 2.2. Frequency recommendation and regulations

Standards	Frequency	ROCOF	Description
IEEE Std 446 [52]	±0.5 Hz	1 Hz/s	The standards listed types of sensitive loads in industry.
IEEE Std 1250 [53]	±0.5 Hz	1 Hz/s	Reference IEEE Std 446
IEEE Std 1250 [53] (expectations)	±0.015 Hz	NA	Voltage quality performance expectations, which are based on typical steady-state maximum frequency deviation in an interconnected power system in North America.
IEEE1100 [54]	±0.5%	0.3 Hz/s	0.3 Hz for 60 Hz Systems and 0.25 Hz for 50 Hz systems

Table 2.2 continued

Standards	Frequency	ROCOF	Description
GB/T 15945 [55]	± 0.2 Hz	NA	Frequency regulation in China. Frequency limits are relaxed to ± 0.5 Hz when the system capacity is small.
AEMS FOS [56] (Mainland)	± 0.15 Hz	NA	Australia frequency operating standard
AEMS FOS[56] (island)	± 0.5 Hz	NA	Australia frequency operating standard
AEMS FOS [56] (Mainland – during supply scarcity)	± 0.5 Hz	NA	Australia frequency operating standard

system frequency. For generator perspective, International Organization for Standardization (ISO) defines frequency limits for gas and steam turbine regard to mechanical vibration [57]. It is recommended for generator manufacture to meet the standard requirements when generators are tested and installed. The ISO recommendation about generator frequency is summarized in Table 2.3.

2.3 FNET/Grideye overview and observation data preprocessing

FNET/GridEye is the first WAMS system ever designed to be deployed at the distribution level, whose mission is to pioneer and promote the WAMS technologies in electric power utilities [45]-[49]. Data processing, visualizing and analyzing applications have been implemented on the FNET/GridEye system to process near real-time measurements, collected by variable types of FDRs [43]. Up to date, 297 FDRs are deployed in 31 counties across the world. The locations of FNET/GridEye FDR sensor over the world are shown in Fig. 2.1. FDR deployment map demonstrates that the FNET/GridEye could observe the frequencies of worldwide main power grids.

One of the most distinctive features of FNET/GridEye is the employment of low-cost and high-accuracy sensor, installed at the distribution level, which provides the probability to install FDR sensors over the world with low costs. After years of efforts, contributed by PowerIT group at UTK, three generations of FDR with different features have been developed, including smartphone-based FDR, magnetic and electric field based FDR, and universal grid analyzer (UGA) [58]-[60]. A photo of UGA is shown in Fig. 2.2. At present, the sample rate of the FDRs in FNET/GridEye is 10 times per second. The FDRs transmit the nearly real-time data with GPS synchronized timestamp to FNET/GridEye server via the internet.

Table 2.3 summary of ISO torsional frequency exclusion zones [57]

Torsional zone	Frequency Limit
Allowable grid frequency	+2.5%
Field test (full speed, full train)	+3.5%
Full speed shop test	+ 4%
Full speed, factory test data	+5.0%
Primary exclusion	+6.0%

Temperature effect: +1%

Figure 2.1. FDR Worldwide deployment map.

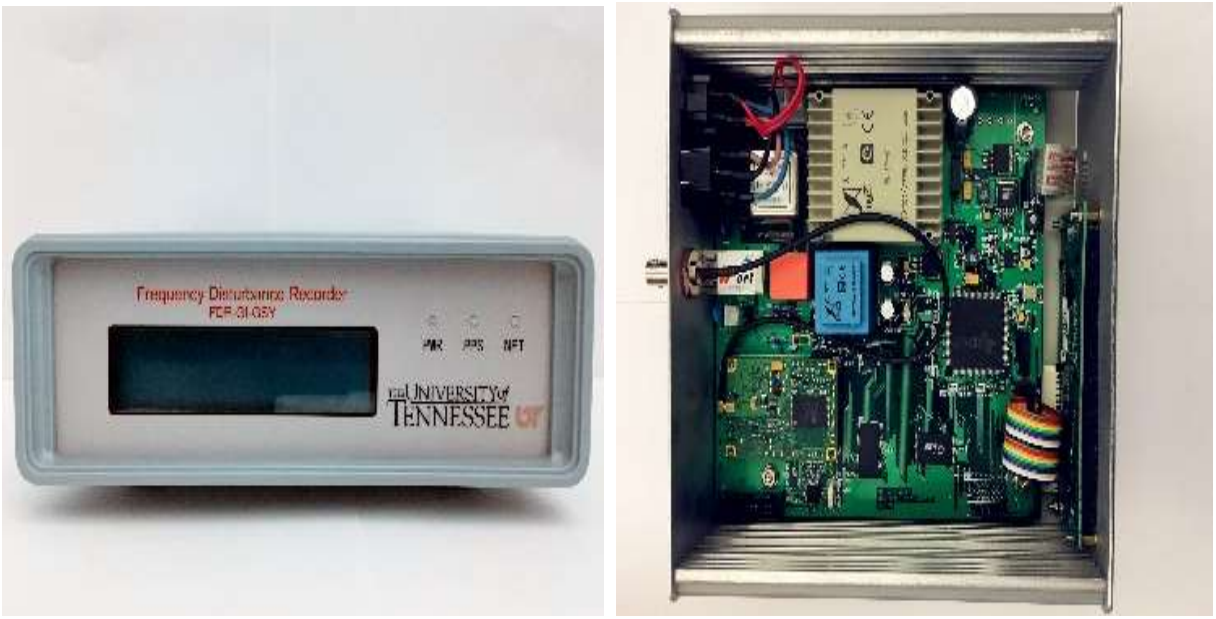

Figure 2.2. The prototype of UGA.

At the FNET/GridEye data center, a data concentrator is employed to receive and process FDR steaming data. After filtering out bad data, all the data are achieved into a database for data analysis [47]. The streaming data is visualized and published at http://fnetpublic.utk.edu/, while historical data is accessible with further privilege authorization. With a vast volume of frequency measurement data collecting over the world, FNET/GridEye provides an opportunity to observe and analyze different power grids frequency status. In the next section, the frequency data collected by FDRs will be analyzed.

For a comprehensive observation purpose, 6 mainland power grids and 7 island power grids, which spread over America, Asia, Europe, Oceania, and Africa, are observed and analyzed in this section. According to [61], [62], frequency in different voltage levels is identical, while frequency differences in different regions of one system are relatively small. Measurements of one FDR in each country is selected for the analysis. The three-month frequency measurement data of the power grids collected by FNET/GridEye are retrieved from the database. The measurement data used in this studied reflect both normal operation and transient status of the power grids.

All the simulations are conducted on a computer running a 64-bit Windows 10, with a 3.60 GHz Intel I7-7700U CPU and 16 GB memory. The sample ratio of FDR is 10 points per second and the studied period is three months, thus the overall volumes of the 13 selected systems measurements data are 9.01 GB. To perform an efficient analysis, R language is employed to implement data processing and analyzing.

The nominal frequencies of the selected power grids include both 50 Hz and 60 Hz, which is shown in TABLE 2.4. Hence, the frequency measurement data are converted to per-unit value (i.e., the unit is p.u.) for a convenient comparing purpose.

Table 2.4 The Operation Frequency of Power Grids Worldwide

Country	Continent	Nominal Frequency (Hz)
EI, U.S.	America	60
WECC, U.S.	America	60
Hawaii, U.S.	America	60
ERCOT, U.S.	America	60
Germany	Europe	50
Saudi Arabia	Asia	60
Japan	Asia	60
Northern Ireland	Europe	50
Ireland	Europe	50
England	Europe	50
Australia	Oceania	50
Bahamas	America	60

To promote repeatability of the simulation, the procedure of the data loading and preprocessing is outlined below and shown in Fig. 2.3.

Step 1: Load historical FDR measurement data files of the studied systems.

Step 2: Align the measurement data with studied periods.

Step 3: Pre-process the measurements and filter bad data.

Step 4: Normalized the measurements of the studied systems.

2.4 Statistical analysis of frequency in power grids

For a specific power grid, the statistic of frequency could reveal some insights into the operation status. Standard deviation and mean of the frequency measurement data are calculated in this paper. The mean of system frequency could be used to show the balance between the generation and the demand. Moreover, the standard deviation of the frequency is offered to demonstrate the frequency fluctuation. It should be noted that some operations in the power grid could also impact on the mean and standard deviation.

As shown in Fig. 2.4, the mean values of frequency in power grids in different regions are listed in descending order. Meanwhile, the standard deviation values of frequency are listed in descending order in Fig. 2.5. As shown in Fig. 2.5, the frequencies in all mainland power grids have smaller standard deviations, comparing to the frequencies in island power grids. One of the potential reasons for this situation is that the sizes of the mainland power grids are larger than the sizes of island power grids. However, it should be noticed that there are some exceptional cases. For Hawaii power grids, its frequency deviation is smaller than those of most mainland power grids. Another extreme case is Egypt power grid, which is located in the mainland, but its frequency deviation is the highest among the power grids studied in this paper.

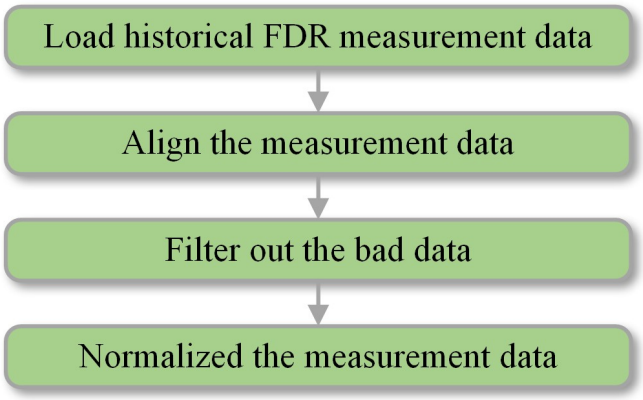

Figure 2.3. The procedure of FDR historical data process and analysis

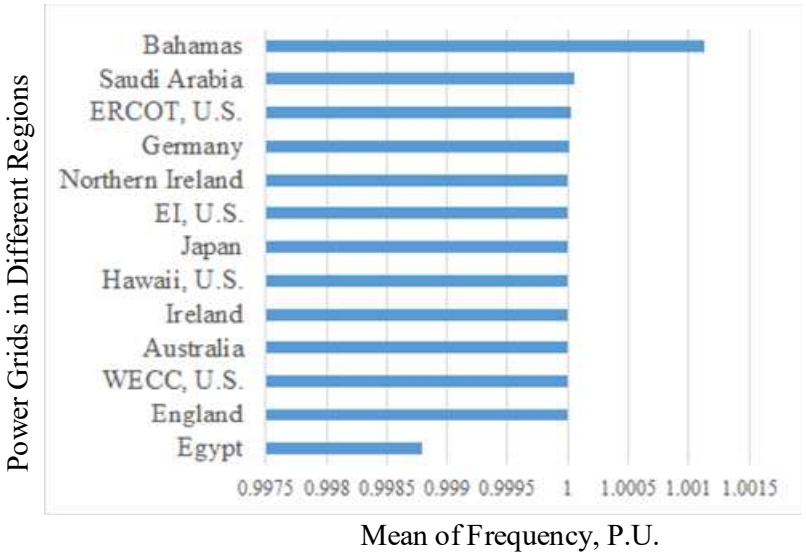

Figure 2.4. Mean of frequency in power grids in different regions

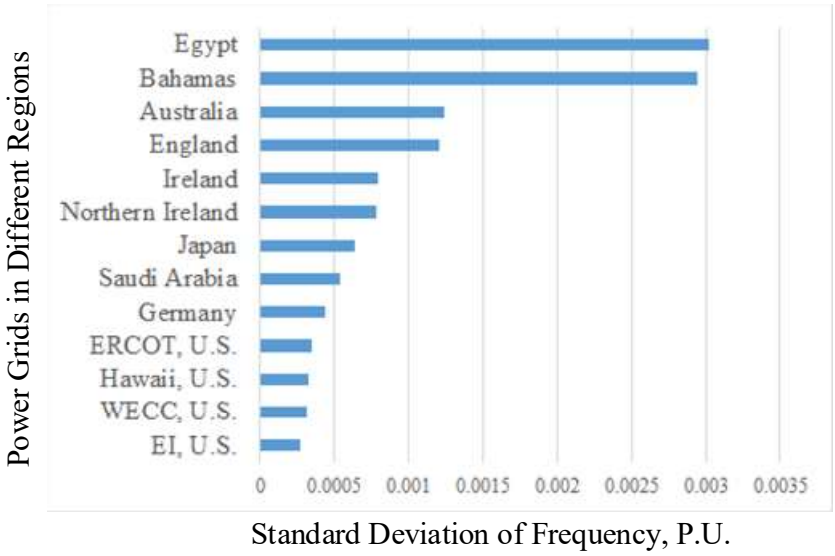

Figure 2.5. The standard deviation of frequency in power grids in different

According to [63], the highest relay setting of load shedding frequency f required by North American Electric Reliability Corporation (NERC) is 59.3 Hz (0.9883333 p.u.) <f<59.5 Hz (0.9916667 p.u.). The measurement data includes transient status, such as generation trip and load shedding events. As shown in Fig. 2.5, most power grids operate with the safe frequency fluctuations in a reasonable margin, comparing to NERC load shedding frequency. However, the frequency standard deviation of Egypt power grid during the observation time in this paper is the highest, which close to the NERC load shedding criteria.

To perform a more detailed statistical analysis, three typical power grids are selected: (1). EI system (North America, mainland power grid), (2). Egypt system (Africa, mainland power grid) and (3). Japan (Asia, island power grid). As shown in Fig. 2.5, there three power grids have the smallest, largest and average standard deviation in the power grids. The standard deviation and mean values of the power grids are calculated for each day. Here, the analysis period is selected as one month. As shown in Fig. 2.6(a), the standard deviation of EI power grid frequency is smallest on a daily basis, compared to Japan and Egypt power grids frequency. Means of daily frequency in Egypt power grid are not a straight line as shown in Fig 2.6(b). It means that Egypt power grids are operated at an under-frequency status. Compared to Egypt power grids frequency mean, the means of daily frequency in EI and Japan power grids are almost flat, which indicates that the two systems are operated steadily around the nominal frequency. Also, the results indicate that the frequency fluctuation in Egypt system is higher than that in EI and Japan power grids.

In the following, the probability density function of the frequency is calculated, which is shown in Fig. 2.7. It can be seen that the probability density functions can divide into two types: 1) single-peak distribution, such as the probability density function of the frequency in EI,

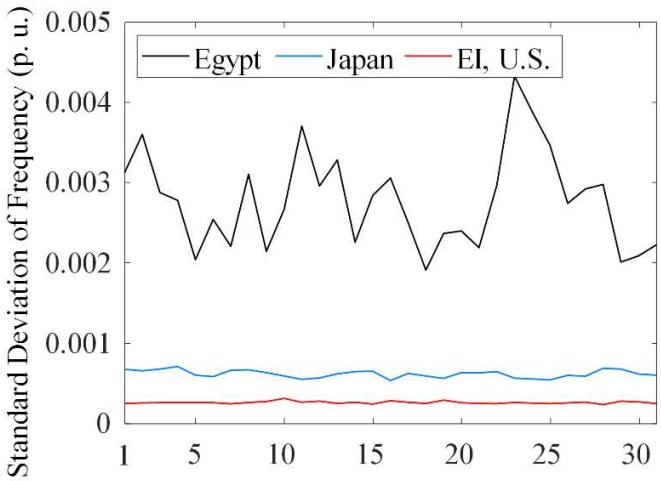

(a)

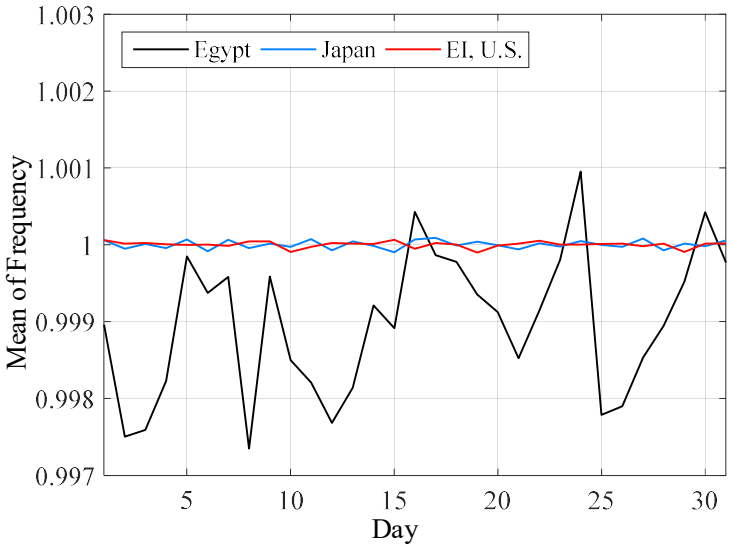

(b)

Figure 2.6. Standard deviation and mean of frequency in each day in three power grids. (a) Standard deviation (b) Mean.

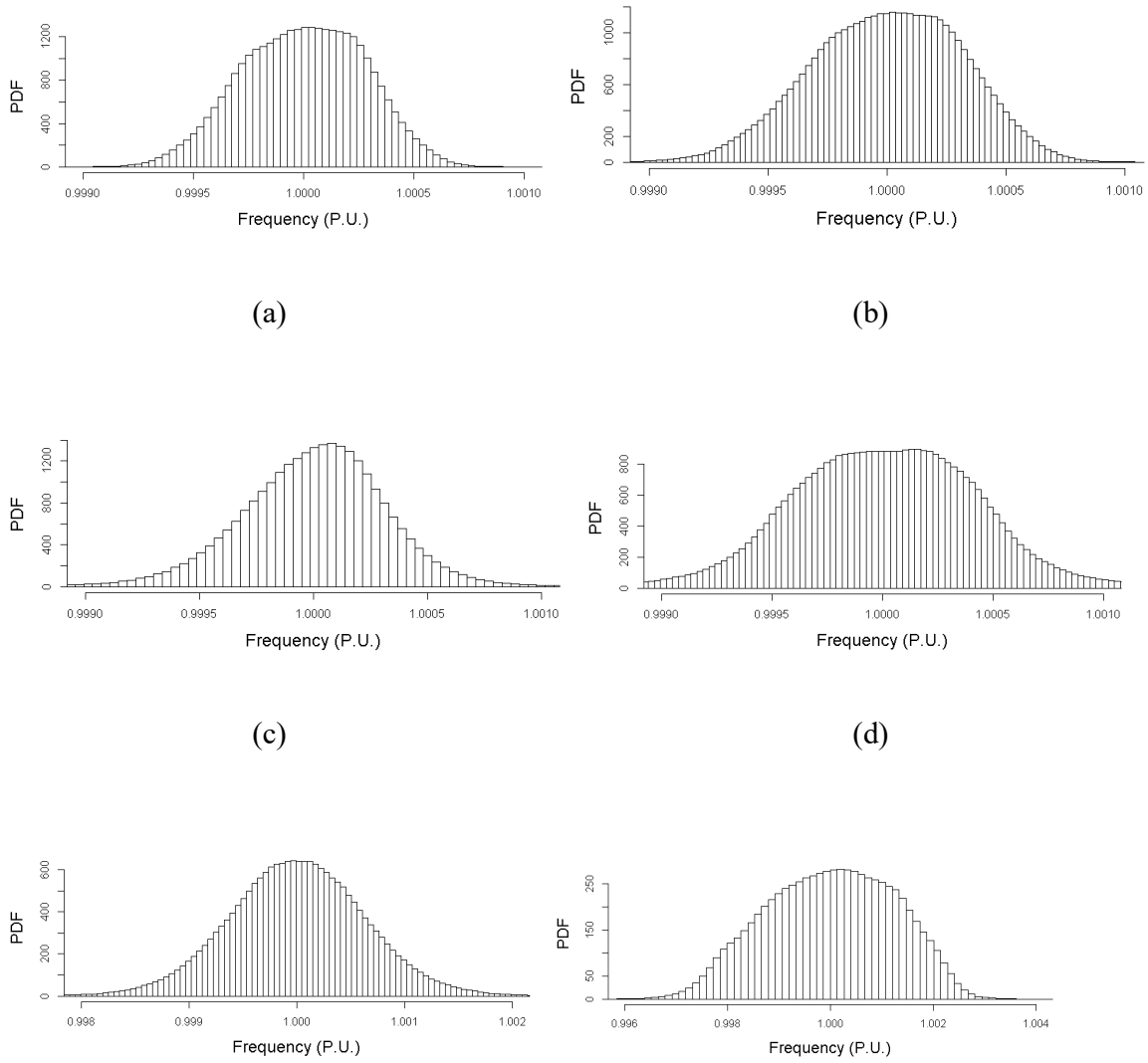

Figure 2.7. Probability density function of frequency in different power grids. (a) EI, U.S. (b) WECC, U.S. (c) Hawaii, U.S. (d) Germany. (e) Japan. (f) Australia. (g) Egypt. (h) ERCOT, U.S. (i) Saudi Arabia. (j) Northern Ireland. (k) Ireland. (l) England. (m) Bahamas.

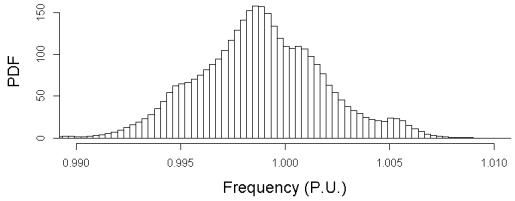

(g)

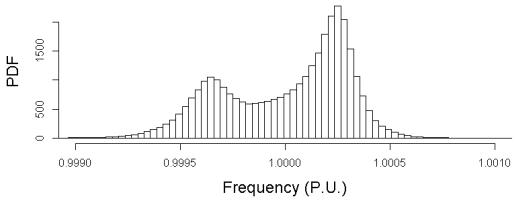

(h)

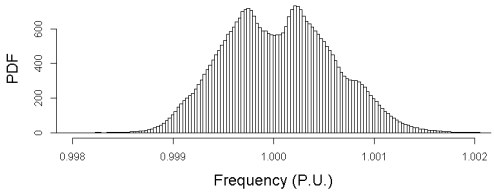

(i)

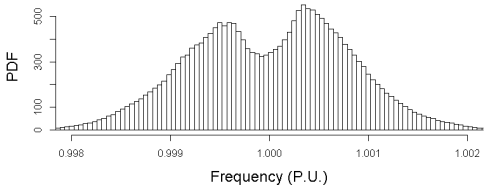

(j)

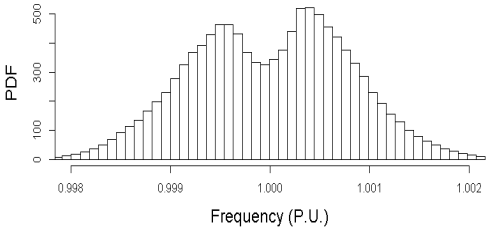

(k)

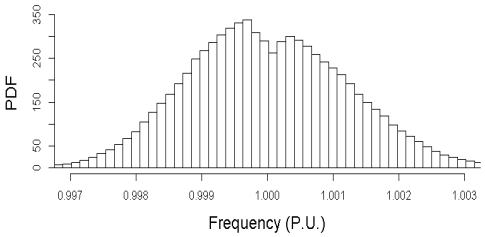

(l)

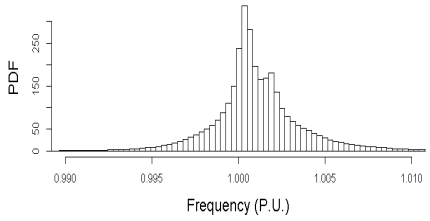

(k)

Figure 2.7 continued

WECC, Hawaii, Germany, Japan, Australia, and Egypt; 2) multi-peak distribution, such as the probability density function of the frequency in ERCOT, Saudi Arabia, Northern Ireland, Ireland, England, and Bahamas.

As shown in Figs. 2.7(a)-2.7(g), for the single-peak distribution of the frequency, the normal distribution is considered an appropriate choice to describe it. The mean and standard deviation values of frequency are calculated and shown in Fig. 2.4 and Fig. 2.5. Based on the calculated mean and standard deviation values, the corresponding probability density functions of the frequency which almost follow normal distribution can be obtained, which is drawn as the red lines in Fig. 2.8. Meanwhile, the real probability density functions of the frequency statistically calculated by the observation data are also shown as the bars in Fig. 2.8. Obviously, the normal distribution provides a suitable profile for the single-peak distribution of the frequency.

2.5 Conclusions

This paper utilizes the frequency measurement data provided by FNET/GridEye, to observe and statistically analyze the power frequency status of various power grids over the world, including the grids located in both mainland and islands. The comparison results show that frequencies of most power grids in mainland operate in a relatively smaller range than those in the islands. From the perspective of regions, the power grids in America has the smallest frequency standard deviation. The standard deviation of Asian and European power grids frequency is at an average level in this study. The frequencies of power grids in Oceania and Africa operate at a high deviation status. Additionally, the distributions of frequency show two different categories in the worldwide power grids, i.e., the single-peak distribution and multi-peak distribution. Furthermore, a meaningful insight that the single-peak distributions of the frequency almost follow the normal distribution is found. Since the lack of the report about the

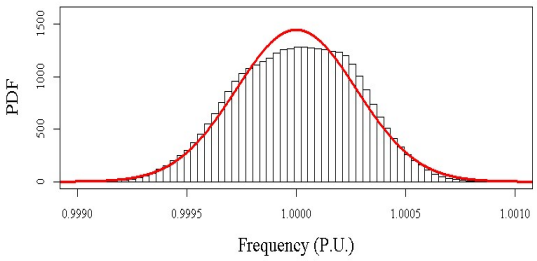

(a)

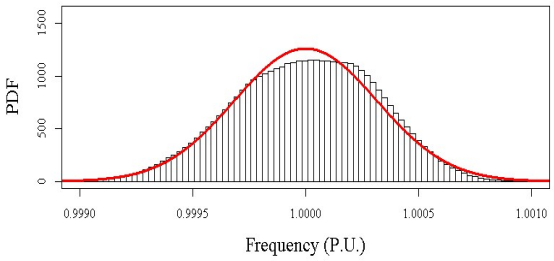

(b)

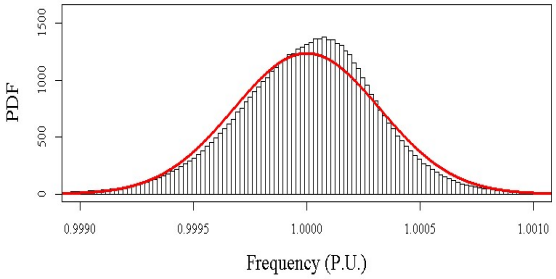

(c)

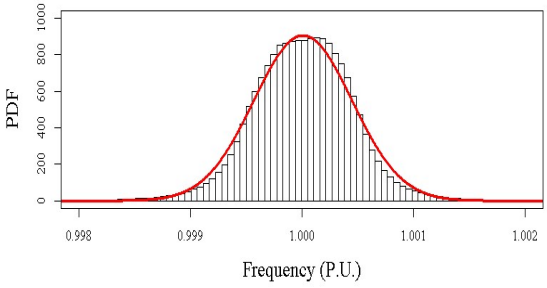

(d)

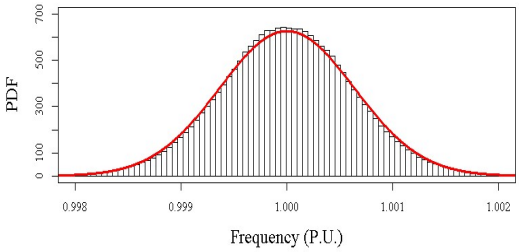

(e)

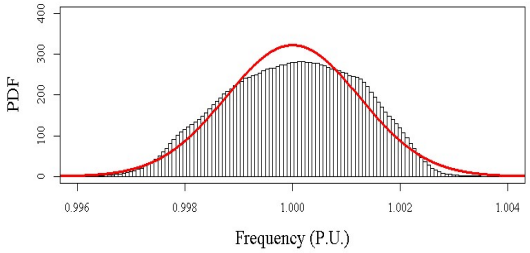

(f)

Figure 2.8. Comparison of probability density function obtained by statistics and the corresponding normal distribution. (a) EI, U.S. (b) WECC, U.S. (c) Hawaii, U.S. (d) Germany. (e) Japan. (f) Australia. (g) Egypt.

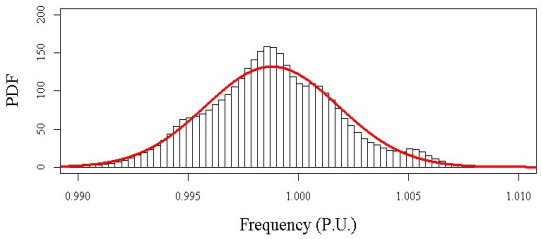

(g)

Figure 2.8 continued

frequency in the worldwide power grids, the analysis in this paper may provide some references for further research or making regulation criteria on the frequency.

Acknowledgment

This chapter is, in part, a reprint of the material in the paper: Xianda Deng, Hongyu Li, Wenpeng Yu, Wang Weikang, Yilu Liu, " Frequency Observations and Statistic Analysis of Worldwide Main Power Grids Using FNET/GridEye, " 2019 IEEE Power & Energy Society General Meeting, Atlanta, GA, 2019.

Chapter 3 Power System Event Detection and Triangulation using High-Density PMU Measurements

3.1 Introduction

The modern power grid is the most complicated artificial system, which has been evolving in recent decades with various technologies [64]-[66]. Meanwhile, renewable energy sources have been promoting and integrated into power grids in recent years [67]. Power grid structures and dynamic behaviors are becoming more complex, due to the flexibility of the new technologies and the fluctuating nature of renewable energy sources. With real-time, global positioning system (GPS) time-synchronized measurements at high data rates, Wide-area monitoring systems (WAMS) reveals unprecedented insights into power grid dynamics and will be the next-generation operational-management systems [68]-[69].

However, a huge amount of PMU data comes with a high resolution brought new challenges for real-time applications:

(1). How to detect abnormal events in a power grid?

(2). Where is the location of the abnormal events in the power grid?

To address these questions, numerous methods have been proposed for power system event detection and location identification based on PMU data. In 2001, Frequency Monitoring Network (FNET) system, a pilot WAMS system, was developed for power system event detection [61]. Decision tree technique and event detection using the rate of change of frequency (ROCOF) was proposed based on real-time measurements from the FNET system [62], [70]. Meanwhile, event detection based on generation-load mismatches and triangulation location identification technique were proposed and implemented [23], [72]. Recently, [24] proposed a

framework based on a sparse linear unmixing technique to detect multiple cascading events in power system for FNET system. Besides, algorithms used in other areas of power systems were also leveraged for event detection and location identification. Wavelet analysis was performed to extract the feature of FDRs data and support vector machine (SVM) was introduced to classify power system events in [13]. In [14], wavelet transform was employed on voltage and frequency measurements from PMU data to identify generation trip and load shedding events. Short time Fourier Transform and statistical techniques were applied to phase angle for online event detection in [15]. In [16], disturbance component can be solved with positive current phasor based on superposition theorem. The event types and location were identified by matching the calculated disturbance component with patterns extracted from historical fault events. Attempts to use principal component analysis (PCA) for power system event detection were conducted in [17]. Later, PCA was employed for real-time event detection at the distribution level [18]. A real-time event detection based on moving windows PCA was developed and demonstrated in the United Kingdom and Irish systems [19]. An investigation of using data mining technique to detect the event and identify event location was introduced in [20]. One of the common study and research scenarios in the aforementioned papers is that the algorithms are tested based on PMUs with low density deployment for demonstration purposes. The accuracy and robustness of event detection applications are seldom tested and reported when it is applied in a power grid with industrial scale PMUs for operation purposes.

Recently, UTK power IT lab cooperated with Global energy interconnection research institute North America (GEIRINA) to develop a real-time event detection and location identification application based on PMUs measurements from the Jiangsu power grid in China. It provides a good opportunity to further explore the capability of the event detection and triangulation in a

power grid with high-density PMU measurements. Meanwhile, low data quality of PMU measurements brings new challenges to this application. In fact, bad data is introduced into PMU measurements due to measurement noise and instrumentation channel errors [25]. The impacts of bad data in simulated PMU measurements have been discussed in other research areas of power system and some solutions were also proposed in [26]-[28]. However, the impacts of low data quality in actual high-density PMU measurement on event detection and location identification have not been reported yet.

In this paper, we use real measurements PMU data from the Jiangsu power grid to evaluate the impacts of low data quality issues on the performance of event triangulation. The event detection was implemented based on the pair-wise comparison from multiple location PMUs and triangulation technique was employed for event location identification. The main contributions of this chapter are summarized as follows: (1) Four types of practical low data quality issues from onsite PMUs are presented. (2) The impacts of bad data on power system disturbance triangulation are explored using simulation and real-time measurement cases from Jiangsu power grid.

3.2 Overview of disturbance triangulation in Jiangsu power grid

A. Overview of high-density distributed PMU deployment in Jiangsu power grid

Jiangsu power grid is located in the east of China and connects with multiple adjacent power grids. There are 114 and 238 PMUs installed at the northern and southern areas of Jiangsu power grid, respectively. As shown in Fig. 3.1, the density of distributed PMU is significantly high. PMUs are mainly installed at terminals of 500kV transmission lines and parts of 220 kV transmission lines with the reporting rate of 25 Hz. To utilize the PMU data and achieve wide-area monitoring purposes, a PMU based situational awareness data analytics platform is

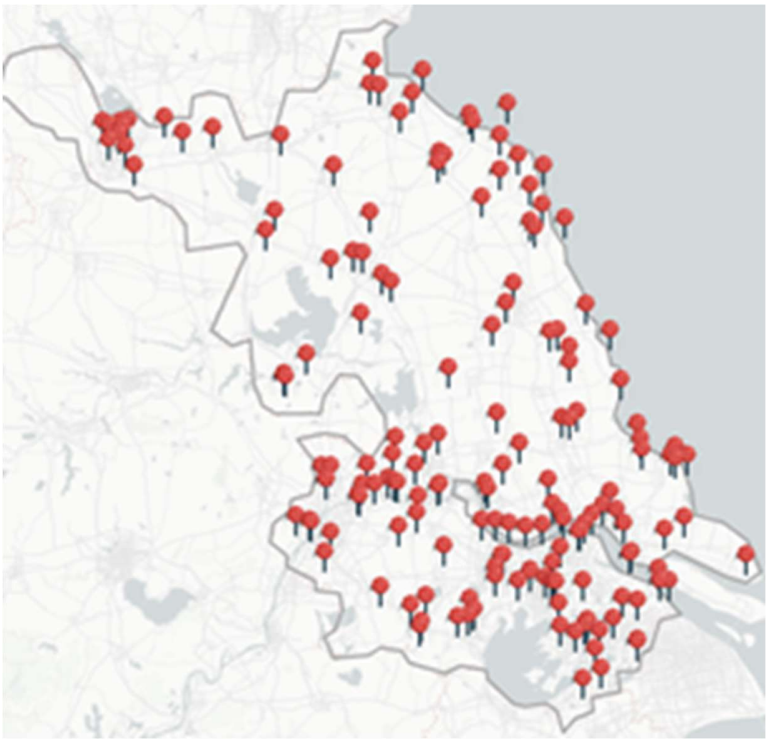

Figure 3.1. Map of PMU deployment in Jiangsu power grid [73]

developed by GEIRINA. Once the PMU data are transmitted to the control center, the data is streamed into multiple power system applications. Event detection and location identification application are composed of three components: event detection, event location identification, and event visualization. The event detection only focuses on detecting if the system is experiencing any generation trip and load shedding events, while triangulation was designed to identify the event location in the power grid.

To deploy the event detection and triangulation application on GEIRINA WAMS platform, an interface was implemented to achieve data exchanges. The basic flowchart of the event detection and triangulation application is shown in Fig. 3.2. The measurements from GEIRINA are aligned based on the timestamp and streamed into the event detection application frame by frame. A certain length of frames is stored in the buffer temporarily. Once a disturbance is confirmed, the data in the buffer will be extracted and delivered to triangulation and visualization applications for location identification and notification.

B. Mechanism of disturbance triangulation

As frequency perturbations travel throughout grid as electromechanical waves dispersing at finite (measurable) speeds, the PMUs located throughout the grid detect said waves with unique time delays proportional to the electrical distance between each respective unit and the disturbance location. Thus disturbance triangulation mainly involves two steps: (1) the determination of the wave-front detected by each unit and its corresponding arrival time and (2) estimating the disturbance location. Once the PMUs close to the disturbance are selected via wave-front detection, the disturbance location can be triangulated by using least square optimization to minimize the estimated distance error as

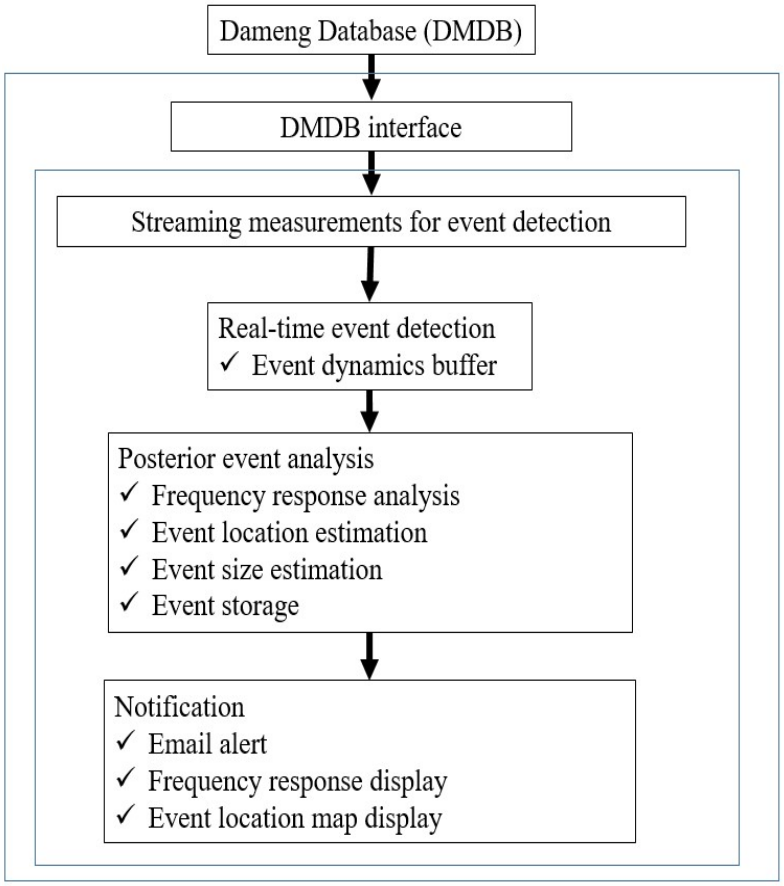

Figure 3.2. Scheme of event detection and triangulation for GEIRINA

$$\min\sum_{i=1}^{n}[(\alpha_i - \alpha_d)^2 + (\beta_i - \beta_d)^2 - v^2(t_i - t_d)^2]^2 \quad (3.1)$$

$$\text{s.t.} \quad \alpha_{min} < \alpha_d < \alpha_{max}$$

$$\beta_{min} < \beta_d < \beta_{max}$$

$$0 < t_d < t_i, \forall i \in \{1,2,\dots,n\}$$

where n denotes the number of PMUs used to estimate disturbance location, (α_i, β_i) and (α_d, β_d)represent the coordinates of Lambert projection from i-th PMU and real disturbance location, v denotes the propagation speed of the electromechanical wave, t_d denotes the start time of the disturbance and t_i denotes the wave-front arrival time of i-th PMU.

C. PMU measurement preprocessing filter

Data quality of raw PMU measurements from operating power grids may degrade due to various factors such as temporal communications failure, synchronization inaccuracy and etc. To eliminate the noise and extract the signal of interest events from raw PMU measurements, a PMU data preprocessing filter was designed and implemented [22]. The block diagram of the PMU data preprocessing filter is shown in Fig. 3.3. PMU raw measurements are fed into a threshold filter to remove random noises. Then a low-pass filter combining with a moving median filter is used to remove high-frequency noise. Another low-pass moving average filter is employed to extract the trend of filtered frequency measurements. The data after preprocessing filter is delivered to the event detection and triangulation application for further analysis.

3.3 Practical data quality issue of high-density deployed PMU

In practical industrial applications, measurements from onsite PMU are likely to contain different types of low data quality issues caused by communication or PMU hardware

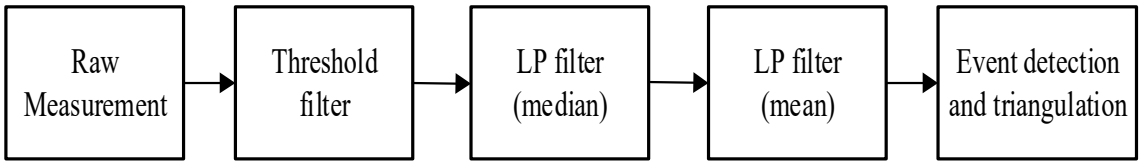

Figure 3.3. PMU measurement preprocessing block diagram

malfunction. This section presents four major data issues discovered in PMUs deployed in Jiangsu power grid.

A. Constant measurements

Constant PMU measurements are mainly caused by PMU hardware issues. The value of measurements periodically repeats with different intervals under both ambient or event conditions. A typical constant measurement is presented in Fig. 3.4. When the most PMU frequency measurements drop during a generation trip event, some of the PMU measurements keep the constant periodical patterns before and after the event thus missing the information of the power system event.

B. Random spikes in measurements

Random spike in measurements is another typical data quality issue caused by PMU hardware issues. The frequency and magnitude of the spikes vary case by case. Thus it is difficult to extract the feather of the spike and apply a uniform filter to remove them. It can be observed in Fig. 3.5 that some measurements have random spikes in the aspect of amplitude and time interval. Additionally, some spikes keep swinging around system frequency as shown in Fig. 3.5. The tendency of the swing indicates that the mean value of the measurement keeps changing over time.

C. Missing data in measurements

Missing data happens in PMU measurements due to several uncontrollable factors (e.g. GPS signal lost, network failure, power failure, etc. [74]). Detecting the missing data is straightforward since each PMU measurement is assigned a unique time index thus a discontinuous timestamp implies the existence of missing data. The entire raw data are broken down into several non-overlapping frames. The miss data results in discontinuity and outlines of

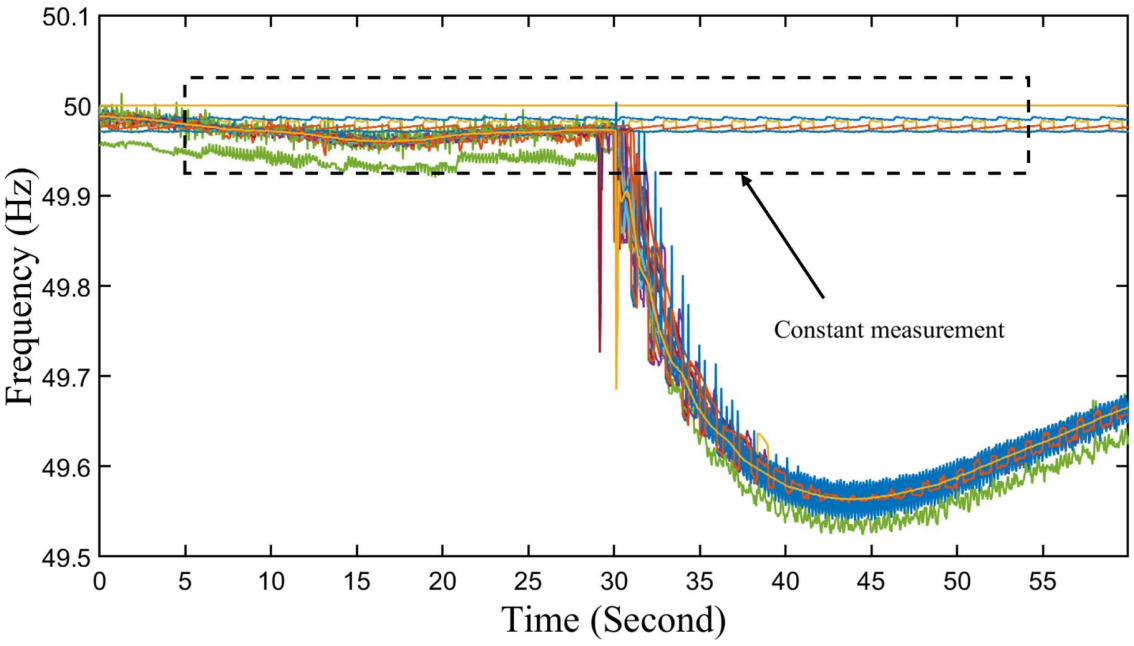

Figure 3.4. Illustration of constant measurement during a generation trip

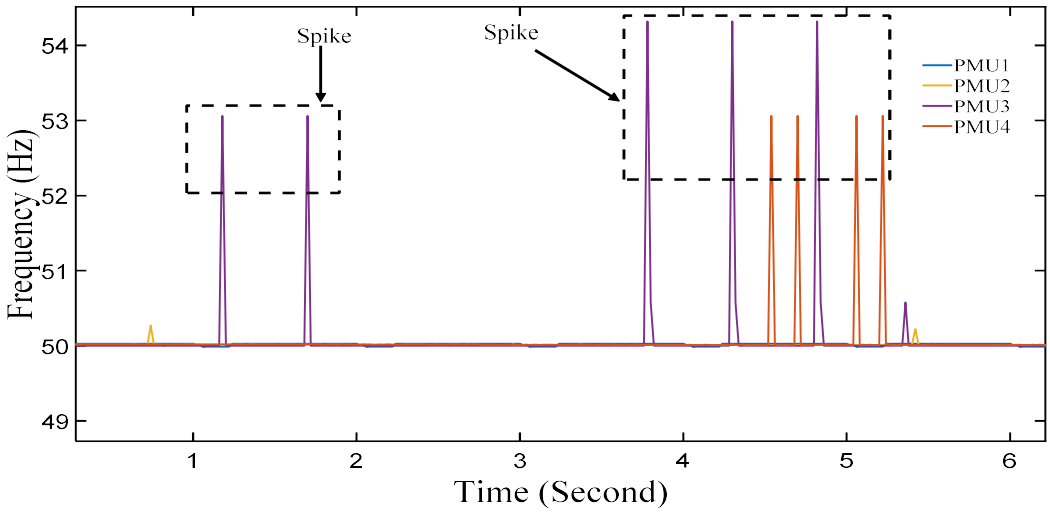

Figure 3.5 Illustration of random spike issue

PMU measurements. As shown in Fig. 3.6, missing data at the GEIRINA PMUs platform can occur frequently and the result suddenly jumps to “0” Hz in frequency measurement from PMU2.High-frequency noise in measurement

The measurement with high-frequency noise can be caused by an inaccurate sampling interval control related to PMU calibration and wrong PMU hardware configuration [75]. It makes the measurements with high-frequency noise and keeps swinging around the actual system frequency. Based on the measurement data from the Jiangsu power grid, the amplitude of the noise varies in a relatively wide range, from 0.01 to 0.2 Hz. As shown in Fig. 3.7, high-frequency noise for each PMU has slight differences in amplitude. Thus, the randomness and variety of the high-frequency noise make it difficult to be removed with a uniform threshold filter.

3.4 Simulation and real-word cases study

To investigate the performance and robustness of the event detection and triangulation location application, a series of tests, including load shedding and generation trip events simulation and one real-world generation trip event, are designed and conducted. To further evaluate the robustness of the application under normal operation status with low data quality PMU measurements, the application is tested with ambient PMU measurements collected from Jiangsu power grid.

(1). Simulation cases

To verify the effectiveness of the event detection and triangulation application in a power grid with high density PMU, 8 generation trip and 2 load shedding events in Jiangsu power grid are simulated. The Jiangsu power grid covers 39,614 mi^2 and consists of two major regions: Su Nan and Su Bei. The power grids in two regions are connected via four 500 kV transmission lines.

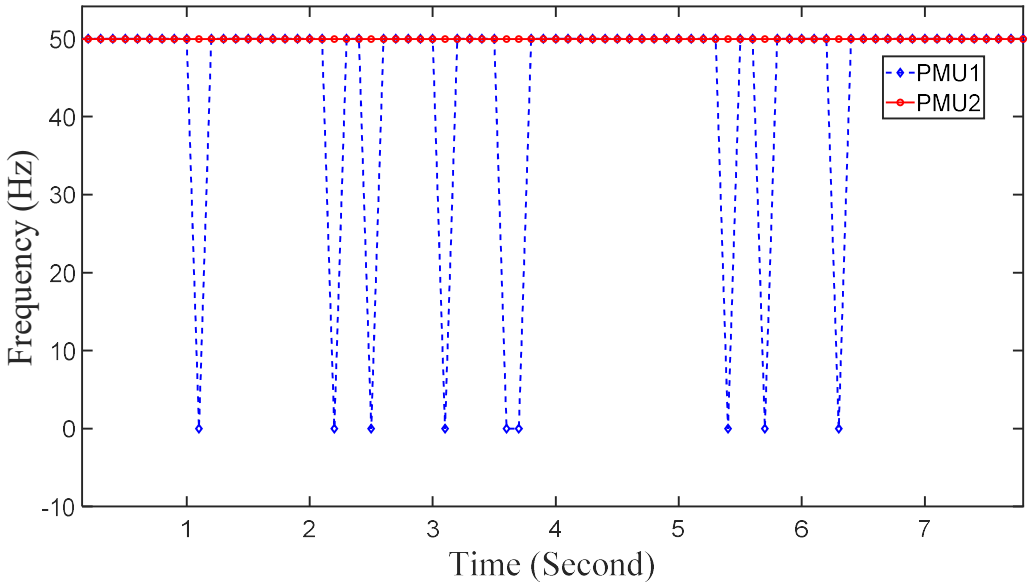

Figure 3.6. Illustration of data missing issue

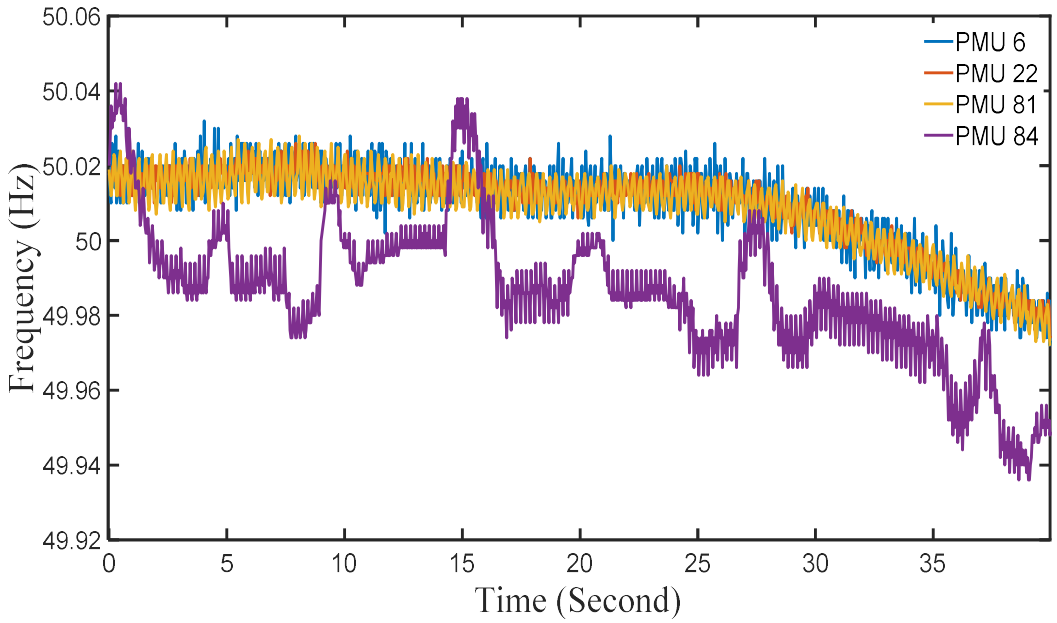

Figure 3.7. Illustration of high-frequency noise issue

Jiangsu power grid is modeled as a system with 2488 buses and 4811 branches within PSD-BPA. PSD-BPA is a widely-used power system analysis software package in Chinese electric power industry, which was introduced around the 1980s and further developed by China Electric Power Research Institute (CEPRI) [76]. To comprehensively exam the application, the events are selected at different locations in the two regions and the amount of generation and load impacted by the events are from 200 MW to 1167 MW. The details of the simulation cases and actual event locations are summarized in Table 3.1. Each case contains 1-minute PMU measurements, which are collected with 40 Hz sampling ratio. All the events occur at 5 seconds of the simulation cases.

The event detection and triangulation application successfully detected all the simulation events at the correct times and pinpoint the event location accurately. The reported locations of the applications are marked in a red circle from Fig. 3.8 to Fig. 3.16. Based on the operation and event detection experiences of UTK FNET system, the performance of the event detection and triangulation application in Jiangsu power grid is remarkable in the simulation cases.

(2). Real-world generation trip case

To further evaluate the capability of the event detection and triangulation application, a real-world generation trip case, which occurred in Jiangsu power grid at 2015, is tested and analyzed. The generation case includes 7 minutes of measurements collected from Jiangsu power grid. The measurements start at 21:57:00 and the event happens at 21: 57:59. The system frequencies measured by PMUs during the event are plotted in Fig. 3.17.

As shown in Fig. 3.17, the PMU measurements contain multiple low data quality PMUs, some of the PMUs frequencies stay the same after the event happens. The event was successfully detected and located by the application. The reported information about the event is summarized

Table 3.1. Description of simulation cases

Case Name	Event type	Size (MW)	Truth	
			Latitude	Longitude
Bixi	Generation trip	1167	31.7574	120.9782
Nantong power plant	Generation trip	412	32.0527	120.8062
Yang er Chang	Generation trip	728	32.2953	119.4118
Xinhai Chang	Generation trip	1145	34.5958	119.1519
Huzhong Gang	Load shedding	218	Chongming island	
Yang er Chang	Load shedding	1000	32.2953	119.4118
Jianbi Chang	Generation trip	1000	32.1726	119.5812
Gaogang Chang	Generation trip	1000	32.2389	119.9298
Chenjiang Gang	Generation trip	660	34.0329	119.8586

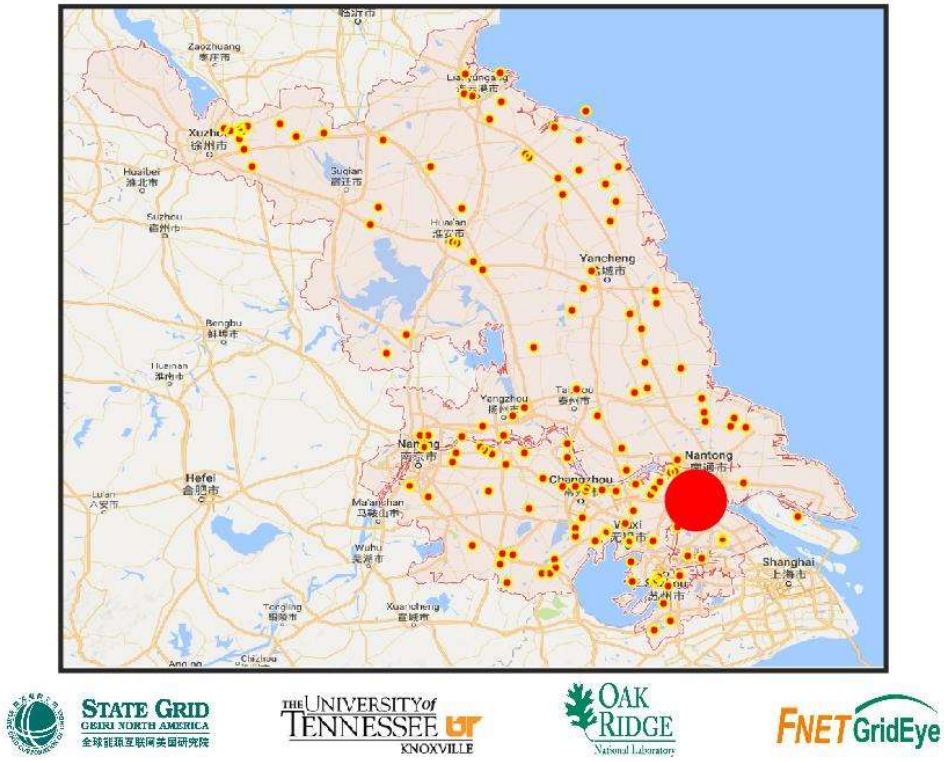

Figure 3.8. Event detection and triangulation results of Bixi case

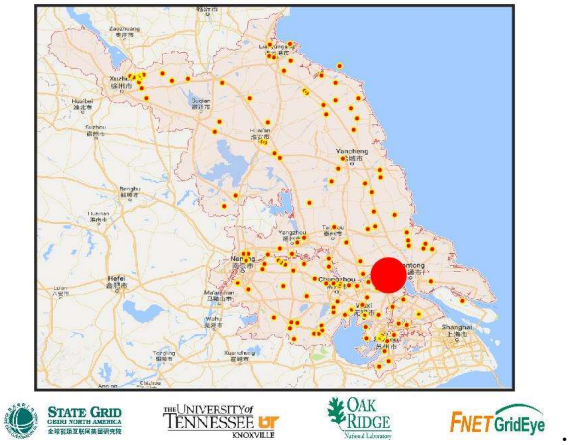

Figure 3.9. Event detection and triangulation results of Nantong power plant case

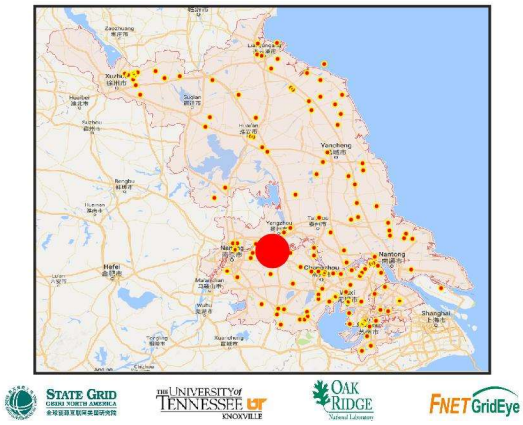

Figure 3.10. Event detection and triangulation results of Yang er Chang Generation trip case

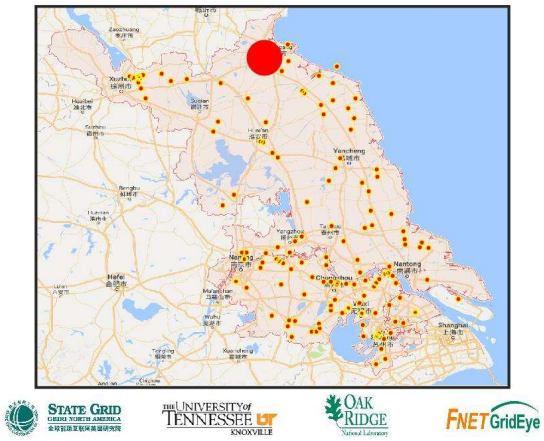

Figure 3.11. Event detection and triangulation results of Xinhai Chang case

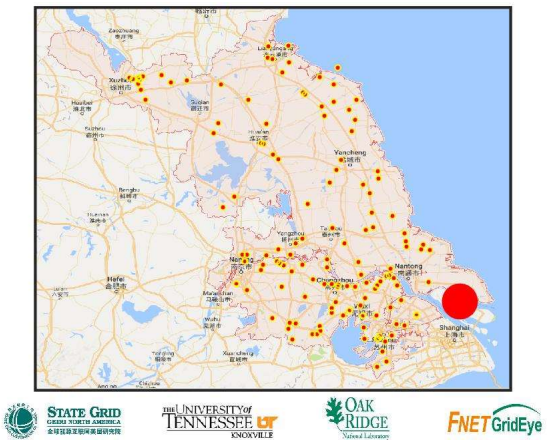

Figure 3.12. Event detection and triangulation results of Huzhong Gang case

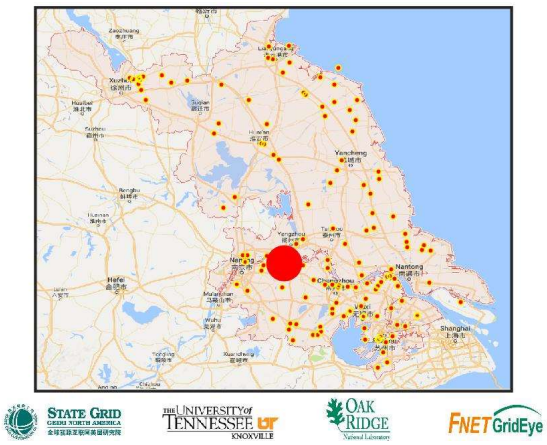

Figure 3.13. Event detection and triangulation results of Yang er Chang Load shedding case

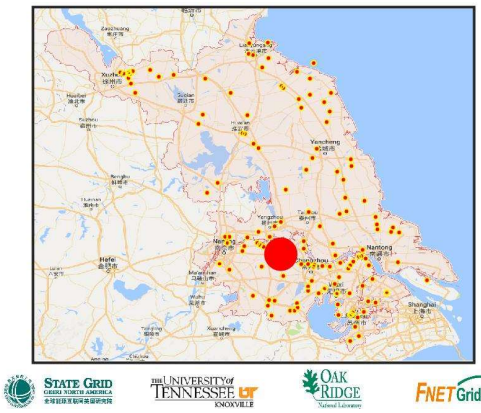

Figure 3.14. Event detection and triangulation results of Jianbi Chang case

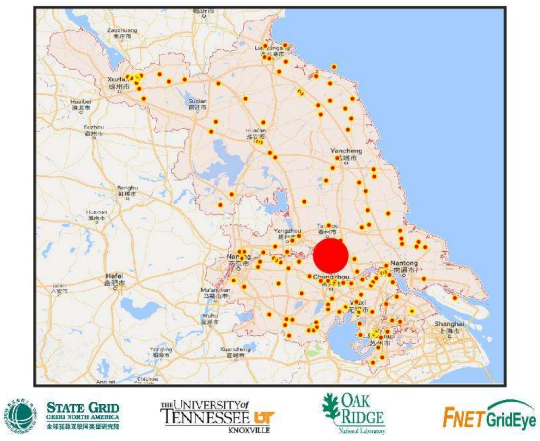

Figure 3.15. Event detection and triangulation results of Gaogang Chang case

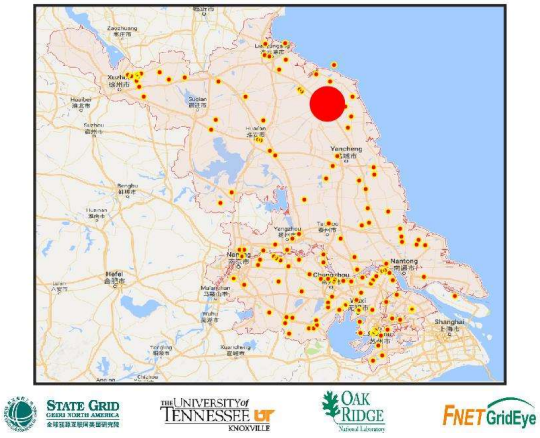

Figure 3.16. Event detection and triangulation results of Chenjiang Gang case

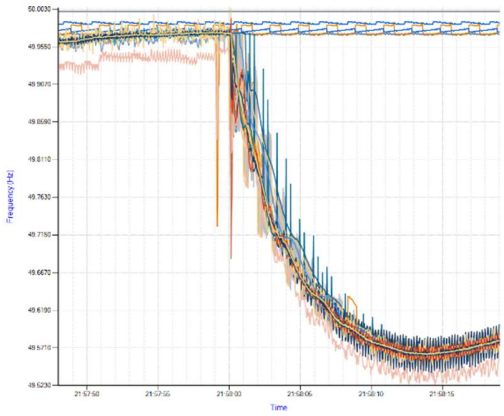

Figure 3.17. PMU frequency measurements during a generation trip in Jiangsu power grid

in Table 3.2. The estimated location is approximately 12 miles away from the actual location. Based on the event detection experience of UTK FNET system, this error is acceptable for the Jiangsu power grid. The estimated location and actual location are plotted in Fig. 3.18.

(3). Ambient cases

As discussed in section 3.3 and demonstrated in a real-world generation trip case above, the low date quality issues of PMU measurements in Jiangsu power grid are common and severe. It has been concerned that the low data quality issues of PMU measurements may cause a false alarm of the event detection application under normal operation status. To validate the robustness of the event detection application, 75 ambient cases with one-minute PMU measurements from Jiangsu power grids are steamed into the application for false alarm tests. In Fig, 3.19, a typical ambient case is plotted. As shown in Fig. 3.19, the multiple PMU measurements jump to 0 and come back and some measurements stay at extremely higher than the system frequency. To further analyzed the cases, frequency higher than 52 Hz and lower than 48 Hz are removed for a better visualization purpose. Many PMUs measurements still have data quality issues, after removing extreme measurements and two typical ambient cases are plotted in Fig. 3.20 and Fig. 3.21. The event detection application remains stable and no false alarm was triggered with all the ambient cases.

To further investigate the stability of event detection application under communications issue, a one-hour ambient case is provided by GEIRINA and plotted in Fig. 3.22. The one-hour ambient case emulates a scenario that all PMUs measurements are lost simultaneously and recovered after a while, due to communication failures of the PMU data platform. The test result indicates that the event detection application does not have any erroneous alarming under such circumstances.

Table 3.2. Reported event information of a generation trip event in Jiangsu power grids

Detected event time	21: 57:59
Frequency propagation speed	866.64 mile/second
Relative event time	-0.011015 second
Estimated latitude	31.5071
Estimated longitude	119.8953
Triangulation calculation error	1.9606

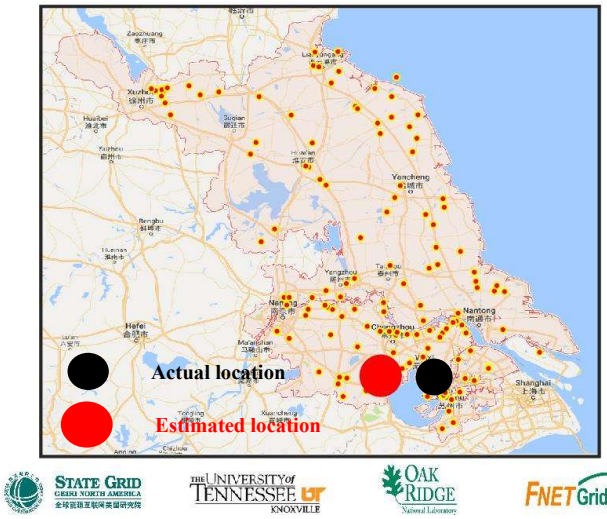

Figure 3.18. Generation trip event location and estimated location in Jiangsu power grid

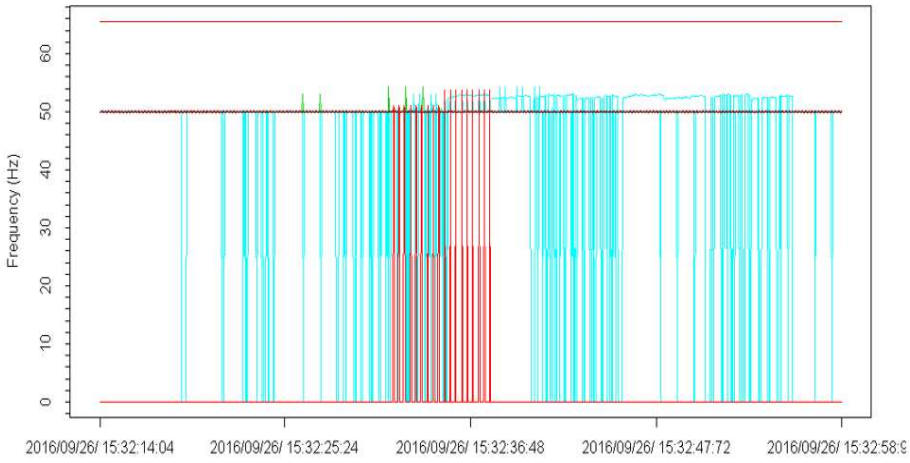

Figure 3.19. A typical ambience case in Jiang power grid

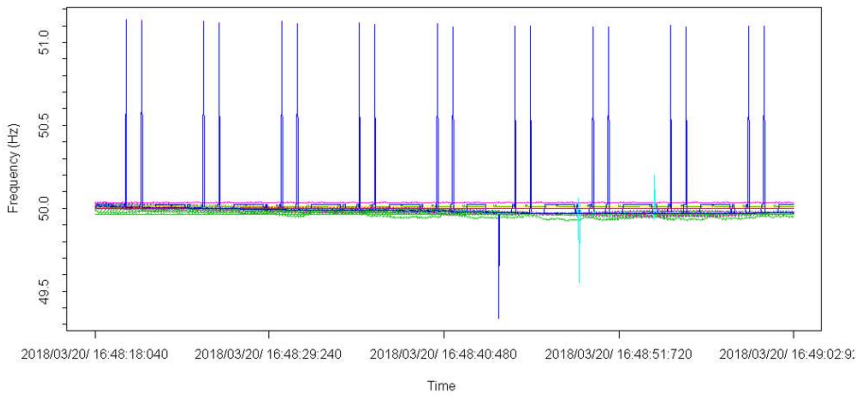

Figure 3.20. Filtered ambience case (a) from Jiang power grid

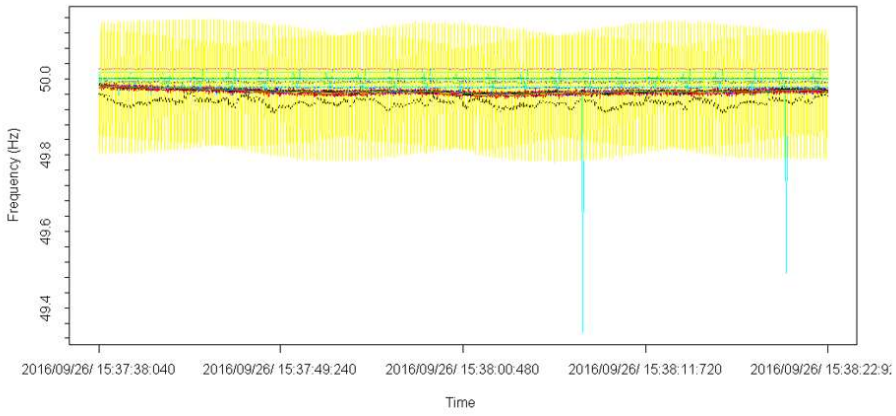

Figure 3.21. Filtered ambience case (b) from Jiang power grid

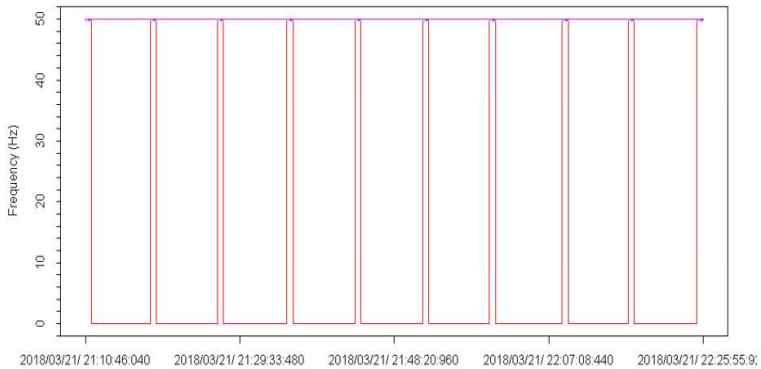

Figure 3.22. A one-hour ambience case from GEIRINA data platform

3.5 Impact of Data Quality on Event triangulation

The purpose of this section is to investigate the impacts of low data quality on the accuracy of event triangulation when using high-density PMU measurements. To this end, an actual generation trip in the Jiangsu power grid is selected for this study. Each bad data issue mentioned in Section 3.3 is considered. It is assumed that the measurements of a PMU that is the first one responding to the actual event disturbance, referred as PMU1 deployed at latitude 31.60 and longitude 119.99), encounters with bad data issues. The scenarios of each testing case are given below:

1) Base case: original raw data case without any bad data issue
2) Case 1: PMU1 with constant measurement issue
3) Case 2: PMU1 with random spike and missing data issue
4) Case 3: PMU1 with high-frequency noise issue

Based on the triangulation method, the estimated locations for each case are illustrated in Fig. 3.23 to Fig. 3.26. The summary result is listed in Table 3.3. In the based case, the estimated location is close to the actual location within 12 miles estimation error, which demonstrates the TDOA can estimate location accurately in normal conditions. It can be seen from Fig. 3.24 that the constant measurement issue will lead to a large estimation error. The estimated location is more than 100 miles far away from the actual location. The impact of other types of data issues including random spike, missing data, and high-frequency spike is negligible according to the results Fig. 3.25 to Fig. 3.26, which indicates that the preprocessing filter has successfully eliminated the impact of these bad data issues before the measurements been fed into TODA algorithm.

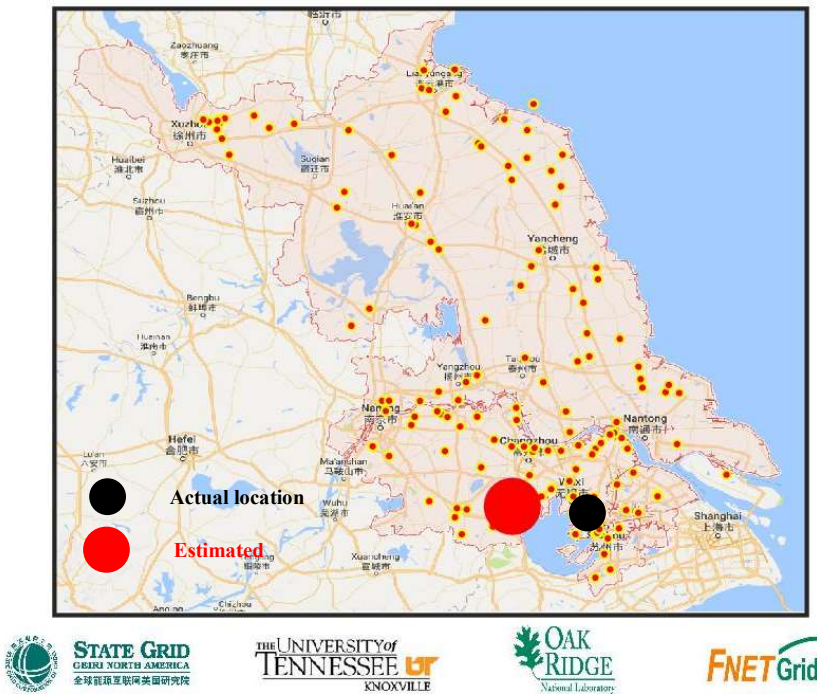

Figure 3.23. Base case without any base data issue

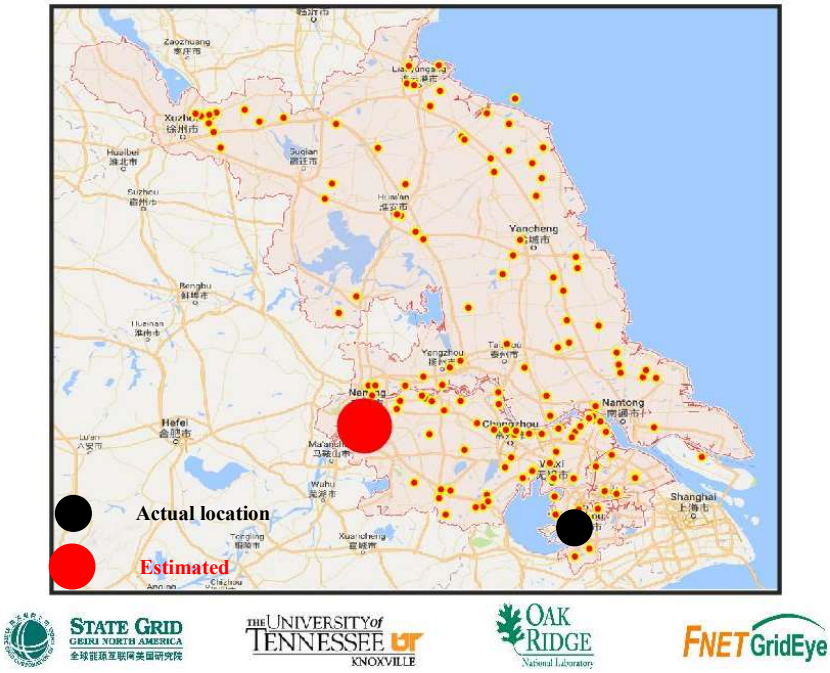

Figure 3.24. Case 1: PMU1 with constant measurement

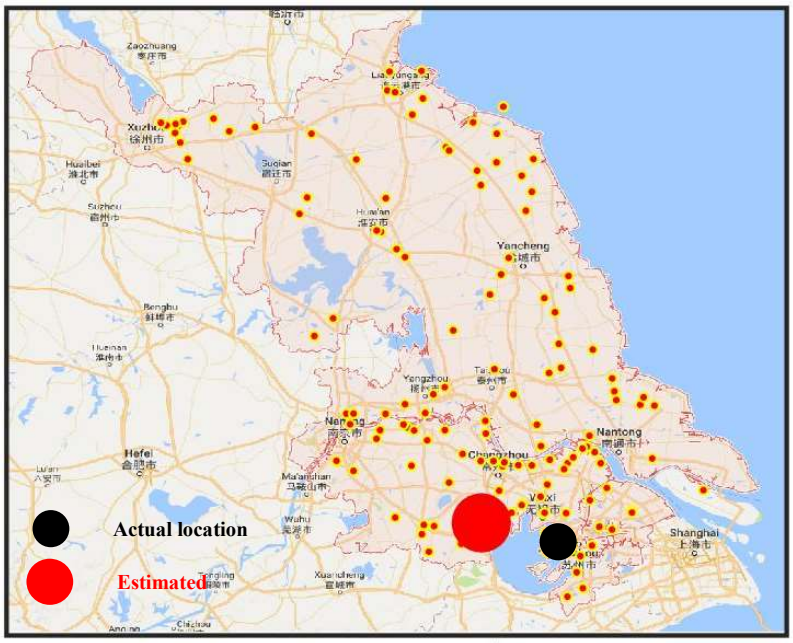

Figure 3.25. Case 2: PMU1 with random spikes

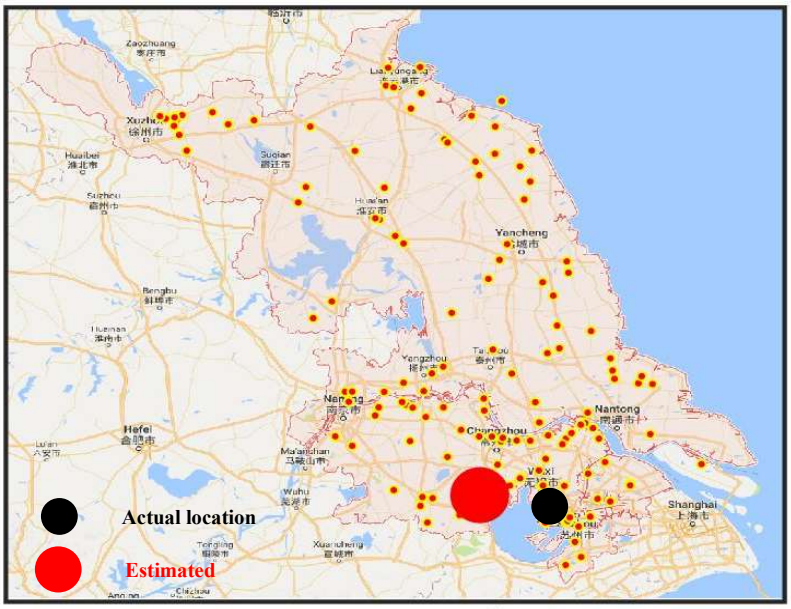

Figure 3.26. Case 3: PMU1 with high-frequency spikes

Table 3.3. Summary of impact of low data quality on event triangulation

Cases	Latitude	Longitude	Error to the actual location (miles)	Impacts
Base case	31.50	119.89	12	NA
Case 1	31.98	118.69	100	High
Case 2	31.50	119.89	12	negligible
Case 3	31.50	119.89	12	negligible

3.6 Conclusion

Onsite PMU measurements always have low data quality issues due to various uncontrollable and unpredictable factors, which will degrade the performance of measurement based applications. To investigate this problem from an industry perspective, this paper presents four typical types of low data quality issues in high-density PMU measurements. Since the event triangulation is one of the commonest applications using high-density PMUs, the impacts of the low data quality issues on event triangulation are explored using measurements from the Jiangsu power grid as an example. It is discovered that the constant measurement will cause the inaccuracy of event triangulation significantly while the impacts of other low data quality issues are negligible due to the utilization of the preprocessing filter. This paper provides a practical reference for utilizing PMU data in the application of event triangulation.

Acknowledgment

This chapter is, in part, a reprint of the material in the paper: Xianda Deng, Di Shi, Desong Bian, Wenxuan Yao, Ling Wu, Yilu Liu, “Impact of Low Data Quality on Disturbance Triangulation Application using High-Density PMU Measurements”, in IEEE Access, vol. 7, pp. 105054-105061, 2019.

Chapter 4 Line Outage Detection and Localization using High-Density PMU Measurement

4.1 Introduction

The detection and localization of transmission line outage in power system are of great significance for the system operators to take prompt action to avoid the widespread damage and maintain the reliability of power supply [77]-[78]. Most of the current methods rely on angle data along with network susceptance matrix to calculate power injection change, which is a high computation burden and requires the information of system parameters [78]-[83]. The method using PMU angle data and network susceptance was originally proposed in [78] and pre- and post-outage power flow were calculated to match the measured event. Later, compressive sensing and global optimization techniques are proposed to improve the method in [79] and [80]. A general Bayesian criterion was employed to handle the uncertainty issue of PMU data in [81]. Different new schema and frames are developed to deal with bad PMU measurements in [82] and [83]. However, the system parameter may not be available all the time due to strict security concerns.

With the rapid transformation from the traditional power system into the smart grid, there are various types of novel applications involved in the system [84]-[88]. All these smart grid applications are relying on the high-sampling rate data [89]-[90], such as synchrophasor measurements. Nowadays, the density of synchrophasor is increasing dramatically to observe the dynamic behavior of the system following a contingency, which gives the unpreceded insights to the system [47], [91]-[92] For example, there are 114 and 238 PMUs installed at Jiangsu power grid, respectively. As shown in Fig. 3.1, the density of distributed PMU is significantly high, which covers all 500kV transmission lines and parts of 220 kV transmission lines with the

reporting rate of 25 Hz. To utilize the PMU data and achieve wide area monitoring purposes, a PMU based situational awareness data analytics platform has been developed by Global Energy Interconnection Research Institute North America (GEIRINA) [93]-[95]. The PMU based platform collects synchrophasor measurements with massive channels in real-time from Jiangsu power grids and processes a large amount of data, which can be affected by latency from PMU device or communication network. The platform not only incorporates event detection application developed by GEIRINA, but also provide an interface for event detection applications from third parties. The density synchrophasor measurement brings the opportunity to detect the line outage location and locate the fault location without knowing the system parameters. The line outage detection approach introduced by [22] was employed in the PMU based platform and the reported line outage locations have a significant deviation from actual line outage location. Similar phenomenons were also founded in simulation cases in New England ISO (ISO-NE) and Tennessee Valley Authority (TVA) systems.

To address the issue mentioned above, this paper focuses on the method for line outage detection and localization via high-density synchrophasor measurement. First, the line outage is detected via employing low pass filter and peak detector on synchronized frequency measurements. Once a line outage event is triggered, the location of the fault line will be pinpointed using power flow change. The requirement of computational effort for the whole process is not high thus outage location can be estimated in real time. The proposed method is straightforward and easy to implement. It also can be used for cross-checking line outage events via SCADA.

4.2 Line Outage Detection and Localization

The proposed method for line outage detection and location estimation in the paper includes two steps: (1). Line outage event detection using frequency measurement; (2). Outage line localization using active power measurement.

The frequency measurements from deployed PMUs are used to monitor that if there is ongoing a line outage event in the system. The principle of outage detection can be found in Ref [22], [95]. The frequency measurements are first fed into a moving median filter to remove random spikes and high-frequency noises. After that, a moving mean filer is used to extract the frequency trend as a reference. Then de-trended frequency data is subtracted frequency trend from filtered frequency measurements. Two thresholds are empirically set based on statistical analyses of historical data [22]. The event outage will be triggered using threshold evaluation. The event time can be determined via GPS timestamp on the measurements [74], [96]-[98], which will be utilized further for event location estimation with active power measurements.

When a line outage event happens, the active power flow will be redistributed partially since the power flow on the tripped line has to transfer the rest of the system abruptly, which provides useful information for line outage location estimation. The Power Transfer Distribution Factors (PTDFs) of line l respect to a power flow transaction Δw in a lossless model is defined as [99] - [100]:

$$\varphi_l = \frac{\Delta l}{\Delta w} \tag{4.1}$$

where Δw is MW of power transfer between two locations and Δl is the power transfer via branch l respect to the transaction. Then, for an outage at line m, Line Outage Distribution Factor

(LODF) is defined as the portion of pre-outage real power flow transfer to a line k [99], which can be represented as

$$\varsigma_m = \frac{\Delta P_k}{P_m} = \frac{\varphi_k}{1-\varphi_m} \tag{4.2}$$

where ΔP_k is the power flow transfer changes at line k and P_m is the of pre-outage real power flow at line m. According to the definition in Eq. (4.1) and (4.2), PDTF and LODFs are less than 1.

Meanwhile, buses in pre-and post-outage conditions must follow Gustav Kirchhoff's Current Law (KCL). Defining the power flow change at terminal k_1 is ΔP_{k_1}, the power flow change outage follows:

$$\Delta P_{k_1} = \mathrm{Sum}\big(\Delta P_j\big), \tag{4.3}$$

$$s.t., j \in branch\ connected\ to\ k_1$$

where j is the indexes of the lines.

In an actual power system, the disturbance usually spread out from the source to the rest of the system. As a result, the bus with relatively large power flow changes might be closer to the location of the outage line, that is $\Delta P_{k_1} > \Delta P_{j_1}$ when the distance of k_1 to the outage location is smaller than j_1. Therefore, the bus of the outage line is likely to have the largest power change in the system.

Using the active power change from synchrophasor, the location of an outage can be estimated. Specifically, once a line outage event is detected, noise in active power measurement is filtered by a median filter. With detected event timestamp, the active

power change between pre-outage and the post-outage is calculated with the filtered active power measurements. By ranking the active power change on the monitored transmission lines, the location of the outage line can be determined with maximum value. The process of the line outage detection and localization method is presented in Fig. 4.1.

4.3 Distribution of Power Change in TVA and ISO-NE

This section investigates the characteristic of power flow change distribution caused by line outage via PSS/E simulation. Line outage events are simulated in both ISO-NE and TVA systems, respectively. ISO-NE system consists of 3447 buses and 2479 branches in 71,992 mile^2. The total generation is 18.1GW and the total load is 21.8 GW in the system. There are 16 tie lines, which carry 3.7 GW power flow, connecting to the system. TVA system has 1920 buses and 1720 branches. There are 28.1 GW generation and 31.6 GW load within TVA system. The TVA system is connected with external systems via 70 tie lines and a total of 3.5 GW energy is delivered by the tie lies. The simplified system diagram of ISO-NE and TVA systems are shown in Fig. 4.2 and Fig. 4.3, respectively.

For a comprehensive study, 6 transmission lines in ISO-NE and TVA system are selected and tripped. The voltages levels of the outage line are from 115 kV to 765 kV. The terminal locations (latitude and longitude) of the outage line and pre-outage real power flow on the lines are given in Table 4.1. The locations of the disturbance and distribution of power flow changes caused by the line outage are shown from Fig. 4.4 to Fig. 4.5. It can be seen that the power flow changes at

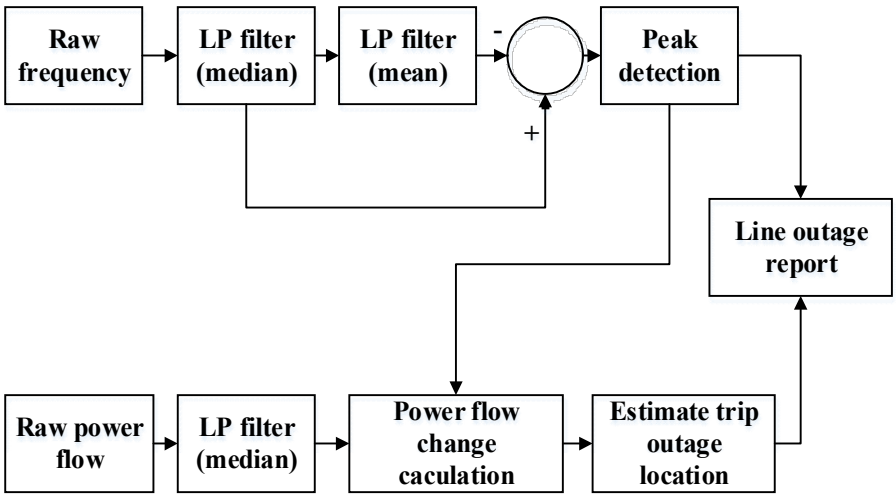

Figure 4.1. Flowchart of line outage detection and localization

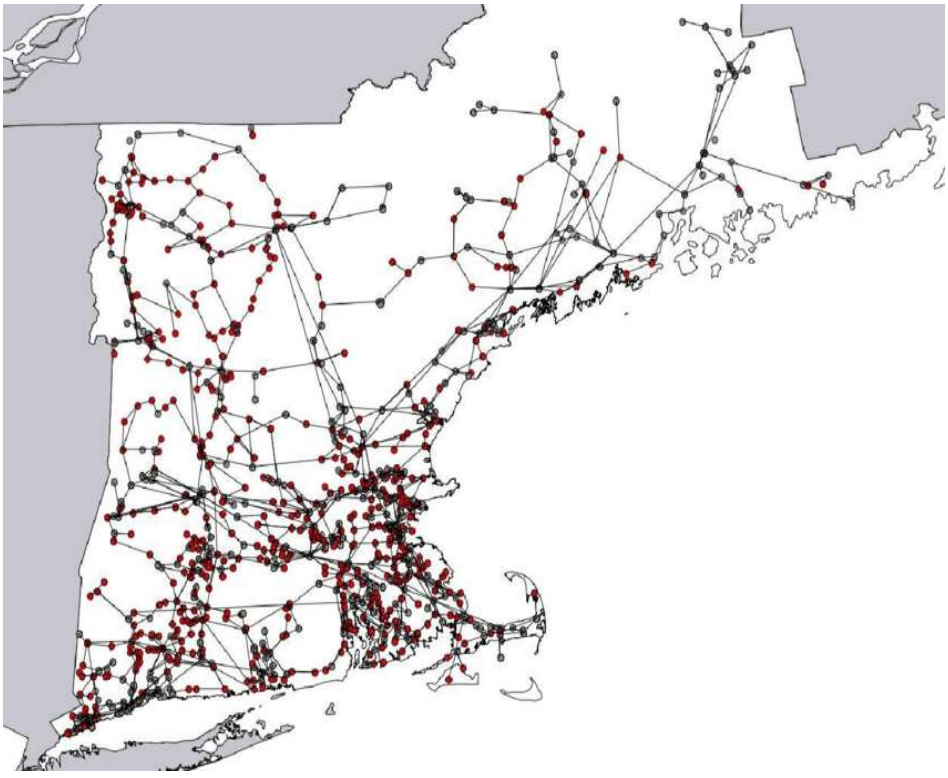

Figure 4.2. ISO-NE model—transmission network map [101]

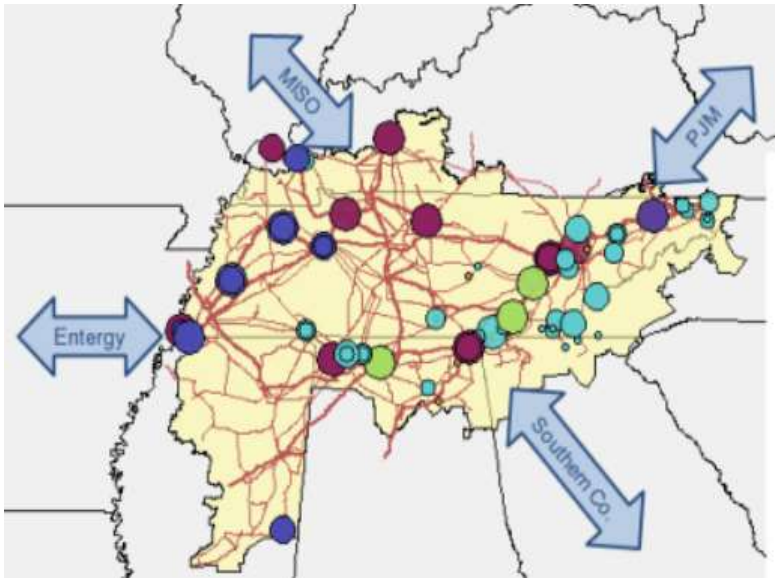

Figure 4.3. Diagram for Tennessee Valley Authority [102]

Table 4.1. Analysis for line outage location estimation

System	Case name	Termial1 (Lat,Lon)	Termial2 (Lat,Lon)	Power flow (MW)	Voltage level(kV)
ISO-NE	Line1	41.51,-72.56	41.29,-72.90	407.36	345
	Line2	42.63,-71.05	42.70,-70.87	100.75	115
	Line3	42.91,-70.86	42.91, -70.86	1101.7	345
TVA	Line4	35.10,-85.02	34.05,-85.08	856.78	500
	Line5	37.78,-86.48	37.26,-86.98	246.72	161
	Line6	35.15, -90.27	35.17, -89.75	1507.1	765

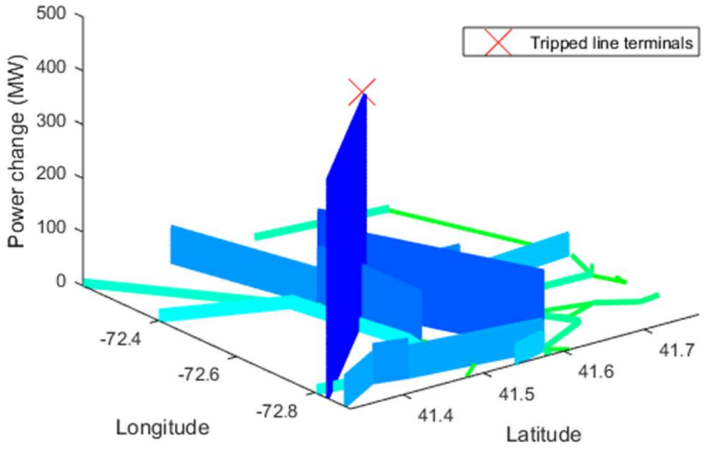

(a)

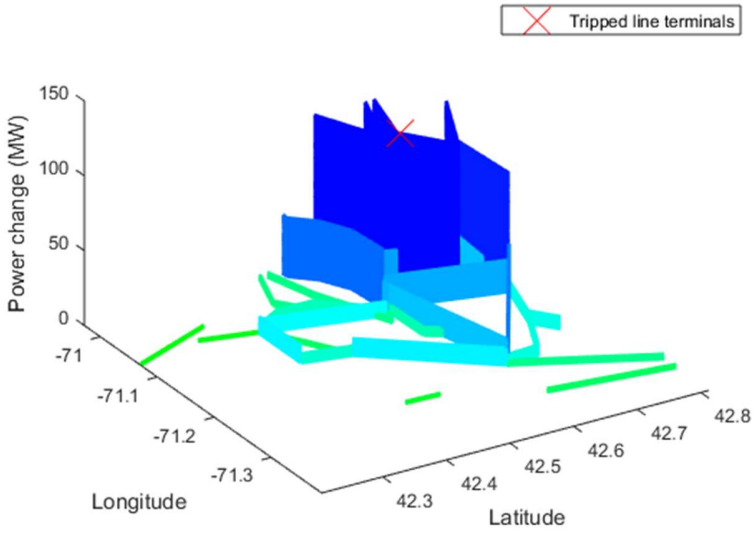

(b)

Figure 4.4. Distribution of power change in ISO-NE system (a) Line1 outage (b) Line2 outage (c) Line3

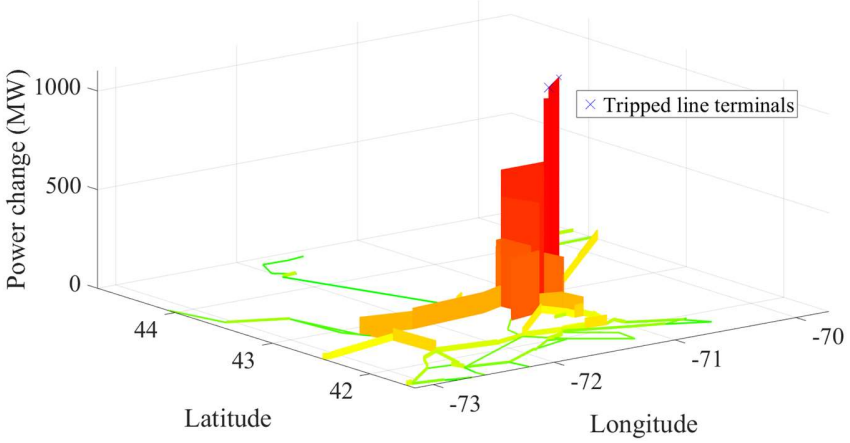

(c)

Figure 4.4 continued

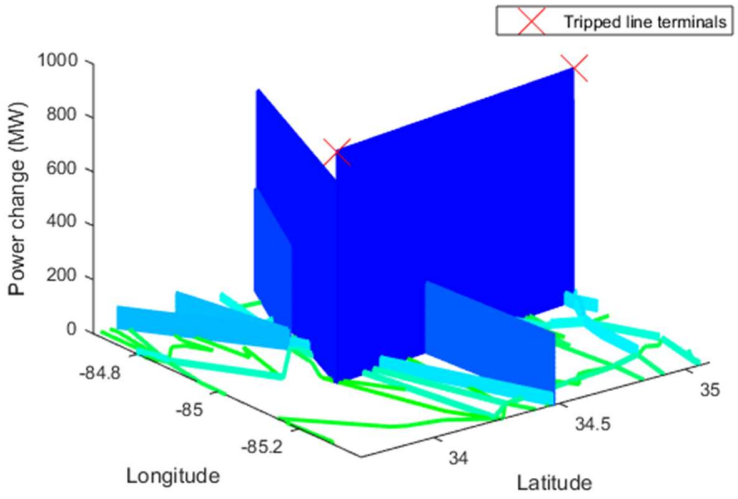

(a)

Figure 4.5. Distribution of power change in TVA system (a) Line4 outage (b) Line5 outage (c) Line6 outage

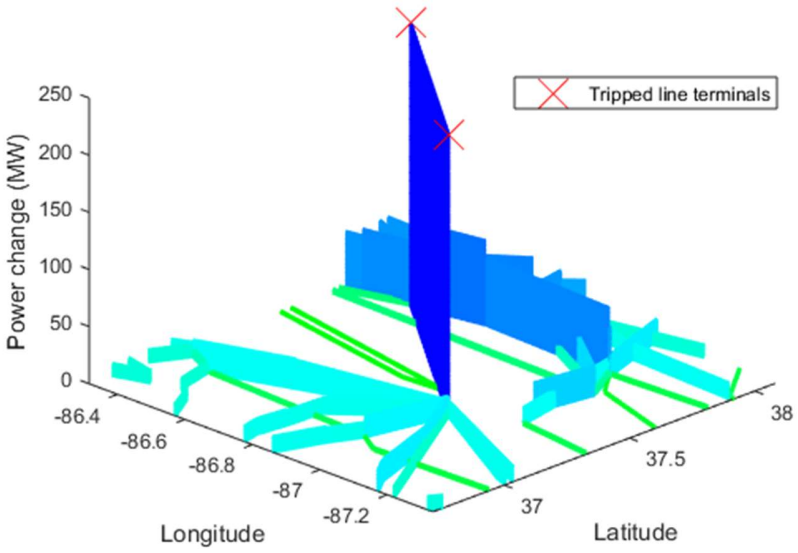

(b)

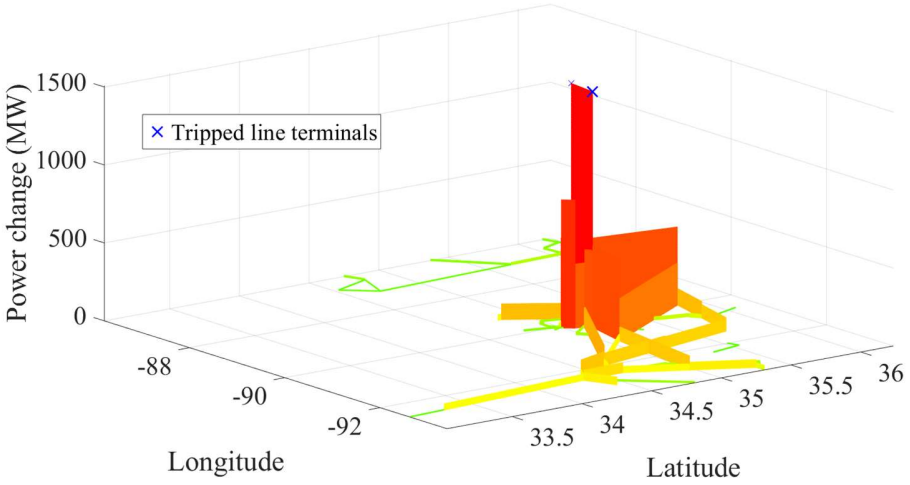

(c)

Figure 4.5 continued

the terminals of the outage line have the highest value for both cases. What is more, the power flow change closer to the outage line generally has a larger value than the line far away from the event location.

4.4 Simulation Study

To verify the effectiveness of the proposed method for line outage detection and localization, a simulation is conducted in ISO-NE which assumes that synchrophasor covers all 345 kV and part of (26%) 230 kV transmission lines. Line outages events are triggered in PSS/E to evaluate the performance of the events at different voltage levels. The parameters of the filter for line outage detection are selected based on [22], which are listed in Table 4.2. The event detection module is implemented in C#, while the location module is developed by MATLAB. The simulation tests are on a computer running a 64-bit Windows 10, with a 3.60 GHz Intel I7-7700U CPU and 16 GB memory.

The line outage events can be successfully detected, and event time can be accurately recorded for all simulation cases. The location estimation of the events is further analyzed. The information of the line outage location and estimation error are in Table 4.3. As shown in Table 4.3, the proposed method is able to identify the outage line location precisely, when the outage lines are monitored by synchrophasor. For the outage lines without synchrophasor monitoring (115 kV), the estimated location is close to actual outage line terminals. For the cases with a large error in the 115 kV case, the actual outage lines are far away from PMU locations and the reported PMU is the closest location to the actual outage line terminals. For the purpose of comparison, the locations of six line outage cases from 115 kV and 345 kV were estimated by the proposed methods and the traditional methods using the maximum frequency magnitude change in Ref. [22] and [103]. The estimation errors for each case are

Table 4.2. Parameter selection for line outage detection

Parameters	Values
Median filter window	7 points
Mean filter size	31 points
Detection window	20 points
First peak threshold	0.0045 Hz
Second peak threshold	0.0025 Hz

Table 4.3. Result of line outage location estimation

Voltage level	Monitored by PMU	Cases numbers	Max error (Mile)	Average error (Mile)
345 kV	Y	37	0	0
230 kV	Y	20	0	0
230 kV	N	8	13.72	6.32
115 kV	N	30	82.49	10.42

given in Table 4.4. The estimation locations and actual line outage for each case are plotted from Fig. 4.6 to Fig. 4.11 As shown in these figures, distances between the estimated locations by proposed methods and the actual location of outage line are small while the estimated location by methods using frequency changes has significant deviations from actual outage locations.

4.5 Conclusion and Future Works

Awareness of line outage event and its location is critical to prevent cascading outages in today's modern power system. This paper presents a fast line outage detection and localization method utilizing high-density synchrophasor measurements. The line outage is first detected via a peak detector on synchronized frequency measurements, and the location of the fault line is directly estimated via active power flow change. The proposed is straightforward and does not need the pre-knowledge on system topology and parameters. The feature of active power change distribution caused by line outage is explored in both TVA and ISO-NE system. A comprehensive simulation study in ISO-NE shows the method can precisely identify the outage line with reasonable accuracy. It can work as an effective tool for real-time line outage detection and localization.

Simulation results manifest that the proposed approach is promising for line outage detection and localization in large-scale power system. The performances of the proposed approach have not been validated with line outage events from a real power grid. Additionally, the approach has not been fully tested for real-time implementation. Following are some future works for further development:

(1). Validate the proposed approach with a confirmed line outage event from utilities.

(2). Test the robustness of the approach with synchrophasor measurements with low data

Table 4.4. Performance comparison for location estimation

Case name	Voltage level	Monitored by PMU	Power flow (MW)	Power change (mile)	Max freq. (mile)
1	345 kV	Y	725.17	0	93
2	345 kV	Y	407.37	0	126.04
3	230 kV	Y	224.43	0	123
4	230 kV	N	285.65	9.366	126
5	230 kV	N	196.61	13.72	196.30
6	115 kV	N	100.45	0	18

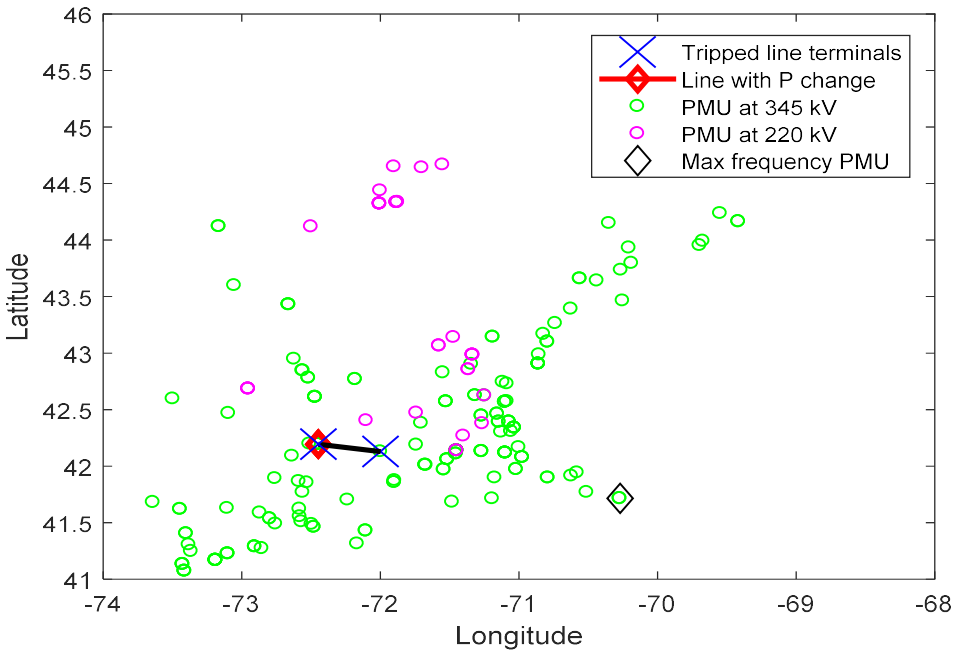

Figure 4.6. Comparison of line outage localization (case 1)

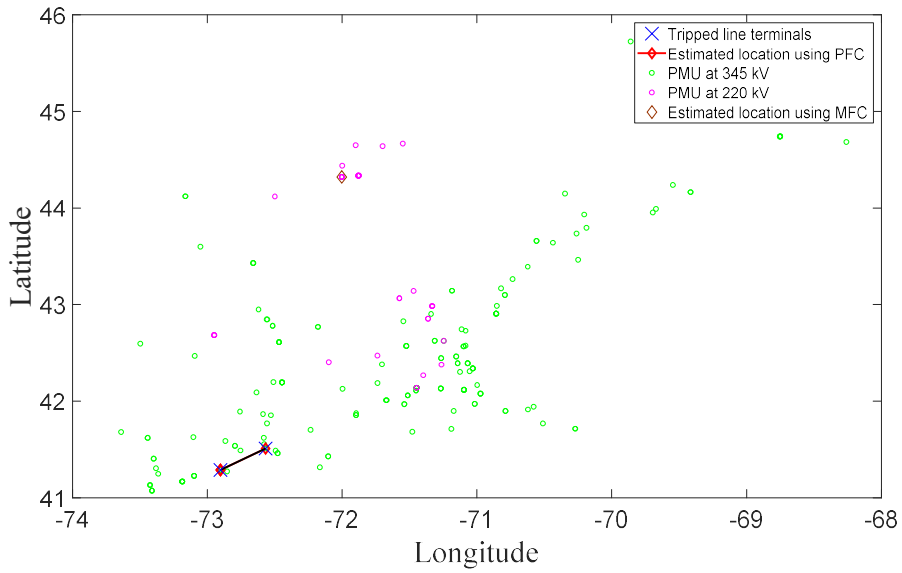

Figure 4.7. Comparison of line outage localization (case 2)

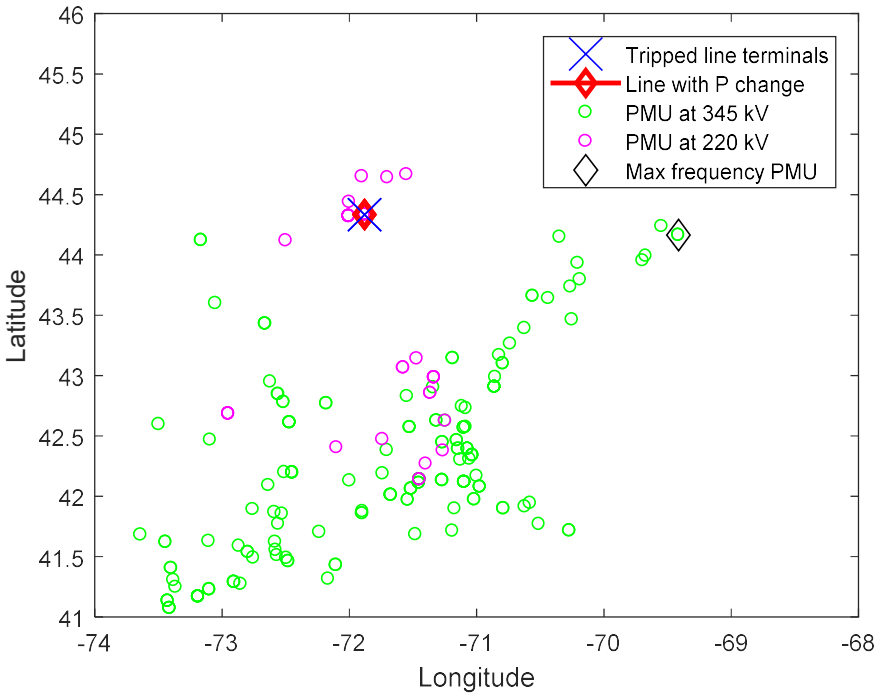

Figure 4.8. Comparison of line outage localization (case 3)

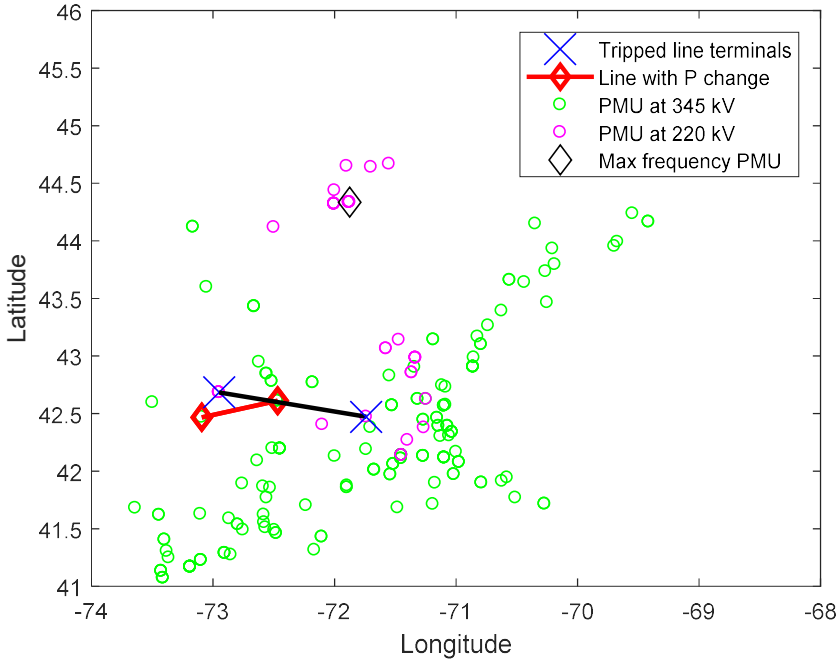

Figure 4.9. Comparison of line outage localization (case 4)

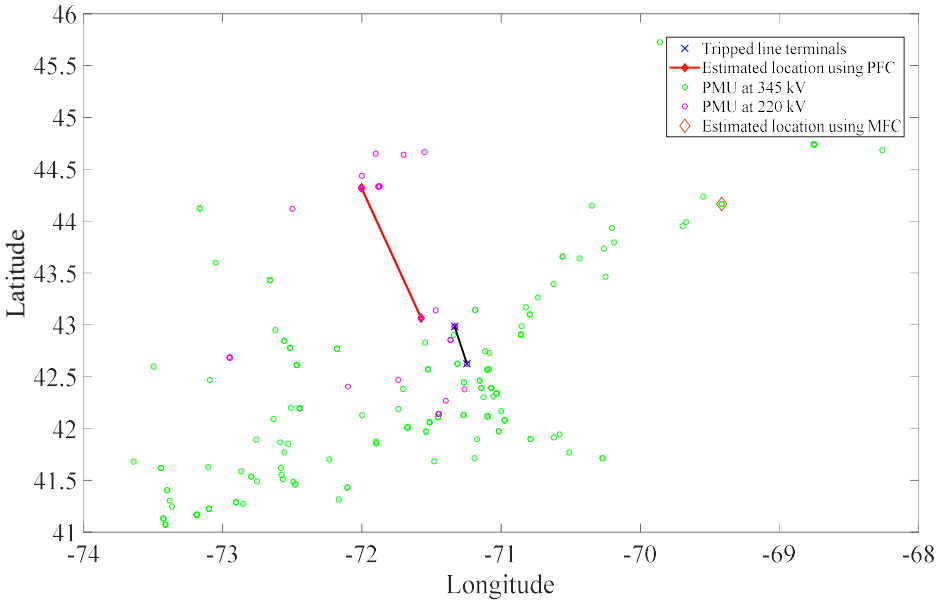

Figure 4.10. Comparison of line outage localization (case 5)

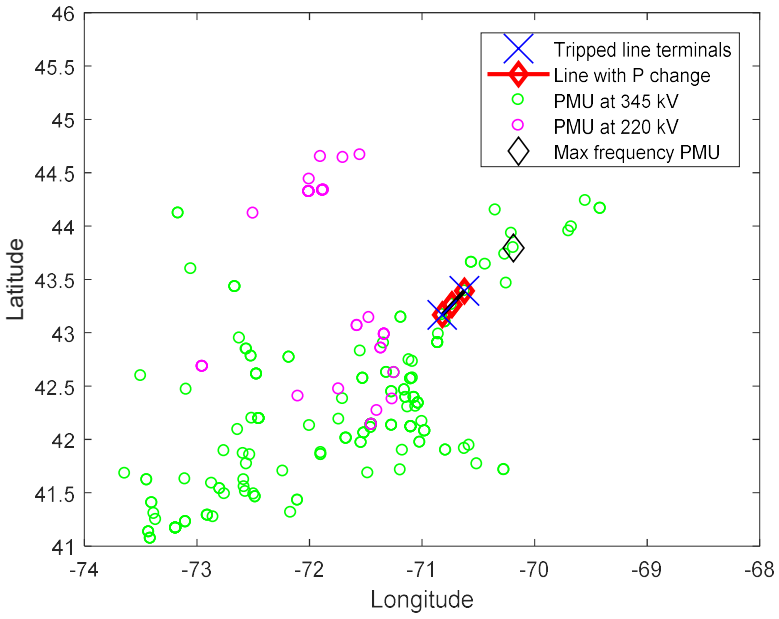

Figure 4.11. Comparison of line outage localization (case 6)

quality.

(3). Implement interface with available PMU data platform and test the approach with real synchrophasor measurements

Acknowledgment

This chapter is, in part, a reprint of the material in the paper: Deng, Xianda., Bian Desong., Shi Di, Yao Wenxuan., Jiang Zhihao., and Liu Yilu., "Line Outage Detection and Localization via Synchrophasor Measurement," in IEEE PES Innovative Smart Grid Technologies (ISGT) ASIA, Chengdu, China, 2019.

Chapter 5 A Novel Deep Learning Model to Detect Various Synchrophasor Data Anomalies

5.1 Introduction

Synchrophasor technology provides high-resolution global positioning system (GPS) time-synchronized phasor measurements [104]-[106]. It reveals unprecedented insights into power grid dynamics and is widely used in applications including disturbance detection, fault location, data mining, cybersecurity [107]-[112], etc.

Since these applications fully depend on synchrophasor measurements, the anomalies in the measurements can impact their performance to various extents. A recent study analyzes the impact of inaccurate synchrophasor measurements on the application disturbance triangulation[113]. According to this work, the location result is sensitive to inaccurate angle measurements when the magnitudes of the disturbances are small. Inaccurate measurements can also affect the accuracy of line outage detection especially noise in synchrophasor measurements is a common issue for the online application [114]. Moreover, incomplete phasor measurement data can have various-scale impacts on fault locations [115] and voltage stability assessment [116].

Due to issues including bad communications, hardware malfunctioning, GPS loss, etc. [117]-[118], anomalies are usually observed in field-collected synchrophasor measurements. To detect data anomalies several model-based methods have been proposed [25]-[31]. However, the model-based approaches heavily depend on knowledge of system topology and model parameters. Their detection performances can be deteriorated when the system topology and the model parameters are unknown. Therefore, data-driven approaches are proposed to detect the

anomalies in the synchrophasor data, eliminating the reliance on the system topology and model parameters. For example, a dimensionality reduction approach is proposed to detect the missing data. However, the computational cost of matrix decomposition is unaffordable for large-scale synchrophasor data. Moreover, a Spatio-temporal approach is proposed to detect the outliers in the synchrophasor measurements [119]. However, this approach may not apply to other data anomaly types. A recent study tries to combine various detectors to provide a comprehensive, unsupervised model to detect missing data and outliers [120]. However, it still cannot cover all data anomaly types due to the heterogeneity of synchrophasor U data anomalies [28].

As aforementioned, anomaly detection in synchrophasor is a rather complex issue. (1) Many approaches are targeted at specific types of abnormalities and cannot work with others. (2) Parameter tuning of models can be rather tricky and it usually requires prior knowledge. (3) Some models require high computational efforts and are hard to implement in real-time.

To address these issues, this paper exploits the power of deep learning, proposing a convolutional neural network (CNN) model to detect various PMU data anomalies. The contribution of this works is four folds.

1). A CNN model is proposed to detect various PMU data anomalies.

2). Over 1500 field-collected ambient samples from Jiangsu, China, including both normal and anomaly data, are manually labeled to train and test the model.

3). The proposed model is extensively evaluated and is proved to achieve superior detection accuracy on all anomalies.

4). The proposed model is compared with several traditional methods

5.2 Proposed deep CNN structure

As present in the previous section, the patterns of the synchrophasor data anomalies are varied and random. Additional, good synchrophasor measurements also keep fluctuating around system nominal value due to system operation statues and unbalance between generation and load. Deep learning CNN is characterized by automatically retrieve significant features without human knowledge, compared to traditional mathematical, statistical methods, and other machine learning methods. It makes deep learning CNN a distinguishing method to detect and classify the diversified data anomalies issue in high-resolution synchrophasor measurements. First, this section introduces the design of the input dataset, label, and data preprocessing. Then, the overall structure of the proposed CNN network structure, hyper-parameters are described and the features extracted in the proposed structure are also presented. Finally, the techniques used to reduce the overfitting issue are introduced.

5.2.1 Dataset design, labeling and data pre-processing

In real-time applications, the measurements from one synchrophasor are consecutive with time stamps. For real-time application consideration, each data set only contains measurement from a single PMU measurement point and the measurements are aligned with time sequence. The size of the dataset intends to be minimized, thus data anomalies will be detected and identified in a short period for further appropriate treatment or data recovery. On another side, considering the complicated patterns of the aforementioned practical PMU data anomalies, a large-size of consecutive measurement in the dataset will provide essential information for better judgment of the anomalies type and labeling. To compromise between the efficiency and accuracy, 100 consecutive measurements of one PMU are selected as one dataset. The labels of the dataset are categorized into 4 types:

1. Good measurement
2. Spiking/Missing anomalies
3. High frequency noise anomalies
4. Erroneous pattern anomalies

Input normalization is an essential step for improving the converge and speed of CNN network. The purpose of input normalization is to reduce the deviation of input data. In practical PMU measurements, the normal measurements and some of the data anomalies are around nominal value while the spikes or missing data may have large deviations from the nominal value. It will cause CNN to over-compensate in training process for one particular type of anomalies and reduce sensitivity for other anomalies. Thus, the raw PMU measurements are pre-processed with the following steps:

1) For the ith measurement, find the maximum value f_{max}^{i} and the minimum value f_{min}^{i}
2) Normalized the ith measurement using the following equation,

$$f_{j,norm}^{i} = \frac{f_j^i - f_{min}^i}{f_{max}^i - f_{min}^i} \tag{5.1}$$

where f_j^i represents the jth sample of the ith measurement.

3) Each normalized measurement will be in the range of [0,1]. It should be noticed that if all measurements in the type of constant measurements anomaly is a pure DC signal in some cases, so all the measurements in the samples with DC signal measurements are set to 0 in the normalization.

5.2.2 Design network structure

The proposed deep CNN structure is shown in Fig. 5.1. It contains 4 layers of convolutional layers, 3 layers of max-pooling layers, and n layers of fully-connected layers. Each type of the layers is described respectively below.

(1) Convolutional Layers

The convolutional layers are implemented to extract the spatio-temporal features by kernels. Each kernel converts the input measurements by

$$S(i,j,f) = M_{m' \times n'}\ (i - m'\ , j - n'\ )K_{m' \times n'}\ (f) \qquad (5.2)$$

where $S(i,j,f)$ is the signal value at coordinates (i, j) in feature map f after convolution, $M_{m' \times n'}$ is the input measurements, $K_{m' \times n'}(f)$ is the kernel at feature map f. In (1), m' is the width of the kernel, which is less than the input width m, and n' is the height of the kernel, which is less than the input height n. In this paper, since the input data is flattened, (1) can be further written as

$$S(i,1,f) = M_{m' \times 1}(i - m'\ , 0)K_{m' \times 1}(f) \qquad (5.3)$$

The first two convolutions layers CL1 and CL2 connect to the normalized input dataset and extract 100 features, which are shown in Fig. 5.2 (b) and (c). The CL3 and CL4 layers extract 200 features, which are presented in Fig. 5.2 (d) and (e), from the output of max-pooling layers MP1.

(2) Max-pooling Layers

Max-pooling layers abstract the output from the convolutional layers by applying max filters on the output. Max-pooling layers not only reduce the size of the extracted features by retaining

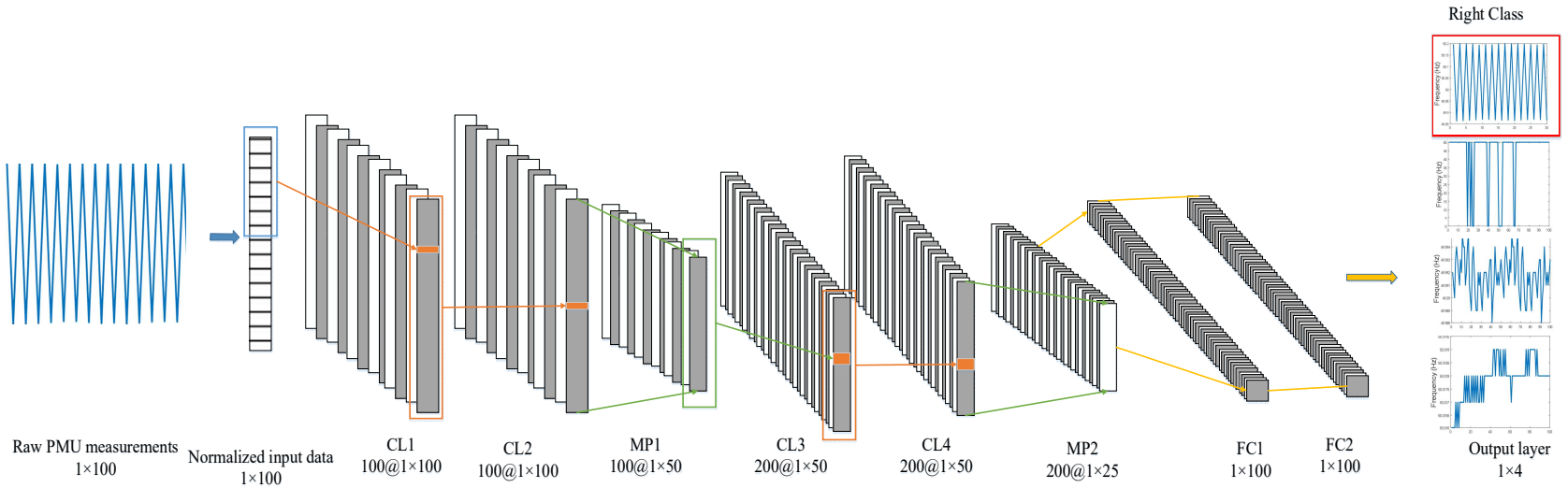

Figure 5.1. Structure of proposed deep CNN

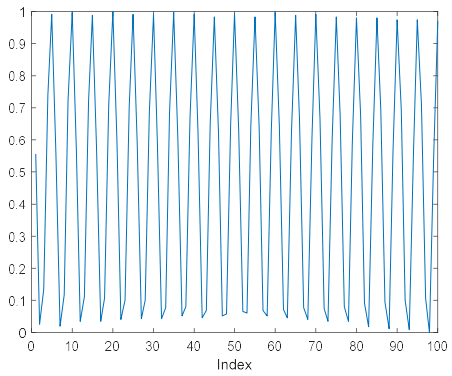

(a)

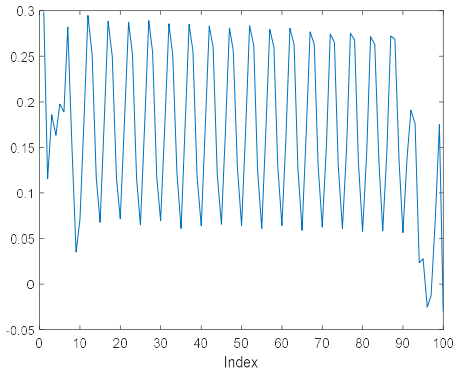

(b)

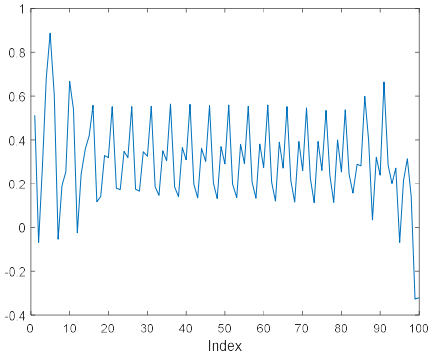

(c)

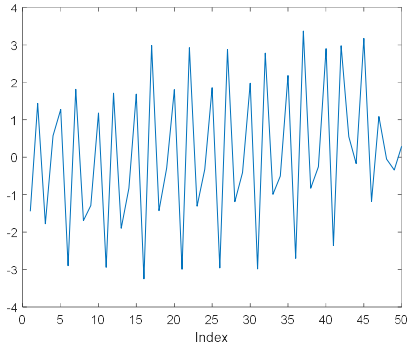

(d)

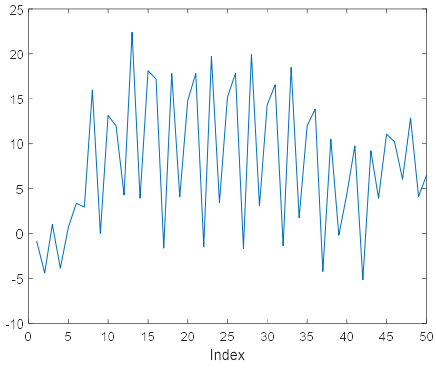

(e)

Figure 5.2. Extracted features of a high frequency noise anomalies sample from Deep CNN (a). Normalized frequency, (b). Feature from CL1 (c). Feature from CL2 (c). Feature from CL3 (d). Feature from CL4

representative information, but also tend to prevent overfitting. The max-pooling used in the structure is presented as

$$MP(i,1,f) = max\{S(i,1,f),\dots,S(i+,1,f)\} \tag{5.4}$$

(3) Fully-connected Layers

A 2^n fully-connected layers using softmax are connected to the output of MP2 to perform classification. Output feature maps after the last max-pooling layer are appended to a vector $output\_1_{lm\times 1}$, where $lm = nf \times fm$, $nf$is the number feature maps and fm is the final width of each feature map. Fully-connected layers classify the data by

$$output\_2_{1\times c} = output\_1^{T}_{lm\times 1} \times w_{lm\times c}, \tag{5.5}$$

5.2.3 Techniques for overfitting

Overfitting is a general issue, which is caused by too complicated network and closed fitting to training dataset for deep learning methods. Overfitting will reduce the capability of deep CNN for generalizing and estimating with the new dataset. As result, the accuracy of a CNN model with the overfitting issue will decrease after epochs in the training process reach a certain point. There are many effective methods, which have been developed to address the overfitting issue, such as data augmentation, regulation, etc [121]. The two regularization techniques used in the proposed networks introduces:

(1) Dropout

Dropout technique is to randomly abandon a portion of the neurons of a deep learning model in each cycle of a training process. Since the root cause of overfitting is that neighboring neurons over relay a certain specific feature of training dataset during neuron weights tuning process, randomly dropout neurons will make the network predicting for the disabled neurons. In

the proposed model, two dropout layers are implemented in after each full-connected layer. The percentage of dropout neurons, dropout rate, are tuned and presented in the following section.

(2) L2 regularization

L2 regularization, weight decay regulation, is one of the most common techniques for the overfitting issue in deep learning models. The idea of L2 regularization is to add the sum of the squares of all the weights in the network into the cost function during the backpropagation process, which is presented as:

$$Cost\ function = loss + \frac{\lambda}{2n}\sum_{\omega}\omega^2 \tag{5.6}$$

where the loss is the cross-entropy loss calculated in the backpropagation. ω is the weight in the network and n is the side of the training set. The regularization term is the sum of all the weights in the fully-connected layers. $\lambda>0$ is the regularization parameter, and n is the size of the training set. The cost function is calculated as the sum of cross-entropy loss and a regularization term. The extra term forces the network preferring small weights in the training process and it guarantees that no specific feature will be over-relied in the network. The regularization parameter λ is tuned and presented in the following sections.

5.3 Performance evaluation

5.3.1 Dataset and tentative test

The evaluation of the proposed deep learning CNN structure use field-collected PMU frequency measurements from a Jiangsu power grid. The PMU deployed in Jiangsu power grid is plotted in Fig 3.1. The nominal frequency of the power grid is 50Hz. The PMU frequency measurements are collected from 155 PMUs and the sample ratio of the PMUs in the power grid

is 25 Hz. All the PMU measurements are collected under normal operation status of the power grid. As discussed in Section 1, 1150, and 350 datasets are created and labeled based on the author's judgment for training and testing the proposed model. The detail of the training and testing dataset are summarized in Table 5.1.

For a tentative purpose, the kernel size and learning rate in the proposed model are initially selected as 5 and 0.01 respectively. The proposed model is trained for 50 epochs. The training and testing convergence and accuracy in each epoch are plotted in Fig 5.3. The proposed model achieves 100% accuracy in training while the best testing accuracy is 95.8%. However, it should be noticed that testing accuracy achieves almost 100% after 38 epochs, but the training accuracy doesn't increase significantly. The testing cost curve slightly increases after 38 epochs, which indicates that the proposed model with initially selected parameters has an overfitting issue. The training and testing results show that the proposed structure with four convolution layers and two max-pooling layers are sufficient to extract the features of the data anomaly and system fluctuation during normal operation in the dataset. To further validate the structure of the proposed model in the tentative test, Deep learning CNN models with 2 to five convolutional layers are implemented, trained, and tested with the same parameters in the previous test. The accuracy of the models in the tests is compared in Figure 5.4. The accuracy of the models rises as the hidden layers of the models increase, and the four layers model achieve the best performance. When the layers increase to 5 layers, the accuracy drop, due to the overfitting issue, which a common issue to a complex model.

5.3.2 Hyper-parameters evaluation

To address the overfitting issue in the proposed model, the drop-out and regularization techniques are applied in the proposed model. The hyper-parameters including kernel size,

Table 5.1. Summary of training and testing data set

Dataset name	Data types	Number of measurements
Training	Good	729
	EP,	266
	RS/ MP	91
	HFN	64
	Total	1150
Testing	Good	252
	EP,	66
	RS/ MP	7
	HFN	25
	Total	350

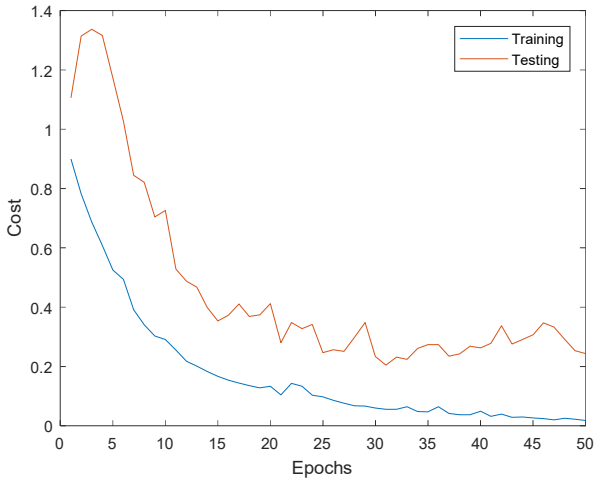

(a)

Figure 5.3. Convergence and accuracy comparison of the tentative test (a). Convergence (b).

Accuracy

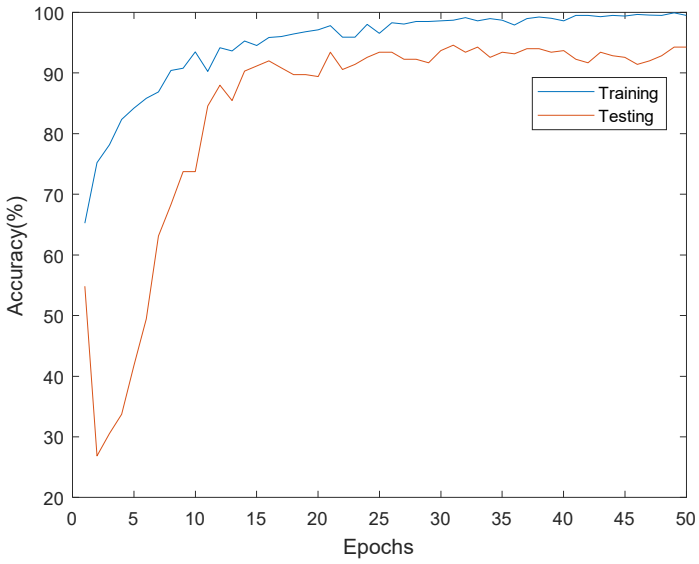

(b)

Figure 5.3 continued

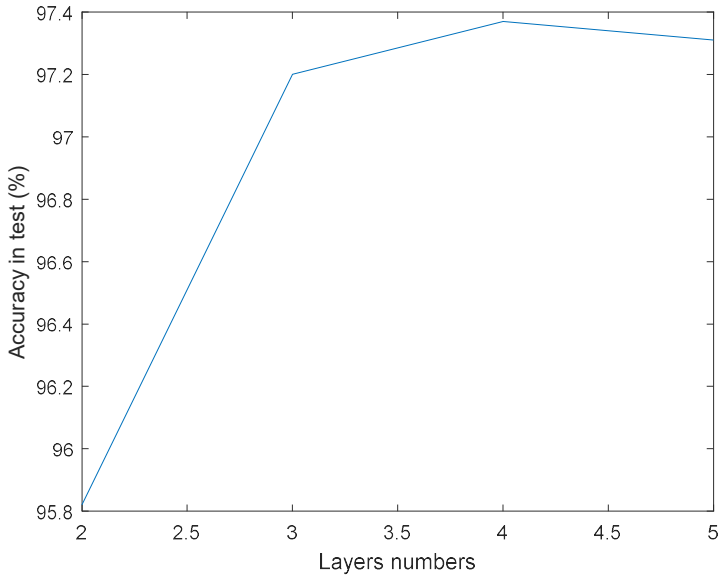

Figure 5.4. Test accuracy comparison of models with different layers

drop-out rate, and regularization parameter, affect the performance of the model. In this paper, an extensive study of the hyper-parameters is conducted to evaluate the effects of these hyper-parameters. In the evaluation, the same sample sets, epoch number, and learning rate are used as in section 5.3.1.

(1) Kernel size

To evaluate the impacts of the kernel size, the kernel size in the proposed CNN model is increased from 1 to 20. The best accuracies in training and testing achieved by each kernel size are presented in Fig 5.5. The training accuracy reaches 99.83 % after the kernel size is larger than 10. The testing accuracy slightly increases after the kernel size is larger than 8. The best accuracy of the testing result is 97.14%. It indicates that the kernel size has limited impacts on training accuracy and overfitting issue when it research certain thresholds. The best accuracy of kernel size 19 is selected at the following evaluations.

(2) Dropout rate and regularization parameter

Both dropout and L2 techniques are utilized to improve the overfitting issue. As discussed in the aforementioned section, the dropout and L2 used different mechanisms to improve the overfitting issue, the combination of both techniques doesn't guarantee the best performance of the proposed model. Thus, the hyper-parameters in both techniques are evaluated simultaneously and the best accuracy of each combination is present in Fig 5.6 and Fig. 5.7.

As shown in Fig. 5.7, a larger dropout rate and smaller λ result in better accuracy in the training results. The proposed model achieves 100% accuracy in training when the dropout rate$\geq$0.5 and $\lambda \leq 0.01$. For the testing results, 6 combinations of the dropout rate and λ achieve the

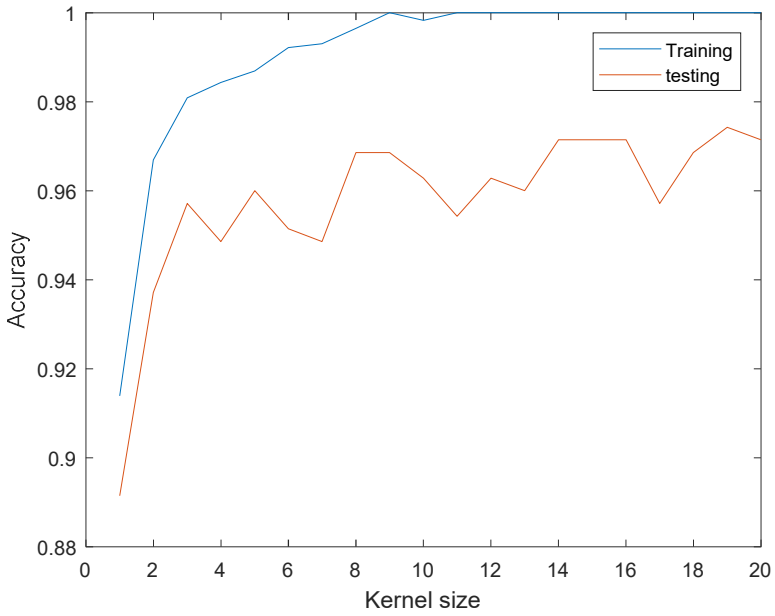

Figure 5.5. Accuracy comparison with different Kernel sizes

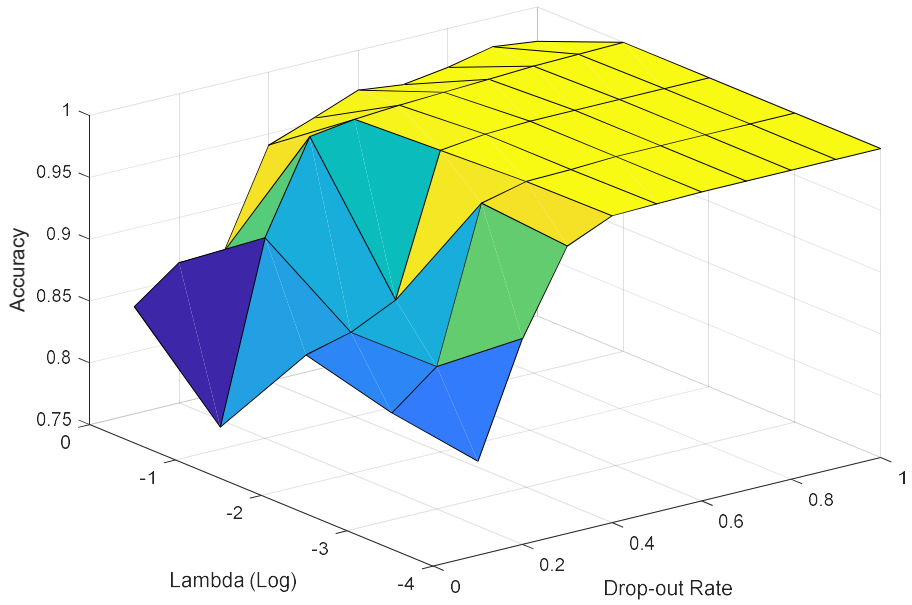

Figure 5.6. Training accuracy evaluation with L2 and drop-out regulation

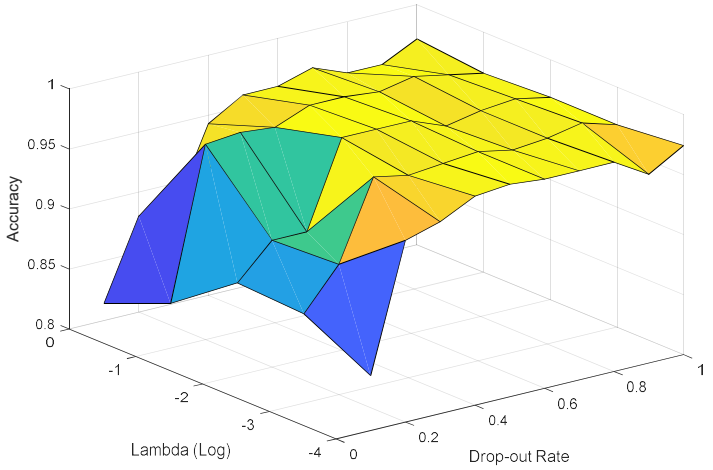

Figure 5.7. Testing accuracy evaluation with L2 and drop-out regulation

best accuracy of 97.71%, but major ranges of the parameters are 0.4≤dropout rate≤0.6 and λ=0.01. It also indicates that the accuracy drops when the dropout is too high or λ is too low.

Comparing to the best accuracy in the previous scenario, overfitting is slightly improved.

The limited improvement of dropout and L2 techniques in the proposed model can be contributed to two factors: (a). the best accuracy of the previous scenarios is considered very high, the improvement space is limited. (b). The size of the training and testing dataset is relatively small. However, it should be noticed that the dataset used in the evaluation may not be utilized traditional data augmentation techniques, due to the RP and EP types.

5.3.3 Evaluation Metrics

To further evaluate the complete performance of the proposed model results, the false classified samples in the previous best scenarios are identified. Precision and recall, popular metrics in machine learning classification, are used to analyze the performance of misclassification in the proposed model.

(1) Evaluation Metrics

In the precision and recall metrics, a model classification results are categorized based on the true/false classification results [122]. The confusion matrix in the testing at the best scenario of the proposed model is summarized in Table 5.2

In a classification task, precision reflects the percentage of the actual good measurement samples in the classified good measurement samples by a model. It can be calculated by

$$precision = \frac{TP}{(TP+F\ )} \tag{5.7}$$

$$recall = \frac{TP}{(TP+FN)} \tag{5.8}$$

Table 5.2. Confusion matrix of the proposed deep learning model

		Actual			
Predicted		Good	EP	RS/ MP	HFN
	Good	247	0	1	1
	EP	3	66	1	0
	RS/ MP	2	0	5	0
	HFN	0	0	0	24
	Total	252	66	7	25

On the other side, recall indicates the percentage of the actual good measurement samples are classified by a model, which can be presented as

Based on Table 5.2, the precision and recall of the proposed model achieved in the best scenario are 0.9919 and 0.9761. Both high precision and high recall indicate the proposed model is able to detect the data anomaly sample and classified into correct types in high confidence while there is a low chance to misclassify a good measurement sample as abnormal data.

(2) Cross-validation

To further evaluate the performance of the proposed model, 200 samples of the training and testing dataset used in the previous section are randomly exchanged five times and used as datasets in cross-validation. The details of the new dataset are listed in Table 5.3. In Table 5.3, the numbers of data anomaly in each combination are organized as training samples/testing samples.

Each dataset is trained and tested as in the aforementioned section and the best accuracy of cross-validation results are listed in Table 5.4. As shown in Table 5.4, the testing accuracy in cross-validation indicates the proposed model achieves similar performances with different combinations of the training and testing dataset.

(3) Compassions

To compare the performance of the proposed CNN with some common used outlier classifications methods, Support Vector Machine (SVM), Artificial Neural Network (ANN), Principal Components Analysis-SVM (PCA-SVM), and the Long Short Term Memory (LSTM) are implemented and tested with the normalized dataset used in section 5.4.2.. The Radial Basis Function (RBF) kernel is selected in SVM. For ANN, the two-layer structure is used. To

Table 5.3. Summary of training and testing dataset in cross-validation

Dataset	Good	EP	RS/ MP	HFN
1	748/233	264/68	71/27	67/22
2	740/241	257/75	86/12	67/22
3	754/227	255/77	81/17	60/29
4	748/233	261/71	80/18	61/28
5	744/237	258/74	82/16	66/23

Table 5.4. Trainingand testing accuracy in cross-validation

Dataset	Training accuracy	Testing accuracy
1	100%	96.29%
2	100%	97.42%
3	100%	96.29%
4	100%	98.29%
5	100%	98.86%

Table 5.5. Comparison results of different methods

Methods	Structure	Average accuracy
ANN	Nodes: 100-50-20	89.14 %
SVM	RBF kernel	92.28 %
PCA-SVM	10 Principal Components	68.00 %
LSTM	4 layers with 120 hidden units	88.00 %
Proposed CNN	Four convolutional layers	97.43 %

compare with the dimensional compression method, the PCA and SVM are combined to achieve feature extraction and classification capabilities. As can be seen from Table 5.5. The SVM performs better than the ANN and LSTM. However, the result of PCA-SVM is 64.57 % and it is not as good as SVM, which indicates that there may be a loss of information during the PCA process. Overall, the proposed CNN obtains the best accuracy.

5.4 Conclusion

Real-world synchrophasor measurements have anomalies issues including erroneous pattern, random spike, missing point, and high frequency components, which would degrade the performance of synchrophasor based applications. In this paper, a deep learning approach is proposed for the detection of synchrophasor anomalies using a convolutional neural network，which could help the system operators know the quality of synchrophasor measurements in real-time. To evaluate the performance of the proposed network, experiments are conducted using field-collected synchrophasor in Jiangshu Power grid. The test results show the proposed model can achieve an accuracy of 97.71%, which demonstrates the proposed CNN can effectively detect abnormality in synchrophasor measurements.

Acknowledgment

This chapter is, in part, a reprint of the material in the paper: Xianda Deng, Weikang Wang, Zhihao Jiang, Wenxuan Yao, Ning Tong, and Yilu Liu, “A Novel Deep Learning Model to Detect Various Synchrophasor Data Anomalies”, *IET Generation, Transmission & Distribution, accepted*

Chapter 6 Non-Contact Synchronized Measurement Using Electric Field Study

6.1 Introduction

As vital components of a wide area monitoring system, traditional synchrophasor measurement units are usually installed at potential transformers (PTs) and current transformers (CTs) of a bus or power line [123]. The installation and maintenance cost of a synchrophasor measurement unit, especially in a transmission network, is expensive. According to [124], the installation cost of one single transmission-level synchrophasor measurement unit is over $8,000. However, developing low cost synchrophasor measurement unit is one of the evolution directions for synchrophasor technology [125]. Synchrophasor measurement unit with features of flexible installation and easy to maintain is desired for large-scale applications in power grids.

As a pioneer of synchrophasor technology, PowerIT group in the University of Tennessee at Knoxville (UTK) designed a non-contact synchronized measurement unit by utilizing electric field generated by power line [126]. One of the key designs in the [126] is that it uses copper as electric field sensor. The alternative electric field generated by power lines induces voltage signals on the sensors. Then, the voltage signal is processed and calibrated to the power line voltage. The hardware design of the non-contact synchronized measurement unit is shown in Fig. 6.1. A prototype of the non-contact synchronized measurement unit was implemented and tested under a 500 kV transmission line at Knoxville, Tennessee. The field testing results demonstrate the feasibility of the non-contact synchronized measurement unit with low cost and flexibility.

In traditional power line measurement, researches and developments have been investigated using alternative electric field to measure power line voltage [127]-[132]. It measures electric

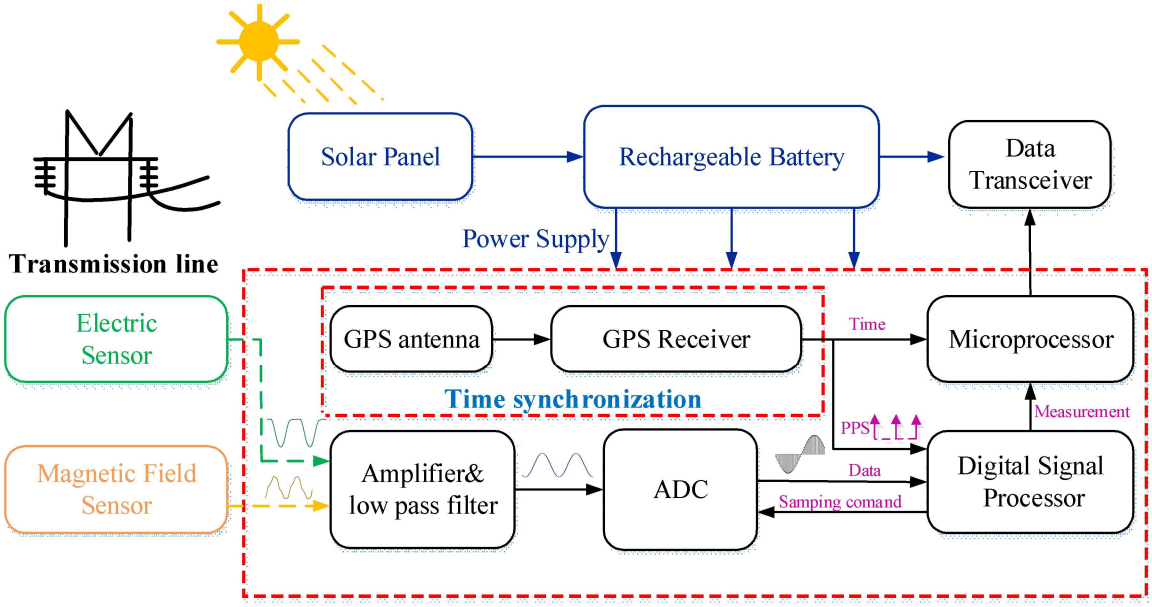

Figure 6.1. Hardware design of non-contact synchronized measurement unit by UTK[126]

field vectors generated by power line, which requires an expansive and sophisticated electric field sensor. Then, the power line voltage can be calculated by electromagnetic theory with the measured electric field vector. On the other side, the electric field strength meter is very mature with a lower cost. Using electric field strength to determine voltage may reduce the cost of the solution significantly. Meanwhile, it may provide a potential solution to improve measurement accuracy for the non-contact synchronized measurement unit. In this chapter, the theoretical foundation of calculating power line voltage via electric field strength is discussed. The calculating process and equations are derived for a single circuit AC transmission line and a double circuit AC transmission line respectively. The derived equations and calculating process are implemented in Matlab code and tested with a 525 kV single circuit transmission line and double circuit transmission line configurations from [133]. The simulation testing results show that the proposed method can determined power line voltage via electric field strength with high accuracy.

6.2 Theoretical foundation and equation derivation

In this section, the theoretical foundation of calculating transmission line voltage level via electric field strength are discussed. The calculating process is derivated for both single circuit and double circuit transmission line configurations.

6.2.1 Single circuit transmission line

According to [133], the traditional configurations of three-phase single circuit transmission lines are categorized into three types: horizontal, vertical and delta configuration. In this section, a horizontal configuration is utilized in the equation derivation, but the derivate equations are valid for the three configurations.

As defined in [133], the electric field of a power line can be calculated by superimposing the electric field generated by each power line conductor. A traditional infinite and balanced model of single circuit three-phase transmission line is used for electric field calculation and presented in Fig. 7.1. The following are the assumptions and simplifications used in this chapter.

(1). Conductor positions and GMR

The coordinates of the transmission line conductors of phases a, b and c are defined as (X_a, Y_a), (X_b, Y_b) and (X_c, Y_c). The coordinates of transmission line conductors may vary depending on different transmission line configurations. For one transmission, the coordinates are assumed constants once the transmission line is constructed. For each phase of conductors, it may consist of one or multiple bundle conductors. The bundle conductors can be converted into an equivalent tubular conductor with the equations defined in [133]. The radius of the equivalent tubular conductor is defined as r_{bund}, which is determined by the actual conductor type and bundles numbers. Both conductor radius and coordinates in the chapter are referred to as the equivalent conductor.

(2). Ground effects

The energization of the conductors generates charges both on the conductors and in the ground under the conductors. The ground effect is simulated by placing image conductors as shown in Fig. 6.2. The image conductors carry negative charges and are placed under the ground level. The bundled conductors of the transmission line are converted into equivalent conductors.

As shown in Fig. 6.2, an electric field sensor is placed at location s and the coordinate is defined as x_s and y_s. Since the sensor is placed on the ground, y_s is set to 0. The electric field

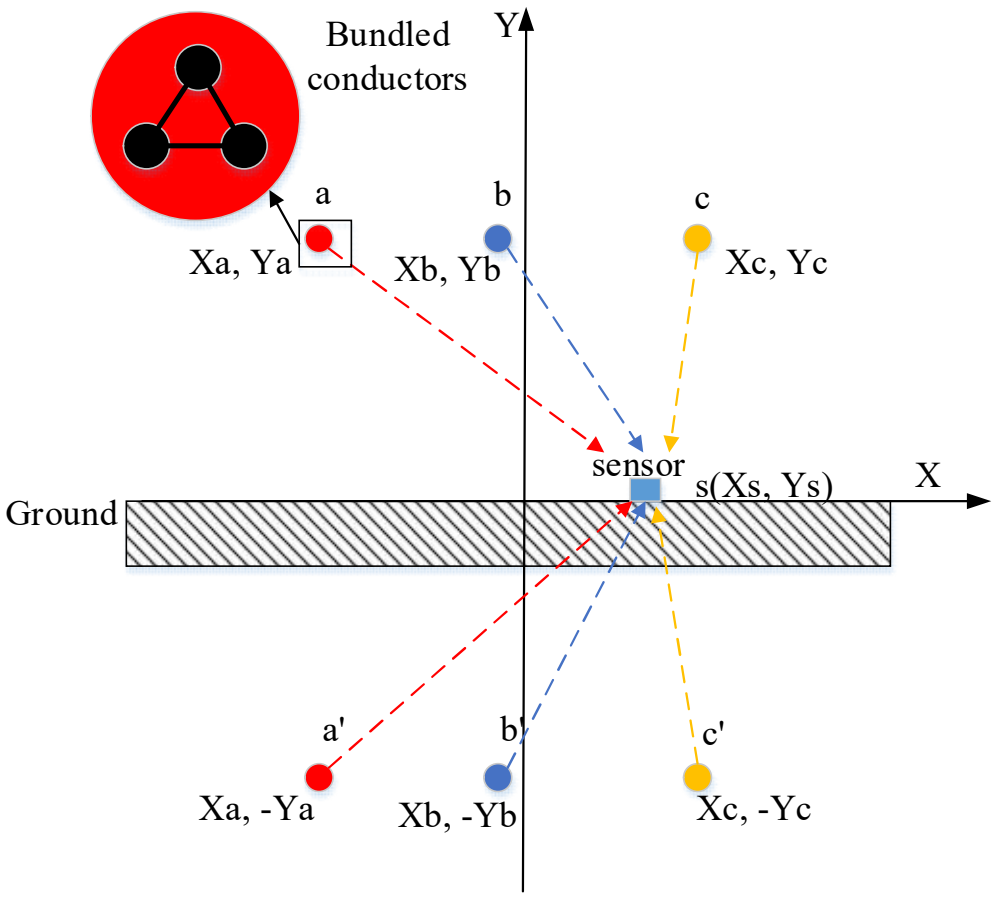

Figure 6.2. Transmission line horizontal configuration and sensor position

strength measured by the sensor is E_m. It is assumed that the voltage of the transmission line is balance and line to ground voltage of the conductors are defined as:

$$\boldsymbol{V_{ap}} = V_{lg}cos(2\pi ft + \beta) = V_{lg}\angle 0^o \tag{6.1}$$

$$\boldsymbol{V_{bp}} = V_{lg}cos(2\pi ft + \beta + 120°) = V_{lg}\angle 120^o$$

$$\boldsymbol{V_{cp}} = V_{lg}\cos(2\pi ft + \beta + 240°) = V_{lg}\angle 240^o$$

where β is the initial angle and V_{lg} is the line to ground voltage.

Equation (6.1) can be converted into complex format:

$$\boldsymbol{V_{ap}} = V_{ar} + V_{ai}i \tag{6.2}$$

$$\boldsymbol{V_{bp}} = (V_{ar} + V_{ai}i) \times (-0.5 + 0.866i)$$

$$\boldsymbol{V_{cp}} = (V_{ar} + V_{ai}i) \times (-0.5 - 0.866i)$$

where V_{ar} and V_{ai} are the real and imaginary parts of voltage in phase a respectively and two unknown variables to be determined below.

As defined in [133], for an energized transmission line, the voltage differences between conductors and ground can be calculated by

$$V_{kl} = \frac{1}{2\pi\varepsilon_0}\sum_{l=1}^{m} q_{con\_k}\ln\left(\frac{D_{kl\prime}}{d_{kl}}\right) \tag{6.3}$$

where q_{con_k} is charges on the conductors and shield wires on a transmission line. *k,* d_{kl} and $D_{kl\prime}$ are the distances from conductor *k* to conductor *l* and its image conductor *l'* respectively. *m* is the number of overhead conductors and shield wires. *k*, *l*=1,2,3,……, *m*. ε_0 is vacuum permittivity and select $\varepsilon_0 = 8.854 \times 10^{-12}F/m$.

Equation (6.3) can be presented in a matrix form as:

$$\boldsymbol{V} = \boldsymbol{PQ} \tag{6.4}$$

where $\boldsymbol{P}$ is potential coefficients of a transmission line, which can be determined by

$$P_{kl} = \frac{1}{2\pi\varepsilon_0}\sum_{l=1}^{m} \ln\left(\frac{D_{kll}}{d_{kl}}\right) \tag{6.5}$$

For the single circuit transmission line shown in Fig. 6.2, the distant from conductor k to the actual conductors and image conductors can be determined in matrix form as

$$\boldsymbol{d} = \begin{bmatrix} r_{\text{bund}} & \sqrt{(x_a - x_b)^2 + (y_a - y_b)^2} & \sqrt{(x_a - x_c)^2 + (y_a - y_c)^2} \\ \sqrt{(x_b - x_a)^2 + (y_b - y_a)^2} & r_{\text{bund}} & \sqrt{(x_b - x_c)^2 + (y_b - y_c)^2} \\ \sqrt{(x_c - x_a)^2 + (y_c - y_a)^2} & \sqrt{(x_c - x_b)^2 + (y_c - y_b)^2} & r_{\text{bund}} \end{bmatrix} \tag{6.6}$$

$$\boldsymbol{D} = \begin{bmatrix} 2y_{\text{a}} & \sqrt{(x_a - x_b)^2 + (y_a + y_b)^2} & \sqrt{(x_a - x_c)^2 + (y_a + y_c)^2} \\ \sqrt{(x_b - x_a)^2 + (y_b + y_a)^2} & 2y_{\text{a}} & \sqrt{(x_b - x_c)^2 + (y_b + y_c)^2} \\ \sqrt{(x_c - x_a)^2 + (y_c + y_a)^2} & \sqrt{(x_c - x_b)^2 + (y_c + y_b)^2} & 2y_{\text{a}} \end{bmatrix} \tag{6.7}$$

As a consequence, potential coefficients $\boldsymbol{P}$ can be calculated by submitting (6.6) and (6.7) into (6.5). To calculate charges on the conductor and shield wires $\boldsymbol{Q}$, Equation (6.4) is inversed as:

$$\boldsymbol{V} = \boldsymbol{P^{-1}Q} \tag{6.8}$$

and the inversion of potential coefficients $\boldsymbol{P}$ for the transmission line can be presented as:

$$\boldsymbol{P^{-1}} = \frac{1}{p_{11}(p_{22}\times p_{33} - p_{23}\times p_{32}) - p_{21}(p_{12}\times p_{33} - p_{13}\times p_{32}) - p_{31}(p_{12}\times p_{23} - p_{13}\times p_{22})} \times$$

$$\begin{bmatrix} p_{22} \times p_{33} - p_{23} \times p_{32} & p_{13} \times p_{32} - p_{12} \times p_{33} & p_{12} \times p_{23} - p_{23} \times p_{22} \\ p_{23} \times p_{31} - p_{21} \times p_{33} & p_{11} \times p_{33} - p_{13} \times p_{31} & p_{21} \times p_{13} - p_{11} \times p_{23} \\ p_{21} \times p_{32} - p_{22} \times p_{31} & p_{12} \times p_{31} - p_{11} \times p_{32} & p_{11} \times p_{22} - p_{21} \times p_{12} \end{bmatrix} \quad (6.9)$$

For a simplification purpose, $\boldsymbol{P^{-1}}$ is presented in the following format and each element of the matrix is known:

$$\boldsymbol{P^{-1}} = \begin{bmatrix} {p^{-1}}_{11} & {p^{-1}}_{12} & {p^{-1}}_{13} \\ {p^{-1}}_{21} & {p^{-1}}_{22} & {p^{-1}}_{23} \\ {p^{-1}}_{31} & {p^{-1}}_{32} & {p^{-1}}_{33} \end{bmatrix} \quad (6.10)$$

Submitting equations (6.2), (6.10) into equation (6.8) and the relationship between charges and voltages can be built:

$$Q_a = (V_{ar} + V_{ai}i\,) \times {p^{-1}}_{11} + (V_{ar} + V_{ai}i) \times (-0.5 + 0.866i) \times {p^{-1}}_{12} + (V_{ar} + V_{ai}i) \times (-0.5 - 0.866i) \times {p^{-1}}_{13} \quad (6.11)$$

$$Q_b = (V_{ar} + V_{ai}i\,) \times {p^{-1}}_{21} + (V_{ar} + V_{ai}i) \times (-0.5 + 0.866i) \times {p^{-1}}_{22} + (V_{ar} + V_{ai}i) \times (-0.5 - 0.866i) \times {p^{-1}}_{23}$$

$$Q_c = (V_{ar} + V_{ai}i\,) \times {p^{-1}}_{31} + (V_{ar} + V_{ai}i) \times (-0.5 + 0.866i) \times {p^{-1}}_{32} + (V_{ar} + V_{ai}i) \times (-0.5 - 0.866i) \times {p^{-1}}_{33}$$

For a simplification purpose, equations (6.11) can be expressed as

$$Q_a = K_a(V_{ar} + V_{ai}i\,) \quad (6.12)$$

$$Q_b = K_b(V_{ar} + V_{ai}i\,)$$

$$Q_c = K_c(V_{ar} + V_{ai}i\,)$$

where K_a, K_b and K_c are the constant coefficients determined in equation (6.11).

The electric field at point s due to charges on conductor k and its image conductors can be calculated by

$$E_{kp\_s} = \left(\frac{Q_k}{2\pi\varepsilon_0}\right)\frac{1}{\sqrt{(x_k-x_s)^2+(y_k-y_s)^2}} \tag{6.13}$$

$$E_{kn\_s} = -\left(\frac{Q_k}{2\pi\varepsilon_0}\right)\frac{1}{\sqrt{(x_k-x_s)^2+(y_k+y_s)^2}} \tag{6.14}$$

where Q_k is the charges on conductor *k.*

The relationships between the transmission line voltage and electric field amplitude at position s generated by each conductor and the imagine conductor can be derived by submitting equation (6.12) into equation (6.13) and (6.14)

$$E_{ap\_s} = \left(\frac{K_a(V_{ar}+V_{ai}i\,)}{2\pi\varepsilon_0}\right)\frac{1}{\sqrt{(x_a-x_s)^2+(y_a-y_s)^2}} \tag{6.14}$$

$$E_{an\_s} = -\left(\frac{K_a(V_{ar}+V_{ai}i\,)}{2\pi\varepsilon_0}\right)\frac{1}{\sqrt{(x_a-x_s)^2+(y_a+y_s)^2}}$$

$$E_{bp\_s} = \left(\frac{K_b(V_{ar}+V_{ai}i\,)}{2\pi\varepsilon_0}\right)\frac{1}{\sqrt{(x_b-x_s)^2+(y_b-y_s)^2}}$$

$$E_{bn\_s} = -\left(\frac{K_b(V_{ar}+V_{ai}i\,)}{2\pi\varepsilon_0}\right)\frac{1}{\sqrt{(x_b-x_s)^2+(y_b+y_s)^2}}$$

$$E_{cp\_s} = \left(\frac{K_c(V_{ar}+V_{ai}i\,)}{2\pi\varepsilon_0}\right)\frac{1}{\sqrt{(x_c-x_s)^2+(y_c-y_s)^2}}$$

$$E_{cn\_s} = -\left(\frac{K_c(V_{ar}+V_{ai}i\,)}{2\pi\varepsilon_0}\right)\frac{1}{\sqrt{(x_c-x_s)^2+(y_c+y_s)^2}}$$

The angles of the electric field at position s generated by conductor k are calculated by

$$\theta_{k\_s} = atan\frac{y_k-y_s}{x_k-x_s} \tag{6.15}$$

Thus, equation (6.14) can be expressed in a simplified format as:

$$E_{ap\_s} = L_1(V_{ar} + V_{ai}i\,) \tag{6.16}$$

$$E_{an\_s} = L_2(V_{ar} + V_{ai}i\,)$$

$$E_{bp_s} = L_3(V_{ar} + V_{ai}i\,)$$

$$E_{bn\_s} = L_4(V_{ar} + V_{ai}i\,)$$

$$E_{cp_s} = L_5(V_{ar} + V_{ai}i\,)$$

$$E_{cn\_s} = L_6(V_{ar} + V_{ai}i\,)$$

where L_1, L_2, L_3, L_4, L_5 and L_6 are the constant coefficients determined in equation (6.14)

For any electric field generated by one conductor and its image conductor can be expressed by real and imaginary parts. The electric field at the s point is the superposition of electric fields generated by one conductor and its image conductor,

$$\widetilde{E_{kp\_s}} = \widetilde{E_{kpx\_s}} + \widetilde{E_{kpy\_s}}\,i \tag{6.17}$$

$$\widetilde{E_{kn\_s}} = \widetilde{E_{knx\_s}} + \widetilde{E_{kny\_s}}\,i$$

$$\widetilde{E_{k\_s}} = \widetilde{E_{kpx\_s}} + \widetilde{E_{knx\_s}} + (\widetilde{E_{kpy_s}} + \widetilde{E_{kny_s}}\,)\,i$$

Then, equation (6.16) can be represented as

$$\widetilde{E_{ap\_s}} = \widetilde{E_{apx\_s}} + \widetilde{E_{apy\_s}}i = L_1(V_{ar} + V_{ai}i\,) \times cos\,(\theta_{a\_s}) + L_1(V_{ar} + V_{ai}i\,) \times sin\,(\theta_{a'\_s})i \tag{6.18}$$

$$\widetilde{E_{an\_s}} = \widetilde{E_{anx\_s}} + \widetilde{E_{any\_s}}i = L_2(V_{ar} + V_{ai}i\,) \times cos\,(\theta_{a'\_s}) + L_2(V_{ar} + V_{ai}i\,) \times sin\,(\theta_{a'\_s})i$$

$$\widetilde{E_{bp\_s}} = \widetilde{E_{bpx\_s}} + \widetilde{E_{bpy\_s}}i = L_3(V_{ar} + V_{ai}i\,) \times cos\,(\theta_{b\_s}) + L_3(V_{ar} + V_{ai}i\,) \times sin\,(\theta_{b'\_s})i$$

$$\widetilde{E_{bn\_s}} = \widetilde{E_{bnx\_s}} + \widetilde{E_{bny\_s}}i = L_4(V_{ar} + V_{ai}i\,) \times cos\,(\theta_{b'\_s}) + L_4(V_{ar} + V_{ai}i\,) \times sin\,(\theta_{b'\_s})i$$

$$\widetilde{E_{cp\_s}} = \widetilde{E_{cpx\_s}} + \widetilde{E_{cpy\_s}}i = L_5(V_{ar} + V_{ai}i\,) \times cos\,(\theta_{c\_s}) + L_5(V_{ar} + V_{ai}i\,) \times sin\,(\theta_{c'\_s})i$$

$$\widetilde{E_{cn\_s}} = \widetilde{E_{cnx\_s}} + \widetilde{E_{cny\_s}}i = L_6(V_{ar} + V_{ai}i\,) \times cos\,(\theta_{c'\_s}) + L_6(V_{ar} + V_{ai}i\,) \times sin\,(\theta_{c'\_s})i$$

And total electric field at the point s generated by the transmission line can be calculated by

$$E_{x\_s} = \left(L_1 \times cos\left(\theta_{a\_s}\right) + L_2 \times cos\left(\theta_{b\_s}\right) + L_3 \times cos\left(\theta_{c\_s}\right) + L_4 \times cos\left(\theta_{a'\_s}\right) + L_5 \times cos\left(\theta_{b'\_s}\right) + L_6 \times cos\left(\theta_{c'\_s}\right)\right) \times (V_{ar} + V_{ai}i\,) \quad (6.19)$$

$$E_{y\_s} = \left(L_1 \times sin\left(\theta_{a\_s}\right) + L_2 \times sin\left(\theta_{b\_s}\right) + L_3 \times sin\left(\theta_{c\_s}\right) + L_4 \times sin\left(\theta_{a'\_s}\right) + L_5 \times sin\left(\theta_{b'\_s}\right) + L_6 \times sin\left(\theta_{c'\_s}\right)\right) \times (V_{ar} + V_{ai}i\,)$$

For a simplification purpose, equation (6.19) can be represented as

$$E_{x\_s} = M_1 \times (V_{ar} + V_{ai}i\,) \quad (6.20)$$

$$E_{y\_s} = M_2 \times (V_{ar} + V_{ai}i\,)$$

where M_1 and M_2 are determined in equation (6.19).

The total electric field strength at the point s generated by the transmission line can be calculated by

$$|E_{total}| = \sqrt{(\left|E_{x\_s}\right|)^2 + (\left|E_{y\_s}\right|)^2} = \sqrt{(|M_1 \times (V_{ar} + V_{ai}i\,)\,|)^2 + (|M_2 \times (V_{ar} + V_{ai}i\,)\,|)^2} \quad (6.21)$$

Where $|E_{total}|$ is known as electric field strength measured at position s.

Since M_1 and M_2 are constant coefficients, equation (6.21) can be transformed as

$$|E_{total}|^2 = \left({M_1}^2 + {M_2}^2\right) \times |(V_{ar} + V_{ai}i\,)\,|^2 \quad (6.22)$$

Based on the physical meaning of the element, measured electric field strength and voltage amplitude are positive. The relationship between transmission line voltage amplitude and measured electric field strength at position s can be derived as follows:

$$|(V_{ar} + V_{ai}i\,)\,| = |V_{ln}| = \frac{|E_{total}|}{\sqrt{({M_1}^2 + {M_2}^2)}} \quad (6.23)$$

6.2.2 Double circuit transmission line

Similar to the single circuit transmission line, a traditional infinite and balanced model of a three-phase double circuit transmission line is used for electric field calculation and presented in Fig. 6.3. The same assumptions and simplification about conductor coordinates, GMR, and ground effect are used in this section.

As shown in Fig. 6.3, the bundled conductors of the transmission line are converted into equivalent conductors. An electric field sensor is placed at location s and the coordination is defined as x_s and y_s. Since the sensor is placed on the ground, y_s is set to 0. The electric field strength measured by the sensor is E_m. It is assumed that the voltage of the transmission line is balance and line to ground voltage of the conductors are defined as:

$$\boldsymbol{V_{a1p}} = V_{1lg}\angle 0^o \tag{6.24}$$

$$\boldsymbol{V_{b1p}} = V_{1lg}\angle 120^o$$

$$\boldsymbol{V_{c1p}} = V_{1lg}\angle 240^o$$

where V_{1lg} is the line to ground voltage at circuit 1.

$$\boldsymbol{V_{a2p}} = V_{2lg}\angle 0^o \tag{6.25}$$

$$\boldsymbol{V_{b2p}} = V_{2lg}\angle 120^o$$

$$\boldsymbol{V_{c2p}} = V_{2lg}\angle 240^o$$

where V_{2l} is the line to ground voltage at circuit 2.

Equation (6.24) and (6.25) can be converted into complex format:

$$\boldsymbol{V_{a1p}} = V_{a1r} + V_{a1i}i \tag{6.26}$$

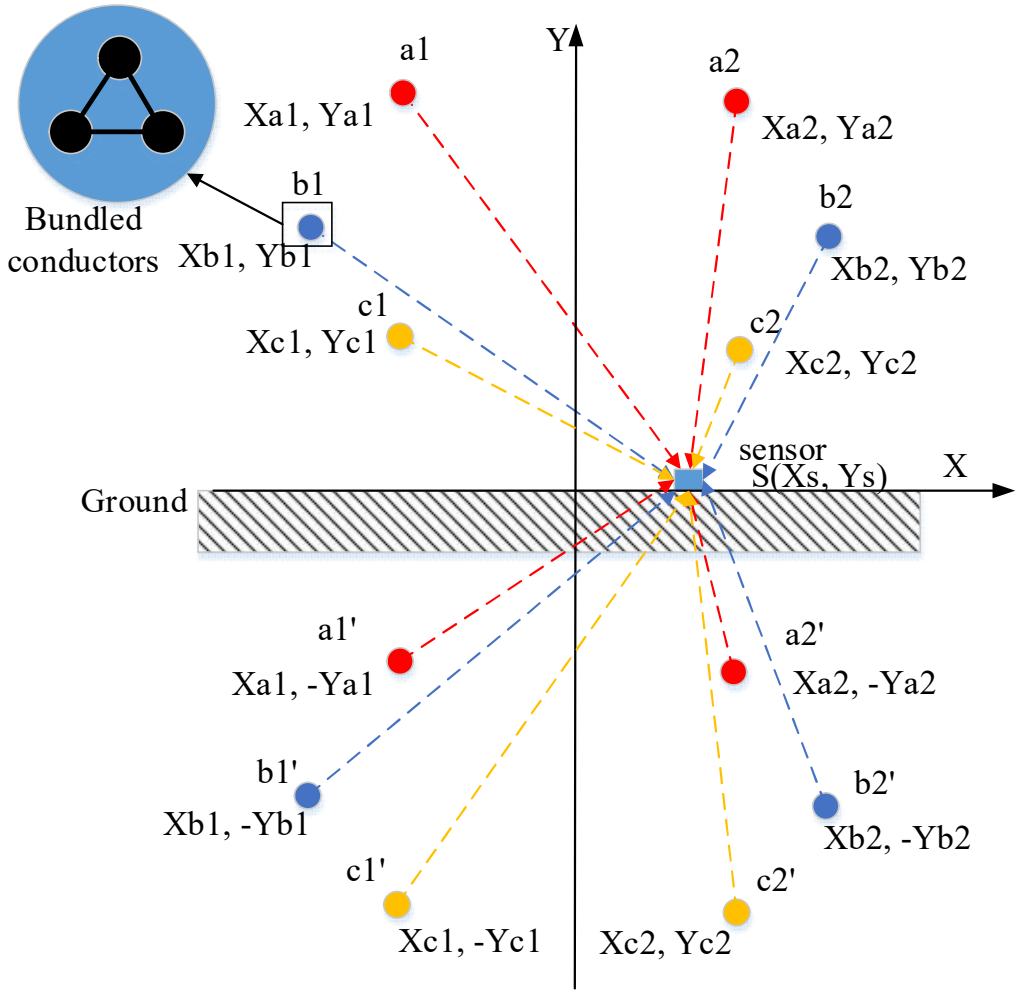

Figure 6.3. Double circuit transmission line configuration and sensor position

$$\boldsymbol{V_{b1p}} = (V_{a1r} + V_{a1i}i\ ) \times (-0.5 + 0.866i)$$

$$\boldsymbol{V_{c1p}} = (V_{a1r} + V_{a1i}i\ ) \times (-0.5 - 0.866i)$$

where V_{a1r} and V_{a1i} are the real and imaginary parts of circuit 1 voltage in phase a respectively and two unknown variables to be determined below.

$$\boldsymbol{V_{a2p}} = V_{a2r} + V_{a2i}i \tag{6.27}$$

$$\boldsymbol{V_{b2p}} = (V_{a2r} + V_{a2i}i) \times (-0.5 + 0.866i)$$

$$\boldsymbol{V_{c2p}} = (V_{a2r} + V_{a2i}i) \times (-0.5 - 0.866i)$$

where V_{a2r} and V_{a2i} are the real and imaginary parts of circuit 2 voltage in phase a respectively and two unknown variables to be determined below.

As discussed in the aforementioned section, for the double circuit transmission line shown in Fig. 6.3, the distant from conductor *k* to the actual conductors and image conductors can be determined in 6×6 matrices as

$$\boldsymbol{d} = \begin{bmatrix} r_{1\text{bund}} & \cdots & \sqrt{(x_{a1} - x_{c2})^2 + (y_{a1} - y_{c2})^2} \\ \vdots & \ddots & \vdots \\ \sqrt{(x_{c2} - x_{a1})^2 + (y_{c2} - y_{a1})^2} & \cdots & r_{2\text{bund}} \end{bmatrix} \tag{6.28}$$

$$\boldsymbol{D} = \begin{bmatrix} 2y_{\text{a}} & \cdots & \sqrt{(x_{a1} - x_{c2})^2 + (y_{a1} + y_{c2})^2} \\ \vdots & \ddots & \vdots \\ \sqrt{(x_{c2} - x_{a1})^2 + (y_{c2} + y_{a1})^2} & \cdots & 2y_{\text{a}} \end{bmatrix} \tag{6.29}$$

Similarly, potential coefficients $\boldsymbol{P}$ can be determined by submitting equation (6.28) and (6.29) into equation (6.5) and inversion of $\boldsymbol{P}$ is expressed

$$\boldsymbol{P^{-1}} = \begin{bmatrix} p^{-1}{}_{11} & \cdots & p^{-1}{}_{16} \\ \vdots & \ddots & \vdots \\ p^{-1}{}_{61} & \cdots & p^{-1}{}_{66} \end{bmatrix} \tag{6.30}$$

The relationship between charges on the conductors and voltages can be built:

$$Q_{a1} = V_{a1p} \times {p^{-1}}_{11} + V_{a1p} \times (-0.5 + 0.866i) \times {p^{-1}}_{12} + V_{a1p} \times (-0.5 - 0.866i) \times {p^{-1}}_{13} + V_{a2p} \times {p^{-1}}_{14} + V_{a2p} \times (-0.5 + 0.866i) \times {p^{-1}}_{15} + V_{a2p} \times (-0.5 - 0.866i) \times {p^{-1}}_{16} \quad (6.31)$$

$$Q_{b1} = V_{a1p} \times {p^{-1}}_{21} + V_{a1p} \times (-0.5 + 0.866i) \times {p^{-1}}_{22} + V_{a1p} \times (-0.5 - 0.866i) \times {p^{-1}}_{23} + V_{a2p} \times {p^{-1}}_{24} + V_{a2p} \times (-0.5 + 0.866i) \times {p^{-1}}_{25} + V_{a2p} \times (-0.5 - 0.866i) \times {p^{-1}}_{26}$$

$$Q_{c1} = V_{a1p} \times {p^{-1}}_{31} + V_{a1p} \times (-0.5 + 0.866i) \times {p^{-1}}_{32} + V_{a1p} \times (-0.5 - 0.866i) \times {p^{-1}}_{33} + V_{a2p} \times {p^{-1}}_{34} + V_{a2p} \times (-0.5 + 0.866i) \times {p^{-1}}_{35} + V_{a2p} \times (-0.5 - 0.866i) \times {p^{-1}}_{36}$$

$$Q_{a2} = V_{a1p} \times {p^{-1}}_{41} + V_{a1p} \times (-0.5 + 0.866i) \times {p^{-1}}_{42} + V_{a1p} \times (-0.5 - 0.866i) \times {p^{-1}}_{43} + V_{a2p} \times {p^{-1}}_{44} + V_{a2p} \times (-0.5 + 0.866i) \times {p^{-1}}_{45} + V_{a2p} \times (-0.5 - 0.866i) \times {p^{-1}}_{46}$$

$$Q_{b2} = V_{a1p} \times {p^{-1}}_{51} + V_{a1p} \times (-0.5 + 0.866i) \times {p^{-1}}_{52} + V_{a1p} \times (-0.5 - 0.866i) \times {p^{-1}}_{53} + V_{a2p} \times {p^{-1}}_{54} + V_{a2p} \times (-0.5 + 0.866i) \times {p^{-1}}_{55} + V_{a2p} \times (-0.5 - 0.866i) \times {p^{-1}}_{56}$$

$$Q_{c2} = V_{a1p} \times {p^{-1}}_{61} + V_{a1p} \times (-0.5 + 0.866i) \times {p^{-1}}_{62} + V_{a1p} \times (-0.5 - 0.866i) \times {p^{-1}}_{63} + V_{a2p} \times {p^{-1}}_{64} + V_{a2p} \times (-0.5 + 0.866i) \times {p^{-1}}_{65} + V_{a2p} \times (-0.5 - 0.866i) \times {p^{-1}}_{66}$$

For a simplification purpose, equations (6.31) can be expressed as

$$Q_{a1} = K_{a11} \times V_{a1p} + K_{a21} \times V_{a2p} \quad (6.32)$$

$$Q_{b1} = K_{b11} \times V_{a1p} + K_{b21} \times V_{a2p}$$

$$Q_{c1} = K_{c11} \times V_{a1p} + K_{c21} \times V_{a2p}$$

$$Q_{a2} = K_{a12} \times V_{a1p} + K_{a22} \times V_{a2p}$$

$$Q_{b2} = K_{b12} \times V_{a1p} + K_{b22} \times V_{a2p}$$

$$Q_{c2} = K_{c12} \times V_{a1p} + K_{c2} \times V_{a2p}$$

where the constant coefficients K are known constants determined in equation (6.31).

The electric field at point s due to charges on conductor k and its image conductors can be calculated by submitting equation (6.32) into equation (6.13) and (6.14). The relationships between the transmission line voltage and electric field amplitude generated by each conductor and its imagine conductor can be derived:

$$E_{a1p\_s} = \left(\frac{K_{a1} \times V_{a1p} + K_{a2} \times V_{a2p}}{2\pi\varepsilon_0}\right) \frac{1}{\sqrt{(x_{a1} - x_s)^2 + (y_{a1} - y_s)^2}} \tag{6.33}$$

$$E_{a1n\_s} = -\left(\frac{K_{a11} \times V_{a1p} + K_{a21} \times V_{a2p}}{2\pi\varepsilon_0}\right) \frac{1}{\sqrt{(x_{a1} - x_s)^2 + (y_{a1} + y_s)^2}}$$

$$E_{b1p\_s} = \left(\frac{K_{b1} \times V_{a1p} + K_{b2} \times V_{a2p}}{2\pi\varepsilon_0}\right) \frac{1}{\sqrt{(x_{b1} - x_s)^2 + (y_{b1} - y_s)^2}}$$

$$E_{b1n\_s} = -\left(\frac{K_{b1} \times V_{a1p} + K_{b21} \times V_{a2p}}{2\pi\varepsilon_0}\right) \frac{1}{\sqrt{(x_{b1} - x_s)^2 + (y_{b1} + y_s)^2}}$$

$$E_{c1p\_s} = \left(\frac{K_{a1} \times V_{a1p} + K_{a22} \times V_{a2p}}{2\pi\varepsilon_0}\right) \frac{1}{\sqrt{(x_{c1} - x_s)^2 + (y_{c1} - y_s)^2}}$$

$$E_{c1n\_s} = -\left(\frac{K_{a12} \times V_{a1p} + K_{a22} \times V_{a2p}}{2\pi\varepsilon_0}\right) \frac{1}{\sqrt{(x_{c1} - x_s)^2 + (y_{c1} + y_s)^2}}$$

$$E_{a2p\_s} = \left(\frac{K_{a12} \times V_{a1p} + K_{a22} \times V_{a2p}}{2\pi\varepsilon_0}\right) \frac{1}{\sqrt{(x_{a2} - x_s)^2 + (y_{a2} - y_s)^2}}$$

$$E_{a2n\_s} = -\left(\frac{K_{a1} \times V_{a1p} + K_{a22} \times V_{a2p}}{2\pi\varepsilon_0}\right) \frac{1}{\sqrt{(x_{a2} - x_s)^2 + (y_{a2} + y_s)^2}}$$

$$E_{b2p\_s} = \left(\frac{K_{b12} \times V_{a1p} + K_{b22} \times V_{a2p}}{2\pi\varepsilon_0}\right) \frac{1}{\sqrt{(x_{b2} - x_s)^2 + (y_{b2} - y_s)^2}}$$

$$E_{b2n\_s} = -\left(\frac{K_{b12} \times V_{a1p} + K_{b22} \times V_{a2p}}{2\pi\varepsilon_0}\right) \frac{1}{\sqrt{(x_{b2} - x_s)^2 + (y_{b2} + y_s)^2}}$$

$$E_{c2p\_s} = \left(\frac{K_{c12}\times V_{a1p}+K_{c22}\times V_{a2p}}{2\pi\varepsilon_0}\right)\frac{1}{\sqrt{(x_{c2}-x_s)^2+(y_{c2}-y_s)^2}}$$

$$E_{c2n\_s} = -\left(\frac{K_{c12}\times V_{a1p}+K_{c22}\times V_{a2p}}{2\pi\varepsilon_0}\right)\frac{1}{\sqrt{(x_{c2}-x_s)^2+(y_{c2}+y_s)^2}}$$

where the constant coefficients K are known constants determined in equation (6.31).

The angles of the electric field at position s generated by conductor k are calculated by equation (6.15).

Equation (6.33) can be represented for a simplification purpose:

$$E_{a1p\_s} = L_{a11p}\times V_{a1p} + L_{a21p}\times V_{a2p} \tag{6.34}$$

$$E_{a1n\_s} = -L_{a11n}\times V_{a1p} - L_{a21n}\times V_{a2p}$$

$$E_{b1p\_s} = L_{b11p}\times V_{a1p} + L_{b21p}\times V_{a2p}$$

$$E_{b1n\_s} = -L_{b11n}\times V_{a1p} - L_{b21n}\times V_{a2p}$$

$$E_{c1p\_s} = L_{c11p}\times V_{a1p} + L_{c21p}\times V_{a2p}$$

$$E_{c1n\_s} = -L_{c11n}\times V_{a1p} - L_{c21n}\times V_{a2p}$$

$$E_{a2p\_s} = L_{a12p}\times V_{a1p} + L_{a22}\ \times V_{a2p}$$

$$E_{a2n\_s} = -L_{a12n}\times V_{a1p} - L_{a22n}\times V_{a2p}$$

$$E_{b2p\_s} = L_{b12p}\times V_{a1p} + L_{b22p}\times V_{a2p}$$

$$E_{b2n\_s} = -L_{b12n}\times V_{a1p} - L_{b22n}\times V_{a2p}$$

$$E_{c2p\_s} = L_{c12p}\times V_{a1p} + L_{c22p}\times V_{a2p}$$

$$E_{c2n\_s} = -L_{c12n}\times V_{a1p} - L_{c22n}\times V_{a2p}$$

where the constant coefficients L are known constants determined in equation (6.33).

The electric field generated by each conductor and its image conductor at the s point is calculated by submitting equation (6.34) into equation (6.17):

$$\widetilde{E_{a1p\_s}} = E_{a1px\_s} + E_{a1py\_s}i = (L_{a11p} \times V_{a1p} + L_{a21p} \times V_{a2p}) \times cos\,(\theta_{a1\_s}) + (L_{a11p} \times V_{a1p} + L_{a21p} \times V_{a2p}) \times sin\,(\theta_{a1\_s})i \quad (6.34)$$

$$\widetilde{E_{a1n\_s}} = E_{a1nx\_s} + E_{a1ny\_s}i = (L_{a11p}(L_{a11p} \times V_{a1p} + L_{a21p} \times V_{a2p}) \times cos\,(\theta_{a1'\_s}) + (L_{a11p} \times V_{a1p} + L_{a21p} \times V_{a2p}) \times sin\,(\theta_{a1'\_s})i$$

$$\widetilde{E_{b1p\_s}} = E_{b1px\_s} + E_{b1py\_s}i = (L_{b11p} \times V_{a1p} + L_{b21p} \times V_{a2p}) \times cos\,(\theta_{b1\_s}) + (L_{b11p} \times V_{a1p} + L_{b21p} \times V_{a2p}) \times sin\,(\theta_{b1\_s})i$$

$$\widetilde{E_{b1n\_s}} = E_{b1nx\_s} + E_{b1ny\_s}i = (L_{b11p} \times V_{a1p} + L_{b21p} \times V_{a2p}) \times cos\,(\theta_{b1'\_s}) + (L_{b11p} \times V_{a1p} + L_{b21p} \times V_{a2p}) \times sin\,(\theta_{b1'\_s})i$$

$$\widetilde{E_{c1p\_s}} = E_{c1px\_s} + E_{c1py\_s}i = (L_{c11p} \times V_{a1p} + L_{c21p} \times V_{a2p}) \times cos\,(\theta_{c1\_s}) + (L_{c11p} \times V_{a1p} + L_{c21p} \times V_{a2p}) \times sin\,(\theta_{c1\_s})i$$

$$\widetilde{E_{c1n\_s}} = E_{c1nx\_s} + E_{c1ny\_s}i = (L_{c11p} \times V_{a1p} + L_{c21p} \times V_{a2p}) \times cos\,(\theta_{c1'\_s}) + (L_{c11p} \times V_{a1p} + L_{c21p} \times V_{a2p}) \times sin\,(\theta_{c1'\_s})i$$

$$\widetilde{E_{a2p\_s}} = E_{a2px\_s} + E_{a2py\_s}i = (L_{a12p} \times V_{a1p} + L_{a22p} \times V_{a2p}) \times cos\,(\theta_{a2\_s}) + (L_{a12p} \times V_{a1p} + L_{a22p} \times V_{a2p}) \times sin\,(\theta_{a2\_s})i$$

$$\widetilde{E_{a2n\_s}} = E_{a2nx\_s} + E_{a2ny\_s}i = (L_{a12p} \times V_{a1p} + L_{a22p} \times V_{a2p}) \times cos\,(\theta_{a2'\_s}) + (L_{a12p} \times V_{a1p} + L_{a22p} \times V_{a2p}) \times sin\,(\theta_{a2'\_s})i$$

$$\widetilde{E_{b2p\_s}} = E_{b2px\_s} + E_{b2py\_s}i = (L_{b12p} \times V_{a1p} + L_{b22p} \times V_{a2p}) \times cos\,(\theta_{b2\_s}) + (L_{b12p} \times V_{a1p} + L_{b22p} \times V_{a2p}) \times sin\,(\theta_{b2\_s})i$$

$$\widetilde{E_{b2n\_s}} = E_{b2nx\_s} + E_{b2ny\_s}i = (L_{b12p} \times V_{a1p} + L_{b22p} \times V_{a2p}) \times cos\,(\theta_{b2\prime\_s}) +$$

$$(L_{b12p} \times V_{a1p} + L_{b22p} \times V_{a2p}) \times sin\,(\theta_{b2\prime\_s})i$$

$$\widetilde{E_{c2p\_s}} = E_{c2px\_s} + E_{c2py\_s}i = (L_{c12p} \times V_{a1p} + L_{c22p} \times V_{a2p}) \times cos\,(\theta_{c2\_s}) +$$

$$(L_{c12p} \times V_{a1p} + \ L_{c22p} \times V_{a2p}) \times sin\,(\theta_{c2\_s})i$$

$$\widetilde{E_{c2n\_s}} = E_{c2nx\_s} + E_{c2ny\_s}i = (L_{c12p} \times V_{a1p} + L_{c22p} \times V_{a2p}) \times cos\,(\theta_{c2\prime\_s}) +$$

$$(L_{c12p} \times V_{a1p} + L_{c22p} \times V_{a2p}) \times sin\,(\theta_{c2\prime\_s})i$$

where θ_{k_s} and $\theta_{k\prime\_s}$ are calculated by equation (6.15).

Then, the total electric field in the X and Y axis at the s point can be expressed by using superposition method

$$E_{x\_s} = E_{a1px\_s} + E_{a1nx\_s} + E_{b1px_s} + E_{b1nx\_s} + E_{c1px\_s} + E_{c1nx\_s} + E_{a2px\_s} + E_{a2nx\_s} +$$

$$E_{b2px\_s} + E_{b2nx\_s} + E_{c2px\_s} + E_{c2nx\_s} \tag{6.35}$$

$$E_{y\_s} = E_{a1py\_s} + E_{a1ny\_s} + E_{b1py} + E_{b1ny\_s} + E_{c1py\_s} + E_{c1ny\_s} + E_{a2py\_s} + E_{a2ny\_s} +$$

$$E_{b2py\_s} + E_{b2ny\_s} + E_{c2py\_s} + E_{c2ny\_s}$$

Equation (6.35) can be simplified as

$$E_{x\_s} = M_{1x} \times V_{a1p} + M_{2x} \times V_{a2p} \tag{6.36}$$

$$E_{y\_s} = M_{1y} \times V_{a1p} + M_{2y} \times V_{a2p}$$

where M_{1x}, M_{2x}, M_{1y} and M_{2y} are constant coefficients determined in equation (6.34) and (6.35).

The total electric field strength $|E_{total}|$ at the point s generated by the transmission line can be calculated by

$$|E_{total}| = \sqrt{(|M_{1x} \times V_{a1p} + M_{2x} \times V_{a2p}|)^2 + (|M_{1y} \times V_{a1p} + M_{2y} \times V_{a2p}|)^2} \quad (6.37)$$

Since M_{1x}, M_{2x}, M_{1y} and M_{2y} are the constants vector determined in equation (6.34) and V_{a1p}, V_{a2p} are unknown scalar, the equation (6-37) can be expanded as:

$$|E_{total}|^2 = (|M_{1x}|^2 \times {V_{a1p}}^2 + |M_{2x}|^2 \times {V_{a2p}}^2 + 2 \times |M_{1x}| \times |M_{2x}| \times V_{a1p} \times V_{a2p} \times \cos(\theta_{m1x\_m2x})) + (|M_{1y}|^2 \times {V_{a1p}}^2 + |M_{2y}|^2 \times {V_{a2p}}^2 + 2 \times |M_{1y}| \times |M_{2y}| \times V_{a1p} \times V_{a2p} \times \cos(\theta_{m1y\_m2y})) \quad (6.37)$$

where θ_{m1x_m2x} is the angle between the known vector M_{1x} and M_{2x}, θ_{m1y_m2y} is the angle between the known vector M_{1y} and M_{2y}.

Thus, the equation can be simplified as:

$$|E_{total}|^2 = C_1 \times {V_{a1p}}^2 + D_1 \times {V_{a2p}}^2 + F_1 \times V_{a1p} \times V_{a2p} \quad (6.38)$$

where C_1, D_1 and F_1 are the known constants determined in (3-37).

To determine V_{a1p} and V_{a2p}, two sensors are placed in different locations under the transmission line and the following equation set can be established and voltages of the transmission line can be determined by solving the equation set with Matlab.

$$\begin{cases} |E_1|^2 = C_1 \times {V_{a1p}}^2 + D_2 \times {V_{a2p}}^2 + F_3 \times V_{a1p} \times V_{a2p} \\ |E_2|^2 = C_2 \times {V_{a1p}}^2 + D_2 \times {V_{a2p}}^2 + F_3 \times V_{a1p} \times V_{a2p} \end{cases} \quad (6.39)$$

6.3 Simulation validation

To validate the effectiveness and performance of the proposed method, the derived equations are implemented in Matlab code. A 525 kV single circuit transmission line and a 525 kV double circuit transmission line configurations from [133] are utilized to test the method. The electric

field strength generated by the transmission line on the ground level are duplicated by Matlab code based on the methods from [133] and used as measured electric field strength in the proposed method. The simulation tests are conducted on a computer running a 64-bit Windows 10, with a 3.60 GHz Intel I7-7700U CPU and 16 GB memory.

(1). Three-phase single circuit transmission line

A 525 kV three-phase single circuit transmission line with a flat configuration from [133] is selected as a test case. The information of the configuration, including conductor size, bundle size, actual conductor size and conductor coordinates, are summarized in Table 6.1. The lateral profiles of the electric field at ground provided in [133] is shown in Fig. 6.3. The electric field strength profiles duplicate by Matlab code with the specified configuration is plotted in Fig. 6.4. The duplicated electric field profile is used as the input measurement of the proposed method.

The conductors in the configuration are converted into equivalent conductors with Matlab code and used in the proposed method testing. A sensor placed at different locations beneath the transmission line in two scenarios and the corresponding electric field strength at the locations is selected from Fig. 6.5 as measured input. The sensor locations, the measured electric field strength and the calculated voltage are summarized in Table 6.2. As shown in the table, the sensor locations are one meter away in two scenarios, which caused the measured electric field strength is slightly different. The calculated voltages in both scenarios of the proposed method are identical to the line voltage specified in the configuration.

(2). Three-phase double circuit transmission line

A 525 kV three-phase double circuit transmission line configuration from [133] is selected as a test case. The information of the configuration, including conductor size, bundle size, actual

Table 6.1. Flat configuration of 525 kV single circuit transmission line

	Conductor1	Conductor2	Conductor3
X axis (m)	10	0	-10
Y axis (m)	10.6	10.6	10.6
Bundle Num.	3	3	3
Bundle spacing (m)	0.45	0.45	0.45
conductor diameter (m)	0.033	0.033	0.033
Line to ground voltage (kV)	303	303	303
Voltage angle (degree)	120	0	240

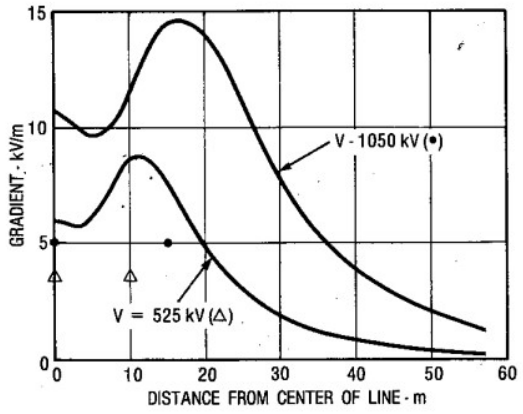

Figure 8.3.3. Lateral profiles of electric field at ground. (a) Line at 525 kV with 3 × 3.3-cm conductor, 45-cm spacing, spaced 10 m, and 10.6 m above ground, flat configuration. (b) Line at 1050 kV with 8 × 3.3-cm conductors on 101-cm diameter, spaced 18.3 m, and 18.3 m above ground, flat configuration.

Figure 6.4. Single circuit transmission line electric field distribution at ground [133]

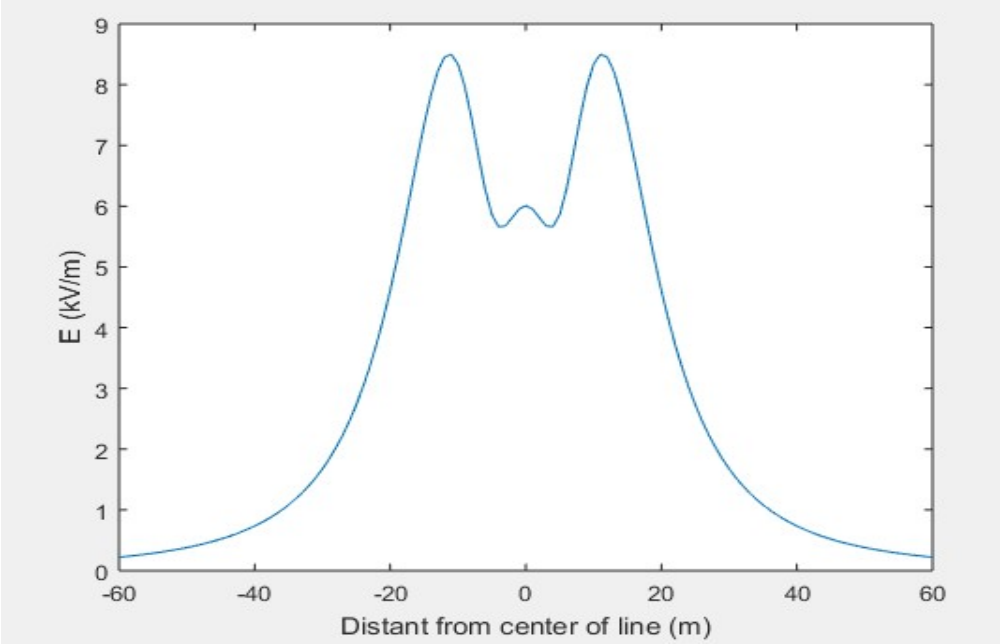

Figure 6.5. Single circuit transmission line electric field distribution at ground generated by Matlab code

Table 6.2. Testing conditions and results of 525 kV single circuit transmission line

	X axis (m)	Y axis (m)	Measured EF strength (kV/m)	Calculated voltage (kV)
Scenario 1	0	1	6.009317907	303
Scenario 2	1	1	5.951386844	303

conductor size and conductor coordinates, are summarized in Table 6.3 and Table 6.4. The lateral profiles of the electric field at ground provided in [133] are shown in Fig. 6.5. The electric field strength profiles duplicated by Matlab code with the specified configuration and #1 phase arrangement is plotted in Fig. 7.6. The duplicated electric field profile is used as the input measurement of the proposed method.

The conductors in the configuration are converted into equivalent conductors with Matlab and used in the proposed method testing. For the three-phase double circuit transmission line, two sensors are placed at different locations beneath the transmission line in two scenarios. The corresponding electric field strength at the locations in each scenario is selected from Fig. 6.7 as measured inputs. The sensor locations, the measured electric field strength and the calculated voltage are summarized in Table 6.5. As shown in the calculation results, the estimated transmission line voltages are slightly lower than the measured voltage in both scenarios. However, the maximum estimated error is 0.561%, which is considered very trivial. The estimated voltages differences in the two scenarios indicate that the locations of the sensor have impacts on the estimated results and symmetric placement of the sensors will lead to a more accurate result.

6.4 Conclusion

This chapter proposes a method to estimate three-phase transmission line voltage by using measured electric field strength for non-contact synchronized measurement. The theoretical foundation and the assumptions in the estimating process are discussed and presented. Linear relationships between measured electric field strength and transmission line voltage are derivated and established. A three-phase single circuit transmission line with flat configuration and a three-phase double circuit transmission line are used to demonstrate the derivation process.

Table 6.3. Circuit 1 configuration of 525 kV double circuit transmission line

	Conductor1	Conductor2	Conductor3
X axis (m)	5.56	8.61	5.56
Y axis (m)	13.72	23.78	33.4
Bundle Num.	3	3	3
Bundle spacing (m)	0.457	0.457	0.457
conductor diameter (m)	0.0325	0.0325	0.0325
Line to ground voltage (kV)	303	303	303
Voltage angle (degree)	240	120	0

Table 6.4. Circuit 2 configuration of 525 kV double circuit transmission line

	Conductor1	Conductor2	Conductor3
X axis (m)	-5.56	-8.61	-5.56
Y axis (m)	13.72	23.78	33.4
Bundle Num.	3	3	3
Bundle spacing (m)	0.457	0.457	0.457
conductor diameter (m)	0.0325	0.0325	0.0325
Line to ground voltage (kV)	303	303	303
Voltage angle (degree)	240	120	0

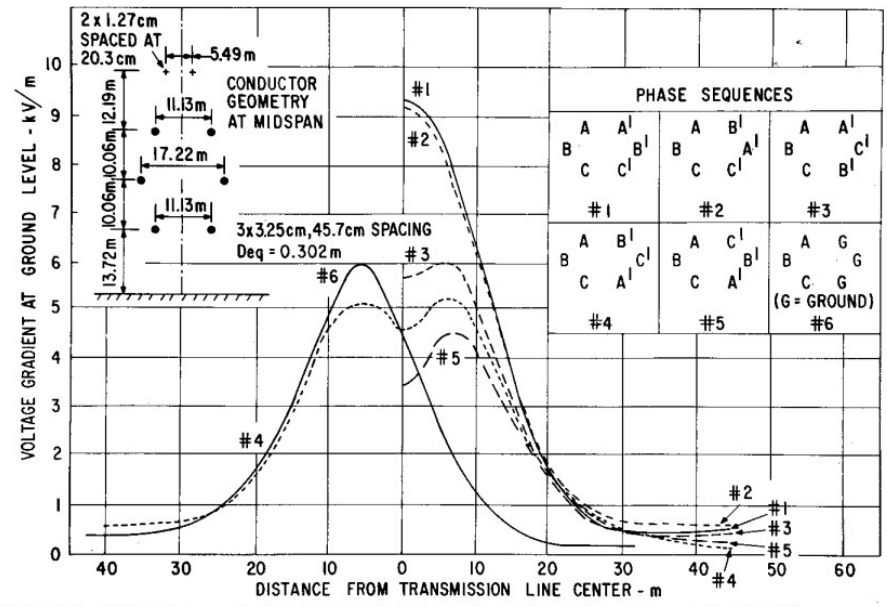

Figure 8.3.12. Electric field at ground level for a typical double-circuit geometry and different phase arrangements. V = 525 kV. Phase arrangement 1, superbundle, corresponds to the maximum ground gradient (and the minimum conductor gradient). Phase arrangement 5, low-reactance, corresponds to the minimum ground gradient (and the maximum conductor gradient and maximum power transfer capability).

Figure 6.6. Double circuit transmission line electric field distribution at ground [133]

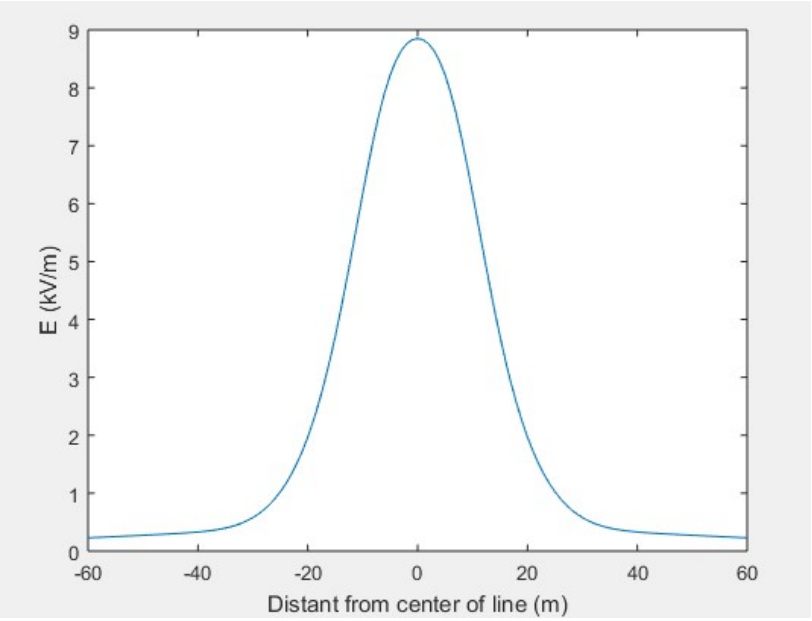

Figure 6.7. Double circuit transmission line electric field distribution at ground generated by Matlab code

Table 6.5. Testing conditions and results of 525 kV double circuit transmission line

	sensor	X axis (m)	Y axis (m)	Measured EF strength (kV/m)	Calculated voltage (kV)
Scenario 1	Sensor #1	0	1	8.708581562	V_{a1p}=302.4
	Sensor #2	1	1	8.731588219	V_{a2p}=301.3
Scenario 2	Sensor #1	1	1	8.708581562	V_{a1p}=301.9
	Sensor #2	-1	1	8.708581562	V_{a2p}=301.9

The proposed method is implemented in Matlab code for both three-phase single and double circuit transmission line. Simulation tests are conducted based on a three-phase 525 kV single circuit transmission line and a double circuit transmission line from [133]. The testing results show that the proposed method can precisely estimate the transmission line voltage. It also indicates that the symmetrical placement of the electric field strength sensor provides better performance. It can work as an effective method for real-time non-contact synchronized measurement.

List of References

[1] R. Sherick and R. Yinger, "Modernizing the Calfornia Grid : Preparing for a Future with High Penetrations of Distributed Energy Resources," in IEEE Power and Energy Magazine, vol. 15, no. 2, pp. 20-28, March-April 2017.

[2] F. Luo et al., "Cloud-Based Information Infrastructure for Next-Generation Power Grid: Conception, Architecture, and Applications," in IEEE Transactions on Smart Grid, vol. 7, no. 4, pp. 1896-1912, July 2016.

[3] M. Qiu, W. Gao, M. Chen, J. W. Niu and L. Zhang, "Energy Efficient Security Algorithm for Power Grid Wide Area Monitoring System," in IEEE Transactions on Smart Grid, vol. 2, no. 4, pp. 715-723, Dec. 2011.

[4] "Integrating Wind Power into the Electric Grid-Prospectives for Policymakers", National Conference of State Legislature. [Online].Available: http://www.uwig.org/ncsl-wind_integration.pdf

[5] K.A. Folly, "Wind Energy Integration into the South African Grid: Prospects and Challenges", Wind Energy-developments, Potential and Challenges, pp.93-120, Nova Publisher, New York, 2016.

[6] B. K. Bose, "Artificial Intelligence Techniques in Smart Grid and Renewable Energy Systems—Some Example Applications," in Proceedings of the IEEE, vol. 105, no. 11, pp. 2262-2273, Nov. 2017.

[7] T. Weissbach and E. Welfonder, "High frequency deviations within the European Power System: Origins and proposals for improvement," 2009 IEEE/PES Power Systems Conference and Exposition, Seattle, WA, 2009, pp. 1-6

[8] M. D. Hadley, J. B. McBride, T. W. Edgar, L. R. O'Neil, and J. D. Johnson. (Jun. 2007). Securing Wide Area Measurement Systems. [Online]. Available: http://energy.gov/oe/downloads/ securing-wide-area-measurement-systems

[9] Y. Liu et al., "Recent developments of FNET/GridEye — A situational awareness tool for smart grid," in CSEE Journal of Power and Energy Systems, vol. 2, no. 3, pp. 19-27, Sept. 2016.

[10] A. G. Phadke, H. Volskis, R. M. de Moraes, T. S. Bi, R. N. Nayak,Y. K. Sehgal, S. Sen, W. Sattinger, E. Martinez, O. Samuelsson, D.Novosel, V. Madani, and Y. A. Kulikov, "The wide world of wide-area measurement," IEEE Power & Energy Magazine, vol. 6, no. 5, pp. 52–65, Sep. /Oct. 2008.

[11] M. Chenine, J. Ullberg, L. Nordström, Y. Wu and G. N. Ericsson, "A Framework for Wide-Area Monitoring and Control Systems Interoperability and Cybersecurity Analysis," in IEEE Transactions on Power Delivery, vol. 29, no. 2, pp. 633-641, April 2014.

[12] J. F. Hauer et al., "Use of the WECC WAMS in Wide-Area Probing Tests for Validation of System Performance and Modeling," in IEEE Transactions on Power Systems, vol. 24, no. 1, pp. 250-257, Feb. 2009.

[13] G. Zheng and R. Craven, "Multiclass support vector machines for power system disturbances classification based on wide-area frequency measurements," in 2011 Proceedings of IEEE Southeastcon, 2011, pp. 68-72.

[14] W. Gao and J. Ning, "Wavelet-Based Disturbance Analysis for Power System Wide-Area Monitoring," IEEE Transactions on Smart Grid, vol. 2, pp. 121-130, 2011.
[15] A. J. Allen, S. W. Sohn, S. Santoso, and W. M. Grady, "Algorithm for screening PMU data for power system events," in 2012 3rd IEEE PES Innovative Smart Grid Technologies Europe (ISGT Europe), 2012, pp. 1-6.
[16] X. Qin, B. Li, Q. Guo, S. Hong, Q. Zhou, and T. Bi, "Study on power system disturbance identification and location based on WAMS," in 2012 IEEE Power and Energy Society General Meeting, 2012, pp. 1-6.
[17] E. Barocio, B. C. Pal, D. Fabozzi, and N. F. Thornhill, "Detection and visualization of power system disturbances using principal component analysis," in 2013 IREP Symposium Bulk Power System Dynamics and Control - IX Optimization, Security and Control of the Emerging Power Grid, 2013, pp. 1-10.
[18] Y. Y. Ge, A. J. Flueck, D. K. Kim, J. B. Ahn, J. D. Lee, and D. Y. Kwon, "Power System Real-Time Event Detection and Associated Data Archival Reduction Based on Synchrophasors," IEEE Tran. Smart Grid, vol. 6, pp. 2088-2097, Jul 2015.
[19] M. Rafferty, X. Q. Liu, D. M. Laverty, and S. McLoone, "Real- Time Multiple Event Detection and Classification Using Moving Window PCA," IEEE Tran. Smart Grid, vol. 7, pp. 2537-2548, Sep 2016.
[20] T. Yin, S. S. Wulff, J. W. Pierre, D. Duan, D. J. Trudnowski, and M. Donnelly, "Initial investigation of data mining applications in event classification and location identification using simulated data from Minni WECC," 2016 North American Power Symposium (NAPS), 2016, pp. 1-6.
[21] X. Deng, D. Bian, D. Shi, W. Yao, L. Wu and Y. Liu, "Impact of Low Data Quality on Disturbance Triangulation Application Using High-Density PMU Measurements," in IEEE Access, vol. 7, pp. 105054-105061, 2019.
[22] D. Zhou, Y. Liu and J. Dong, "Frequency-based real-time line trip detection and alarm trigger development," IEEE PES General Meeting | Conference & Exposition, National Harbor, MD, 2014, pp. 1-5.
[23] T. Xia, H. Zhang, R. Gardner, J. Bank, J. Dong, J. Zuo, et al., "Wide-area Frequency Based Event Location Estimation," in 2007 IEEE Power Engineering Society General Meeting, 2007, pp. 1-7.
[24] W. Wang, L. He, P. Markham, H. Qi, Y. Liu, Q. C. Cao, et al., "Multiple Event Detection and Recognition Through Sparse Unmixing for High-Resolution Situational Awareness in Power Grid," IEEE Trans. Smart Grid, vol. 5, pp. 1654-1664, 2014.
[25] D. Shi, D. J. Tylavsky, and N. Logic, "An Adaptive Method for Detection and Correction of Errors in PMU Measurements," IEEE Transactions on Smart Grid, vol. 3, pp. 1575-1583, 2012.
[26] W. T. Li, C. K. Wen, and et al, "Location Identification of Power Line Outages Using PMU Measurements With Bad Data," IEEE Trans. Power Systems, vol. 31, pp. 3624-3635, 2016.
[27] J. Zhao, S. Wang, L. Mili, B. Amidan, R. Huang and Z. Huang, "A Robust State Estimation Framework Considering Measurement Correlations and Imperfect Synchronization," in IEEE Transactions on Power Systems, vol. 33, no. 4, pp. 4604-4613, July 2018.

[28] M. Zhou, Y. Wang, A. K. Srivastava, Y. Wu, and P. Banerjee, "Ensemble based Algorithm for Synchrophasor Data Anomaly Detection," IEEE Transactions on Smart Grid, pp. 1-1, 2018.
[29] P. Gao, M. Wang, S. G. Ghiocel, J. H. Chow, B. Fardanesh and G. Stefopoulos, "Missing Data Recovery by Exploiting Low-Dimensionality in Power System Synchrophasor Measurements," in IEEE Transactions on Power Systems, vol. 31, no. 2, pp. 1006-1013, March 2016.
[30] S. Ghiocel et al., "Phasor-measurement-based state estimation for synchrophasor data quality improvement and power transfer interface monitoring," IEEE Trans. Power Syst., vol. 29, no. 2, pp. 881–888, Mar. 2014.
[31] K. Jones, A. Pal, and J. Thorp, "Methodology for performing synchrophasor data conditioning and validation," IEEE Trans. Power Syst., vol. 30, no. 3, pp. 1121–1130, May 2015.
[32] A. van Stiphout, K. De Vos and G. Deconinck, "The impact of operating reserves on investment planning of renewable power systems," *2017 IEEE Manchester PowerTech*, Manchester, 2017.
[33] H. Li, P. Ju, C. Gan, S. You, F. Wu and Y. Liu, "Analytic Analysis for Dynamic System Frequency in Power Systems Under Uncertain Variability," in *IEEE Transactions on Power Systems*, in press.
[34] H. Li, P. Ju, C. Gan, Y. Tang, Y. Yu and Y. Liu, "Analytic Estimation Method of Forced Oscillation Amplitude Under Stochastic Continuous Disturbances," in *IEEE Transactions on Smart Grid*, in press.
[35] P. Ju, H. Li, C. Gan, Y. Liu, Y. Yu and Y. Liu, "Analytical Assessment for Transient Stability Under Stochastic Continuous Disturbances," in *IEEE Transactions on Power Systems*, vol. 33, no. 2, pp. 2004-2014, March 2018.
[36] P. Ju, H. Li, X. Pan, C. Gan, Y. Liu and Y. Liu, "Stochastic Dynamic Analysis for Power Systems Under Uncertain Variability," in *IEEE Transactions on Power Systems*, vol. 33, no. 4, pp. 3789-3799, July 2018.
[37] G. Zhang and J. D. McCalley, "Estimation of Regulation Reserve Requirement based on Control Performance Standard," in *IEEE Transactions on Power Systems*, vol. PP, no. 99, pp. 1-1.
[38] M. Bucksteeg, L. Niesen and C. Weber, "Impacts of dynamic probabilistic reserve sizing techniques on reserve requirements and system costs," *IEEE Transactions on Sustainable Energy*, vol. 7, no. 4, pp. 1408-1420, 2016.
[39] K. Dave, N. Mohan, X. Deng, R. Gorur and R. Olsen, "Analyzing techniques for increasing power transfer in the electric grid," *2012 North American Power Symposium (NAPS)*, Champaign, IL, 2012, pp. 1-6.
[40] J. Suh, D. H. Yoon, Y. S. Cho and G. Jang, "Flexible Frequency Operation Strategy of Power System With High Renewable Penetration," in *IEEE Transactions on Sustainable Energy*, vol. 8, no. 1, pp. 192-199, Jan. 2017.
[41] Zhang, Yao et al. "Impacts of Power Grid Frequency Deviation on Time Error of Synchronous Electric Clock and Worldwide Power System Practices on Time Error Correction," *Energies*,1283, Oct., 2017.

[42] Y. Zhang, X. Deng, S. You, J. Dong, W. Yu, Y. Liu, "Measurement-driven Disturbance Magnitude Estimations for Bulk Power Systems," *2019 IEEE PES GTD Grand International Conference and Exposition Asia*, Bangkok, Thailand
[43] Ling Wu, Y. Liu, Dao Zhou, Jiahui Guo and Y. Liu, "Observation of inertial frequency response of main power grids worldwide using FNET/GridEye," *2016 IEEE Power and Energy Society General Meeting (PESGM)*, Boston, MA, 2016, pp. 1-5.
[44] Y. Liu et al., "Recent developments of FNET/GridEye — A situational awareness tool for smart grid," in CSEE Journal of Power and Energy Systems, vol. 2, no. 3, pp. 19-27, Sept. 2016.
[45] Hesen Liu, Lin Zhu, Zhuohong Pan, Feifei Bai, Yong Liu, Yilu Liu, Mahendra Patel, Evangelos Farantatos, Navin Bhatt. "ARMAX-based Transfer Function Model Identification Using Wide-area Measurement for Adaptive and Coordinated Damping Control", IEEE Trans. Smart Grid, 2017, 1105- 1115.
[46] Dao Zhou, Jiahui Guo, Ye Zhang, Jidong Chai, Hesen Liu, Yong Liu, Can Huang, Xun Gui, Yilu Liu. "Distributed Data Analytics Platform for Wide-Area Synchrophasor Measurement Systems", IEEE Trans. Smart Grid, 2016, 2397- 2405.
[47] Y. Liu et al., "A Distribution Level Wide Area Monitoring System for the Electric Power Grid–FNET/GridEye," in IEEE Access, vol. 5, pp. 2329-2338, 2017.
[48] X. Deng, Y. Chen and Ying Li, "Study on the CIM based data integration platform," ISGT 2011, Hilton Anaheim, CA, 2011, pp. 1-5.
[49] Shutang You, Lin Zhu, Yong Liu, Hesen Liu, Yilu Liu, Mallikarjun Shankar, Russell Robertson, Tom King. "A Survey on Next-generation Power Grid Data Architecture", 2015 IEEE PES General Meeting, 2015, 1-5.
[50] "SERC UFLS Standard: PRC-006-SERC-02", NERC. [Online].Available at: https://www.nerc.com/pa/Stand/Reliability%20Standards/PRC-006-SERC-02.pdf
[51] "Standard BAL-001-2 – Real Power Balancing Control Performance", NERC. [Online].Available at:http://www.nerc.com/files/BAL-001-2.pdf
[52] "IEEE Recommended Practice for Emergency and Standby Power Systems for Industrial and Commercial Applications," in IEEE Std 446-1995 [The Orange Book] pp.1-320, July 3 1996.
[53] "IEEE Guide for Identifying and Improving Voltage Quality in Power Systems," in IEEE Std 1250-2011 (Revision of IEEE Std 1250-1995) , pp.1-70, March 31 2011.
[54] "IEEE Recommended Practice for Powering and Grounding Electronic Equipment," in IEEE Std 1100-2005 (Revision of IEEE Std 1100-1999) pp.1-703, May 24 2006.
[55] "Power quality. Frequency deviation for power system" in GB/T 15945-2008, 2008.
[56] "Stage one draft review of the frequency operating standard," Australian Energy Market Commission, [Online].Available at: http://www.aemc.gov.au/getattachment/241498f9-82aa-4e53-b61f-8beb370d3256/Stage-one-draft-determination.aspx.
[57] "Preview Mechanical vibration -- Torsional vibration of rotating machinery -- Part 1: Land-based steam and gas turbine generator sets in excess of 50 MW," ISO 22266-1:2009, pp.1-25, May 2009.
[58] J. Zhao, A. Goldstein, Y. Liu, "Model of parameterized PMU estimation error", 2017 IEEE PES General Meeting, Chicago, IL, 2017.
[59] J. Zhao, J. Tan, L. Wu, L. Zhan, W. Yao, Y. Liu, J. Gracia, P. Ewing, "PMU error impact on measurement-based applications", 2017 IEEE PES General Meeting, Chicago, IL, 2017.

[60] J. Zhao, L. Zhan, Y. Liu, H. Qi, J. R. Garcia, P. D. Ewing, “Measurement accuracy limitation analysis on synchrophasors”, 2015 IEEE PES General Meeting, Denver, CO, 2015.
[61] Bin Qiu, Ling Chen, V. Centeno, Xuzhu Dong and Yilu Liu, "Internet based frequency monitoring network (FNET)," 2001 IEEE Power Engineering Society Winter Meeting. Conference Proceedings (Cat. No.01CH37194), Columbus, OH, USA, 2001, pp. 1166-1171 vol.3.
[62] Zhian Zhong et al., "Power system frequency monitoring network (FNET) implementation," in IEEE Transactions on Power Systems, vol. 20, no. 4, pp. 1914-1921, Nov. 2005.
[63] “Automatic Under frequency Load Shedding Requirements”, North American Electric Reliability Corporation, available at : https://www.nerc.com/pa/Stand/Reliability%20Standards/PRC-006-3.pdf
[64] Z. Yi, W. Dong and A. H. Etemadi, "A Unified Control and Power Management Scheme for PV-Battery-Based Hybrid Microgrids for Both Grid-Connected and Islanded Modes," IEEE Tran. Smart Grid, vol. 9, no. 6, pp. 5975-5985, Nov. 2018.
[65] X. Deng, "Exploring Six-Phase Transmission Lines for Increasing Power Transfer with Limited Right of Way." Order No. 1530362, Arizona State University, Ann Arbor, 2012.
[66] D. Bian, M. Kuzlu, M. Pipattanasomporn, S. Rahman and Y. Wu, "Real-time co-simulation platform using OPAL-RT and OPNET for analyzing smart grid performance," IEEE Power & Energy Society General Meeting, Denver, CO, 2015, pp. 1-5.
[67] J. Duan, K. Zhang and L. Cheng, "A Novel Method of Fault Location for Single-Phase Microgrids," IEEE Tran. Smart Grid, vol. 7, no. 2, pp. 915-925, March 2016.
[68] D. Bian, M. Kuzlu, M. Pipattanasomporn and S. Rahman, "Analysis of communication schemes for Advanced Metering Infrastructure (AMI)," IEEE PES General Meeting | Conference & Exposition, National Harbor, MD, 2014, pp. 1-5.
[69] M. Chenine, J. Ullberg, L. Nordström, Y. Wu and G. N. Ericsson, "A Framework for Wide-Area Monitoring and Control Systems Interoperability and Cybersecurity Analysis," IEEE Tran. Power Delivery, vol. 29, no. 2, pp. 633-641, April 2014.
[70] A. Bykhovsky and J. H. Chow, “Power system disturbance identification from recorded dynamic data at the northfield substation,” Int. J. Elect. Power Energy Syst., vol. 25, no. 10, pp. 787–795, 2003
[71] T. Xia, H. Zhang, R. Gardner, J. Bank, J. Dong, J. Zuo, et al., "Wide-area Frequency Based Event Location Estimation," in 2007 IEEE Power Engineering Society General Meeting, 2007, pp. 1-7.
[72] R. M. Gardner and Y. Liu, "Generation-Load Mismatch Detection and Analysis," IEEE Tran. Smart Grid, vol. 3, pp. 105-112, 2012.
[73] D. Bian, Z. Yu,D. Shi, R. Diao, Z. Wang, "A Robust Low-Frequency Oscillation Detection and Analysis (LFODA) System with Innovative Ensemble Filtering for Real-time Grid Operation," CSEE Journal of Power and Energy Systems, accepted, 2019.
[74] W. Yao et al, "Impact of GPS Signal Loss and Its Mitigation in Power System Synchronized Measurement Devices," IEEE Trans. Smart Grid, vol. 9, no. 2, pp. 1141-1149, March 2018.
[75] W. Yao etal., "A Novel Method for Phasor Measurement Unit Sampling Time Error Compensation," IEEE Trans. Smart Grid, vol. 9, no. 2, pp. 1063-1072, March 2018.

[76] H. Song, R. Na, S. Ting and P. Xiaojun, "Study on conversion between the common models of PSD-BPA and PSS/E," 2013 IEEE 11th International Conference on Electronic Measurement & Instruments, Harbin, 2013, pp. 64-69.
[77] J. Chen, Y. Zhao, A. Goldsmith, and H. V. Poor, "Line outage detection in power transmission networks via message passing algorithms," Signals, Systems and Computers, 2014 48th Asilomar Conference, 2014, pp. 350-354.
[78] J. E. Tate and T. J. Overbye, "Line Outage Detection Using Phasor Angle Measurements," IEEE Trans. Power Systems, vol. 23, no. 4, pp. 1644-1652, Nov. 2008.
[79] H. Zhu and G. B. Giannakis, "Sparse overcomplete representations for efficient identification of power line outages," IEEE Trans. Power Syst., vol. 27, no. 4, pp. 2215–2224, Nov. 2012.
[80] J.-C. Chen, W.-T. Li, C.-K. Wen, J.-H. Teng, and P. Ting, "Efficient identification method for power line outages in the smart power grid," IEEE Trans. Power Syst., vol. 29, no. 4, pp. 1788–1800, Jul. 2014.
[81] C. Chen, J. Wang and H. Zhu, "Effects of Phasor Measurement Uncertainty on Power Line Outage Detection," IEEE Journal of Selected Topics in Signal Processing, vol. 8, no. 6, pp. 1127-1139, Dec. 2014.
[82] A., Mehebub, M, Biswaranjan, S., Siddhartha, "A New Approach of Multiple Line Outage Identification Using Phasor Measurement Unit (PMU) with Bad Data," 2018 International Conference on Current Trends towards Converging Technologies.
[83] W. Li, C. Wen, J. Chen, K. Wong, J. Teng and C. Yuen, "Location Identification of Power Line Outages Using PMU Measurements With Bad Data," IEEE Transactions on Power Systems, vol. 31, no. 5, pp. 3624-3635, Sept. 2016.
[84] D. Bian, M. Pipattanasomporn and S. Rahman, "A Human Expert-Based Approach to Electrical Peak Demand Management," in IEEE Transactions on Power Delivery, vol. 30, no. 3, pp. 1119-1127, June 2015.
[85] Z. Liang, D. Bian, X. Zhang, D. Shi, R. Diao, Z. Wang, "Optimal energy management for commercial buildings considering comprehensive comfort levels in a retail electricity market," Applied Energy, Volume 236, 2019, pp. 916-926.
[86] Y. Yan, D. Shi, D. Bian, B. Huang, Z. Yi and Z. Wang, "Small-signal Stability Analysis and Performance Evaluation of Microgrids under Distributed Control," in IEEE Transactions on Smart Grid, 2018, pp. 1-1.
[87] Z. Yi and A. H. Etemadi, "Line-to-Line Fault Detection for Photovoltaic Arrays Based on Multiresolution Signal Decomposition and Two-Stage Support Vector Machine," in IEEE Transactions on Industrial Electronics, vol. 64, no. 11, pp. 8546-8556, Nov. 2017.
[88] J. Duan, H. Xu and W. Liu, ¡°Q-learning based damping control of wide-area power systems under cyber uncertainties,¡± IEEE Transactions on Smart Grid, vol. 9, no. 2, pp. 6408-6418, 2018.
[89] D. Shi, X. Chen, Z. Wang, X. Zhang, Z. Yu, X. Wang, D. Bian, "A Distributed Cooperative Control Framework for Synchronized Reconnection of a Multi-Bus Microgrid," in IEEE Transactions on Smart Grid, vol. 9, no. 6, pp. 6646-6655, Nov. 2018.
[90] D. Bian, D. Shi, M. Pipattanasomporn, M. Kuzlu and S. Rahman, "Mitigating the Impact of Renewable Variability With Demand-Side Resources Considering Communication and Cyber Security Limitations," in IEEE Access, vol. 7, pp. 1379-1389, 2019.

[91] C. Li, W. Zhou, and Sh. Yuan. "Iris recognition based on a novel variation of local binary pattern." The Visual Computer 31.10 (2015): 1419-1429.
[92] Z. Jiang, L. Zhang, Z. Ren, Y. Chen, S. Huang, “Coupled analysis of energy flow in a multiple energy system”, 2017 IEEE Conference on Energy Internet and Energy System Integration (EI2), 26-28 Nov. 2017
[93] X. Deng, G. He, Y. Chen, W. Zhang,“CIM Leadin Based on Java Reflection Mechanism in AEMS of Shanghai Power Grid,” Automation of Electric Power System, 2007, vol.31, no.18, pp. 21-24
[94] Hesen Liu, Jiahui Guo, Wenpeng Yu, Tao Xia, Rui Sun, Matthew Gardner, Lin Zhu, Yilu Liu. “The Design and Implementation of the Enterprise Level Data Platform and Big Data Driven Applications and Analytics”, 2016 IEEE PES Transmission & Distribution Conference & Exposition, 2015.
[95] X. Lu, D. Shi and et al., "PMU assisted power system parameter calibration at Jiangsu electric power company," IEEE Power & Energy Society General Meeting, Chicago, IL, 2017, pp. 1-5.
[96] W. Yao, D. Zhou L. Zhan, Y. Liu, Y Cui, S. You and Y. Liu, “GPS signal loss in the wide area monitoring system: Prevalence, impact, and solution,” Electric Power Systems Research, vol.147, pp. 254-262, 2017
[97] X. Deng, , H. Li, W. Yu, W. Wang, Y. Liu, " Frequency Observations and Statistic Analysis of Worldwide Main Power Grids Using FNET/GridEye, " 2019 IEEE Power & Energy Society General Meeting, Atlanta, GA.
[98] J. Zhao, S. You, H. Yin, J. Tan, Y. Liu, “Data quality analysis and solutions for distribution-level PMUs”, 2019 IEEE PES General Meeting, Atlanta, GA, 2019.
[99] A. Wood and B. Wollenberg, “Power Generation Operation and Control,” 2nd ed. New York: Wiley, 1996, p. 422.
[100] T. Guler, G. Gross and M. Liu, "Generalized Line Outage Distribution Factors," in IEEE Transactions on Power Systems, vol. 22, no. 2, pp. 879-881, May 2007.
[101] ISO-NE model—transmission network map, available at: https://www.nrel.gov/docs/fy14osti/61824.pdf
[102] Tennessee Valley Authority.electric infrastructure, avaialble at: https://www.eia.gov/todayinenergy/detail.php?id=11151
[103] Y. Song, W. Wang, Z. Zhang, H. Qi and Y. Liu, "Multiple Event Detection and Recognition for Large-Scale Power Systems Through Cluster-Based Sparse Coding," IEEE Trans. Power Systems, vol. 32, no. 6, pp. 4199-4210, Nov. 2017.
[104] C. Chen, H. Yang, W. Wang, M. Mandich, W. Yao, Y. Liu, “Harmonic Transmission Characteristics for Ultra-Long Distance AC Transmission Lines Based on Frequency-Length Factor”, Electric Powre Systems Research, no. 182, 2020.
[105] N. Tong, L. Chen, W. Wang, X. Lin, Z. Li, “Local-Measurement-Based High Speed Protection for Half-Wavelength UHV Lines,” IEEE Transactions on Power Delivery, Early Access, 2020.
[106] T. Li, Y. Li, M. Liao, W. Wang, C. Zeng, “A new wind power forecasting approach based on conjugated gradient neural network”, Mathematical Problems in Engineering, vol. 2016, pp. 1-8, 2016.

[107] W. Wang, H. Yin, C. Chen, A. Till, W. Yao, X. Deng, and Y. Liu, “Frequency Disturbance Event Detection Based on Synchrophasors and Deep Learning,” IEEE Trans. Smart Grid, Early Access, 2020.
[108] Wei Li et al., "Wide area synchronized measurements and inter-area oscillation study," 2009 IEEE/PES Power Systems Conference and Exposition, Seattle, WA, 2009, pp. 1-8.
[109] W. Yao, S. You, W. Wang, X. Deng, Y. Li, L. Zhan, Y. Liu ,"A Fast Load Control System Based on Mobile Distribution-Level Phasor Measurement Unit," in IEEE Transactions on Smart Grid, vol. 11, no. 1, pp. 895-904, Jan. 2020.
[110] R. M. Gardner, J. N. Bank, J. K. Wang, A. J. Arana and Y. Liu, "Non-Parametric Power System Event Location Using Wide-Area Measurements," 2006 IEEE PES Power Systems Conference and Exposition, Atlanta, GA, 2006, pp. 1668-1675.
[111] W. Wang, J. Zhao, W. Yu and Y. Liu, "FNETVision: A WAMS Big Data Knowledge Discovery System," in 2018 IEEE Power & Energy Society General Meeting (PESGM), Portland, OR, 2018.
[112] Y. Cui, W. Wang, P. Fuhr, M. M. Rodriguez. Y. Liu, “Spatio-Temporal Synchrophasor Data Characterization for Mitigating False Data Injection in Smart Grids,” in 2019 IEEE Power & Energy Society General Meeting (PESGM), Atlanta, GA, 2019.
[113] J. Zhao, J. Tan, L. Wu, L. Zhan, W. Yao, Y. Liu, J. R. Gracia, and P. D. Ewing, "Impact of measurement errors on synchrophasor applications," in IEEE Power & Energy Society General Meeting, Chicago, IL, 2017.
[114] C. Chen, J. Wang and H. Zhu, "Effects of Phasor Measurement Uncertainty on Power Line Outage Detection," in IEEE Journal of Selected Topics in Signal Processing, vol. 8, no. 6, pp. 1127-1139, Dec. 2014.
[115] T. Becejac, P. Dehghanian, and M. Kezunovic, "Impact of the errors in the PMU response on synchrophasor-based fault location algorithms," in 2016 North American Power Symposium (NAPS), Denver, CO, USA, 2016, pp. 1-6.
[116] J. Tang, J. Liu, F. Ponci, C. Muscas, and S. Sulis, "Effects of PMU's uncertainty on voltage stability assessment in power systems," in 2011 IEEE International Instrumentation and Measurement Technology Conference, Beijing, China, 2011, pp. 1-5.
[117] C. Huang, F. Li, D. Zhou, et al, “Data quality issues for Synchrophasor applications Part I: a review,” J. Mod. Power Syst. Clean Energy, Vol. 4, N, 3, 2016, pp. 342-352.
[118] C. Huang, F. Li, D. Zhou, et al, “Data quality issues for Synchrophasor applications Part II: problem formulation and potential solutions,” J. Mod. Power Syst. Clean Energy, Vol. 4, N, 3, 2016, pp. 353-361.
[119] W. Wang, C. Chen, W. Yao, K. Sun, W. Qiu, X. Deng, Y. Liu “Synchrophasor Data Compression Under Disturbance Conditions via Cross-Entropy-Based Singular Value Decomposition,” in IEEE Transactions on Industrial Informatics.
[120] Meng Wu and L. Xie, "Online identification of bad synchrophasor measurements via spatio-temporal correlations," 2016 Power Systems Computation Conference (PSCC), Genoa, 2016, pp. 1-7.
[121] Michael A. Nielsen, “Neural Network and Deep Learning,” Determination Press, 2015.
[122] Ian Goodfellow, Yoshua Bengio, and Aaron Courville. “Deep learning,” MIT press, 2016.

[123] Y. C. Zhang, W. Yao, J. Culliss, G. Zhang, Z. Teng and Y. Liu, "Electrical field based wireless devices for contactless power gird phasor measurement," 2014 IEEE PES General Meeting | Conference & Exposition, National Harbor, MD, 2014, pp. 1-5.
[124] A. Mazloomzadeh, M. H. Cintuglu and O. A. Mohammed, "Development and evaluation of a laboratory based phasor measurement devices," 2015 IEEE Power & Energy Society Innovative Smart Grid Technologies Conference (ISGT), Washington, DC, 2015, pp. 1-5.
[125] P. Romano, M. Paolone, T. Chau, B. Jeppesen and E. Ahmed, "A high-performance, low-cost PMU prototype for distribution networks based on FPGA," 2017 IEEE Manchester PowerTech, Manchester, 2017, pp. 1-6.
[126] W. Yao, Y. Zhang, Y. Liu, M. J. Till and Y. Liu, "Pioneer Design of Non-Contact Synchronized Measurement Devices Using Electric and Magnetic Field Sensors," in IEEE Transactions on Smart Grid, vol. 9, no. 6, pp. 5622-5630, Nov. 2018.
[127] G. Wijeweera, B. Bahreyni, C. Shafai, A. Rajapakse and D. R. Swatek, "Micromachined Electric-Field Sensor to Measure AC and DC Fields in Power Systems," in IEEE Transactions on Power Delivery, vol. 24, no. 3, pp. 988-995, July 2009.
[128] F. Li and P. J. Moore, "Determination of phase sequence and voltage level of high-voltage double-circuit overhead conductors using non-contact technique," 2006 IEEE Power Engineering Society General Meeting, Montreal, Que., 2006, pp. 8 pp.-.
[129] C. A. Gerrard, J. R. Gibson, G. R. Jones, L. Holt and D. Simkin, "Measurements of power system voltages using remote electric field monitoring," in IEE Proceedings - Generation, Transmission and Distribution, vol. 145, no. 3, pp. 217-224, May 1998.
[130] C. Peng, P. Yang, X. Wen, D. Fang and S. Xia, "Design of a novel micromachined non-contact resonant voltage sensor for power distribution systems," SENSORS, 2014 IEEE, Valencia, 2014, pp. 978-981.
[131] Lapinksi and John Carroll Hill, "Apparatus and method for the measurement and monitoring of electrical power generation and transmission", U.S. Patent. Application No. US 6,771,058 B2, 2004
[132] Preston Trent Staats, "METHOD FORMONITORNG POWER AND CURRENT FLOW", U.S. Patent. Application No. US 6,714,000 B2, 2004
[133] Electric Power Research Institute, “AC transmission line reference book -200 kV and above,” Second Edition. 1982.
[134] K.K. Kaberere, K.A. Folly, A.I. Petroianu, "Assessment of Commercially Available Software Tools for Transient Stability: Experience Gained in an Academic Environment", IEEE Africon 2004, pp. 711-716, Sep. 2004.
[135] K. S. Shetye, and et al , "Systematic Determination of Discrepancies across Transient Stability Software Packages", IEEE Trans. Power Systems. vol. 31, no. 1, pp. 432-441, Jan. 2016.
[136] United States Department of Energy, "North American Energy Resilience Model", Available at: https://www.energy.gov/sites/prod/files/2019/07/f65/NAERM_Report_public_version_072219_508.pdf
[137] Kurdur, P.: "Power system stability and control" (McGraw-Hill, Inc., New York, 1994)

[138] R. Huang, et l, "Open-source framework for power system transmission and distribution dynamics co-simulation," IET Generation, Transmission & Distribution, vol. 11, no. 12, pp. 3152-3162, 24 8 2017.
[139] Q. Huang and V. Vittal, "Integrated Transmission and Distribution System Power Flow and Dynamic Simulation Using Mixed Three-Sequence/Three-Phase Modeling," IEEE Trans. Power Systems, vol. 32, no. 5, pp. 3704-3714, Sept. 2017.
[140] J. Qi, W. Huang et al, "Optimal Placement of Dynamic Var Sources by Using Empirical Controllability Covariance," IEEE Trans. Power Systems, vol. 32, no. 1, pp. 240-249, Jan. 2017.
[141] Y. Chen, C. Shen and J. Wang, "Distributed Transient Stability Simulation of Power Systems Based on a Jacobian-Free Newton-GMRES Method," in IEEE Transactions on Power Systems, vol. 24, no. 1, pp. 146-156, Feb. 2009.

Appendix

Appendix A. A Time-Domain Electromechanical Co-Simulation Framework for Power System Transient Analysis with Retainment of User Defined Models

A.1. Introduction

Time domain dynamic simulation software enables engineers and researchers to study power systems dynamics under transient conditions [134]. There are several simulation tools available including PSS/E, PSLF, PowerTech TSAT, and PowerWorld [135]. Each electric utility has its own selection for a simulation tool for dynamic analysis. As a result, one particular software has been continuously used and the corresponding power system models have been tuned and maintained over the years. For example, utilities in U.S Eastern Interconnection (EI) generally use PSS/E and utilities in Western Electricity Coordinating Council (WECC) use PSLF for transient-stability simulation.

Unfortunately, when there is a need to explore the interaction between systems whose models are built in different software, simulation cannot be performed due to the following reasons. 1) Each software has its unique simulation algorithms and modeling techniques. Even standard models might not yield the exactly same result in time domain simulation. 2) There are large numbers of user-defined models developed in particular software for specific components e.g., High Voltage Direct Current Transmission (HVDC) and Static Var Compensation (SVC). Replacing them with generic models will generate discrepancies in system dynamics. 3) Most of the user-defined models are proprietary and their source code cannot be accessed due to strict security concerns. Therefore, it is not feasible to convert power system models with user-defined models between multiple software.

To fully investigate system behaviors and perform wide-area awareness studies between interconnections or utilities, a simulation technique that is able to integrate models built in

different software is required. For example, Real-time North American Energy Resiliency Model (R-NAERM) is one of the offices of Electricity's priorities to address vulnerabilities in the North American energy system [136]. Currently, the compromised solution for whole-system simulation is to assume all out-regional systems as static [137]. It defines buses between transmission and distribution systems as interface and models of the external systems as a load or power source in each simulation step. However, for the simulation of two transmission systems with UDMs, it cannot provide a solution since the tie lines between the networks cannot be ignored.

To bridge the gap, this paper proposes a framework to accomplish concurrent running of multiple time-domain software for power system electromechanical transient stability analysis with retainment of UDMs. The main contribution is preserved user-defined models and allows maximum simulation accuracy for power system transient analysis. This co-simulation is achieved through federation, in which each simulator runs as its own process and a middleware manages the data exchange via transmission line-ties and clock synchronization between the simulators considering boundary condition. The power transfers between two simulations are exchanged in each time step via its boundary model, which reflects the actual connection in transmission/transmission co-simulation.

The effectiveness of the proposed framework is validated via PSS/E and PSLF co-simulation on Northeastern Power Coordinating Council (NPCC) system. It is the first attempt to provide a solution for co-simulation in transmission system level with different time domain dynamic simulation tools. The proposed framework eliminates the requirement of model conversion in either tool and ensures the user-defined models are retained to allow maximum accuracy.

A.2. Methodology

A.2.1. Co-simulation interface and boundary model

The dynamics of transmission networks can be represented by a set of differential and algebraic equations, thus it is feasible that a network can be simulated by dividing into multiple sub-systems and analyzing with separate simulators for transient stability analysis[138], [139]. In order to avoid divergence problems of co-simulation, the initial power flow of the transmission networks must be presented at the same operational point. Defining two transmission networks A and B that are connected via I transmission tie-lines, the injected power flow at the corresponding boundary buses $\text{bus\_}k_i$ must follow tie-line power flow transfer in time domain, which can be present as follow:

$$\boldsymbol{S}_{bus\_k_i-B}(t) = h\big(\boldsymbol{S}_{bus\_k_i-A}(t), \boldsymbol{V}_{bus\_k_i-\_A}(t)\big) \tag{A.1}$$

$$\boldsymbol{S}_{bus\_k_i-A}(t) = h\big(\boldsymbol{S}_{bus\_k_i-B}(t), \boldsymbol{V}_{bus\_k_i-B}(t)\big) \tag{A.2}$$

where t is the time index. $\boldsymbol{S}_{\text{bus\_}k_i-\text{A}}(t)$ and $\boldsymbol{S}_{\text{bus\_}k_i-\text{B}}(t)$ are the power flow at the terminals of the tie line k_i in the transmission network A and B respectively. $\boldsymbol{V}_{\text{bus\_}k_i-\text{A}}(t)$ and $\boldsymbol{V}_{\text{bus\_}k_i-\text{B}}(t)$ are the bus voltage of the tie lines k_i at the transmission network A and B sides, respectively. $h(.)$ is the power flow transfer function of the transmission line boundary model between the transmission networks.

Each individual transmission network simulator may have its own algorithm and swing buses for load flow calculation. To achieve an effective information exchange between simulators, only power flow on tie lines are exchanged during the co-simulation process where each tie-line is modeled as a constant power load. The power flow exchanges on the tie-lines are calculated by the transmission line boundary model which depends on how the transmission networks are

connected. For co-simulation of transmission networks, it is assumed that when one transmission network performs dynamic simulation in a small step Δt, the dynamic status of the other transmission networks remains constant. The changes of dynamic status in one transmission network are then propagated to the other network via the boundary models. The equation (A.3) presents the impact of a dynamic simulation step in network A from t to $t + \Delta t$ on the power flow in network B via the tie line k_i

$$\boldsymbol{S}_{bus\_k_i-B}(t+\Delta t) = h\left(\boldsymbol{S}_{bus\_k_i-A}(t), \boldsymbol{V}_{bus\_k_i-A}(t), \boldsymbol{V}_{bus\_k_i-A}(t+\Delta t)\right) \quad \text{(A.3)}$$

where $\boldsymbol{V}_{\mathrm{bus}\_k_i-\mathrm{A}}(t)$ and $\boldsymbol{V}_{\mathrm{bus}\_k_i-\mathrm{A}}(t+\Delta t)$ are the voltage at the terminals of the tie line k_i in the A before and after executing a dynamic simulation. The impact from B to A can be obtained in a similar way. The co-simulation is implemented by performing dynamic simulation alternately at A and B every time step and exchanging the power flow via all the tie-lines. Figure A. 1. Illustration of Co-simulation information exchange illustrates the basic concepts of the co-simulation of two systems A and B, which can be concluded in four steps in each time instant.

Step 1. All boundary conditional load $\boldsymbol{S}_{\mathrm{bus}_{k_i}-\mathrm{B}}(t-\Delta t)$ at B are calculated using $\boldsymbol{S}_{\mathrm{bus}\_k_i-\mathrm{A}}(t-\Delta t)$, $\boldsymbol{V}_{\mathrm{bus}\_k_i-\mathrm{A}}(t-\Delta t)$ and $\boldsymbol{V}_{\mathrm{bus}\_k_i-\mathrm{A}}(t)$ via the boundary model.

Step 2. The dynamic simulation is executed for transmission network B from $t-\Delta t$ to t with updated $\boldsymbol{S}_{\mathrm{bus}_{k_i}-\mathrm{B}}(t-\Delta t)$.

Step 3. All the boundary conditional load $\boldsymbol{S}_{\mathrm{bus}_{k_i}-\mathrm{A}}(t)$ in A are calculated using$\boldsymbol{S}_{\mathrm{bus}_k_i-\mathrm{B}}(t)$, $\boldsymbol{V}_{\mathrm{bus}\_k_i-\mathrm{B}}(t-\Delta t)$ and $\boldsymbol{V}_{\mathrm{bus}\_k_i-\mathrm{B}}(t)$ via the boundary model.

Step 4. The dynamic simulation is executed for transmission network A from t to t+Δt with updated $\boldsymbol{S}_{\mathrm{bus}_{k_i}-\mathrm{A}}(t)$.

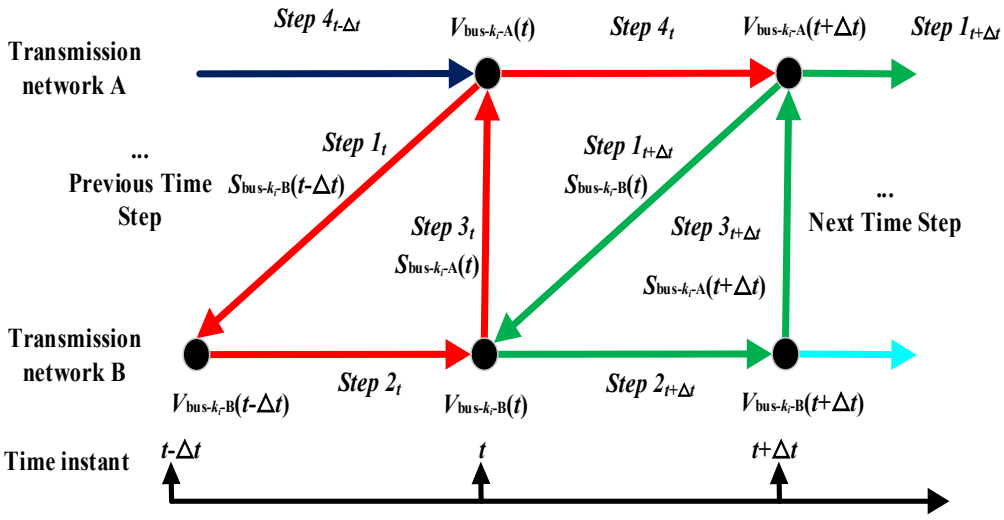

Figure A. 1. Illustration of Co-simulation information exchange

Step 5. Then it goes back to step 1 and this iterative co-simulation process is moved on.

A.2.2. Transmission line boundary models

In this subsection, PI and simple transmission line boundary models in the co-simulation framework are introduced. It is assumed that two transmission networks are connected via *n* transmission line tie lines for demonstration as shown at Figure A. 2. Transmission network A and B are connected via n tie lines. The tie lines can be modeled as either simple transmission line model or PI transmission line model. Each type of the transmission line boundary models is presented respectively as an example for power flow exchange. Assuming the dynamic simulation of A network is completed for time index t, the power flow change in A will prorogate to B network via tie lines.

A. PI transmission line boundary model

Taking the k_i PI transmission line boundary model, which is shown in Figure A. 3. PI transmission line boundary model for power flow exchange from A to B, as an example, the current can be calculated by power flow injection $\boldsymbol{S}_{\mathrm{bus\_}k_i-\mathrm{A}}(t)$ and voltage $\boldsymbol{V}_{\mathrm{bus\_}k_i-\mathrm{A}}(t)$ as

$$\boldsymbol{I}_{line\_k_i}(t) = \left(\frac{\boldsymbol{S}_{bus\_k_i-A}(t)}{\boldsymbol{V}_{bus\_k_i-A}(t)}\right)^* - \boldsymbol{V}_{bus\_k_i-A}(t) \times j\frac{b}{2} \tag{A.4}$$

where * represents conjugate transpose and b is the capacitance parameter of the PI transmission line model. The voltage $\boldsymbol{V}_{\mathrm{bus\_}k_i-\mathrm{B}}(t)$ can be calculated as

$$\boldsymbol{V}_{bus\_k_i-B}(t) = \boldsymbol{V}_{bus\_k_i-A}(t) - \boldsymbol{I}_{line\_k_i}(t) \times \boldsymbol{Z}_{line\_k_i} \tag{A.5}$$

where $\boldsymbol{Z}_{\mathrm{line\_}k_i}$ is the impedance of the tie line k_i. As discussed above, the dynamic status at the network B remains constant when the dynamic simulation is executed in network A from t to t+Δt. The power flow on tie-line k_i is determined by $\boldsymbol{V}_{\mathrm{bus\_}k_i-\mathrm{A}}(t+\Delta t)$ and $\boldsymbol{V}_{\mathrm{bus\_}k_i-\mathrm{A}}(t)$. The

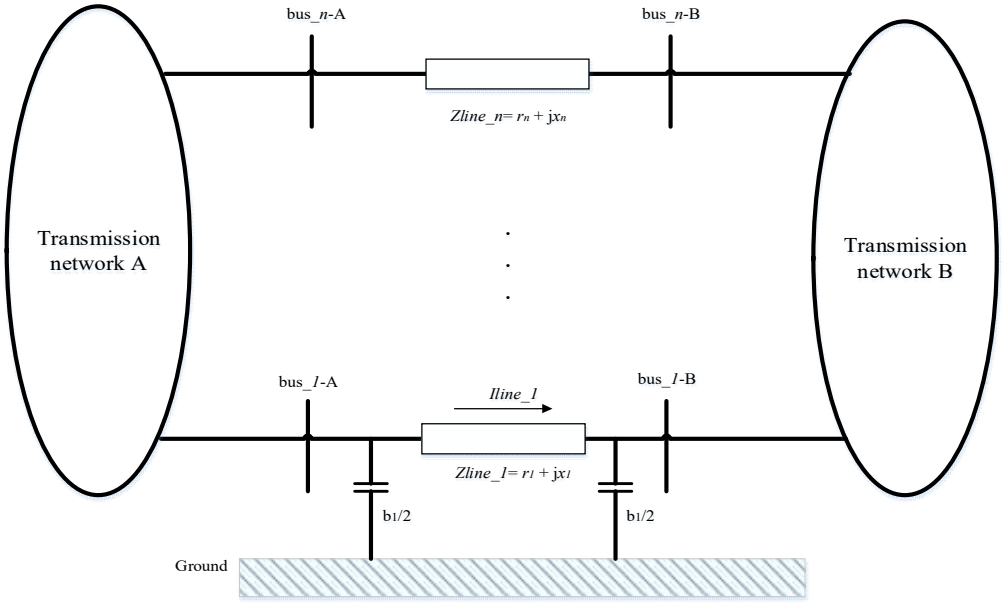

Figure A. 2. Transmission network A and B are connected via n tie lines

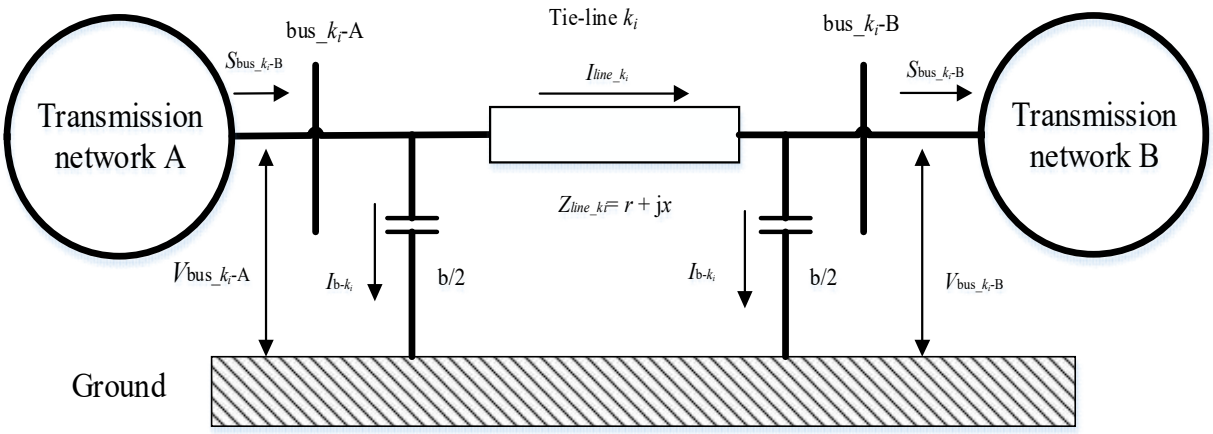

Figure A. 3. PI transmission line boundary model for power flow exchange from A to B

power flow injection at $\boldsymbol{S}_{\mathrm{bus}\_k_i-\mathrm{B}}$ caused by A network can be calculated as

$$\boldsymbol{S}_{bus\_k_i-B}(t) = \boldsymbol{V}_{bus\_k_i-B}(t) \times \left(\left(\frac{\boldsymbol{V}_{bus_{k_i}-A}(t+\Delta t) - \boldsymbol{V}_{bus_{k_i}-B}(t)}{Z} \right) - \boldsymbol{V}_{bus\_k_i-B}(t) \times j\frac{b}{2} \right) \quad \text{(A.6)}$$

Though equation (A.6), the dynamic statues change of $\mathrm{bus}\_k_i - \mathrm{A}$ in A network is propagated to $\mathrm{bus}\_k_i - \mathrm{B}$ in B network.

B. Simple transmission line boundary model

Similar to the aforementioned PI transmission line model, the current at the k_i simple model tie line can be calculated by power flow injection $\boldsymbol{S}_{\mathrm{bus}\_k_i-\mathrm{A}}(t)$ and voltage $\boldsymbol{V}_{\mathrm{bus}\_k_i-\mathrm{A}}(t)$ as

$$\boldsymbol{I}_{line\_k_i}(t) = \left(\frac{\boldsymbol{S}_{bus\_k_i-A}(t)}{\boldsymbol{V}_{bus\_k_i-A}(t)} \right)^* \quad \text{(A.7)}$$

where * represents conjugate transpose.

The voltage $\boldsymbol{V}_{\mathrm{bus}\_k_i-\mathrm{B}}(t)$ can be calculated as

$$\boldsymbol{V}_{bus\_k_i-B}(t) = \boldsymbol{V}_{bus\_k_i-A}(t) - \boldsymbol{I}_{line\_k_i}(t) \times \boldsymbol{Z}_{line\_k_i} \quad \text{(A.8)}$$

where $\boldsymbol{Z}_{\mathrm{line}\_k_i}$ is the impedance of the tie line k_i. As discussed above, the dynamic status at the network B remains constant when the dynamic simulation is executed in network A from t to t+Δt. The power flow on tie-line k_i is determined by $\boldsymbol{V}_{\mathrm{bus}\_k_i-\mathrm{A}}(t+\Delta t)$ and $\boldsymbol{V}_{\mathrm{bus}\_k_i-\mathrm{A}}(t)$. The power flow injection at $\boldsymbol{S}_{\mathrm{bus}\_k_i-\mathrm{B}}$ caused by A network can be calculated as

$$\boldsymbol{S}_{bus\_k_i-B}(t) = \boldsymbol{V}_{bus\_k_i-B}(t) \times \left(\frac{\boldsymbol{V}_{bus_{k_i}-A}(t+\Delta t) - \boldsymbol{V}_{bus_{k_i}-B}(t)}{Z} \right) \quad \text{(A.9)}$$

Though equation (A.9), the dynamic statues change of bus_k_i − A in A network is propagated to bus_k_i − B in B network as shown in Figure A. 4. Simple transmission line boundary model for power flow exchange from A to B.

A.3. Simulation Study

To validate the effectiveness and performance of the proposed framework, a co-simulation with two transmission network are implemented with PSS/E and PSLF software. A Python script based middleware is developed to control the co-simulation process and exchange data via the boundary model at each time step. The time step is 1 ms. Northeastern Power Coordinating Council (NPCC) model [140] is utilized to compare the performances of the co-simulation and PSSE-only simulation. The NPCC system is composited by a 140 bus and 206 branches and the diagram of the NPCC system is shown in Figure A. 5. The NPCC system is divided into two sub-systems, which are connected via two tie lines: 35-73 and 29-37. The two tie lines are modeled as PI model transmission line, and line parameters and voltage level are listed in Table A. 1. Summary of tie line information. The sub-system A and B in Figure A. 5. Diagram of 144-bus NPCC model for co-simulation test are modeled in PSLF and PSS/E, respectively. Bus 5 and Bus 65 are selected as observation bus for comparison. The voltage level of bus 5 and 65 are 345 kV and 115 kV respectively. The full NPCC system in PSS/E is used as a reference to validate the performance of co-simulation.

A. Generation trip

A 194 MW and -21.50 MVar generator trip is applied at Bus 61 in B subsystem at 1 second as shown in Figure A. 6. Generation trip at bus 61 in NPCC model. Both co-simulation and full PSSE model execute dynamic simulation for 10 seconds. The comparison of power flows on the tie lines, and frequency and bus voltage at the observation bus are plotted and presented from

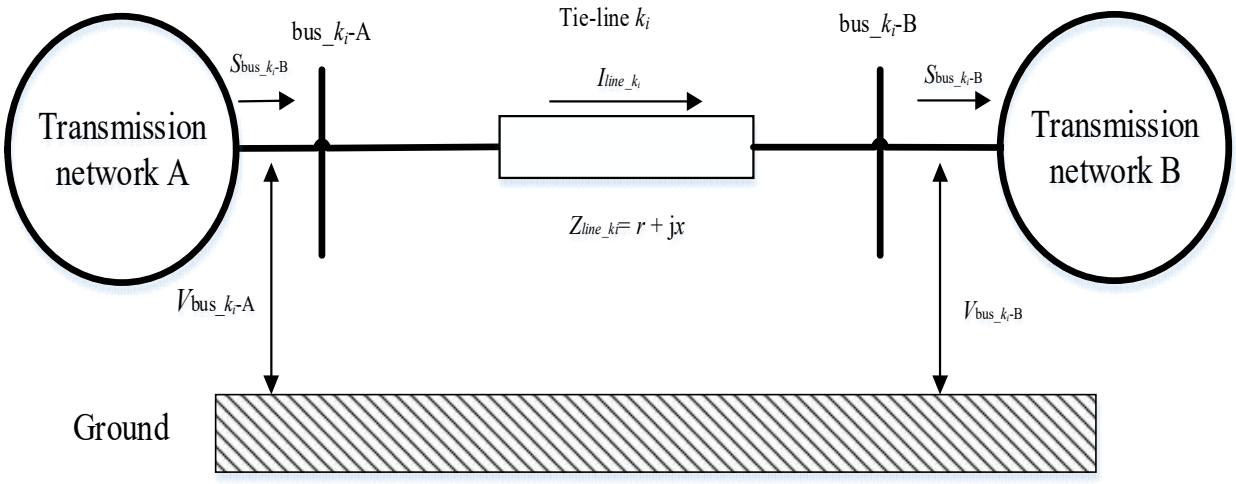

Figure A. 4. Simple transmission line boundary model for power flow exchange from A to B

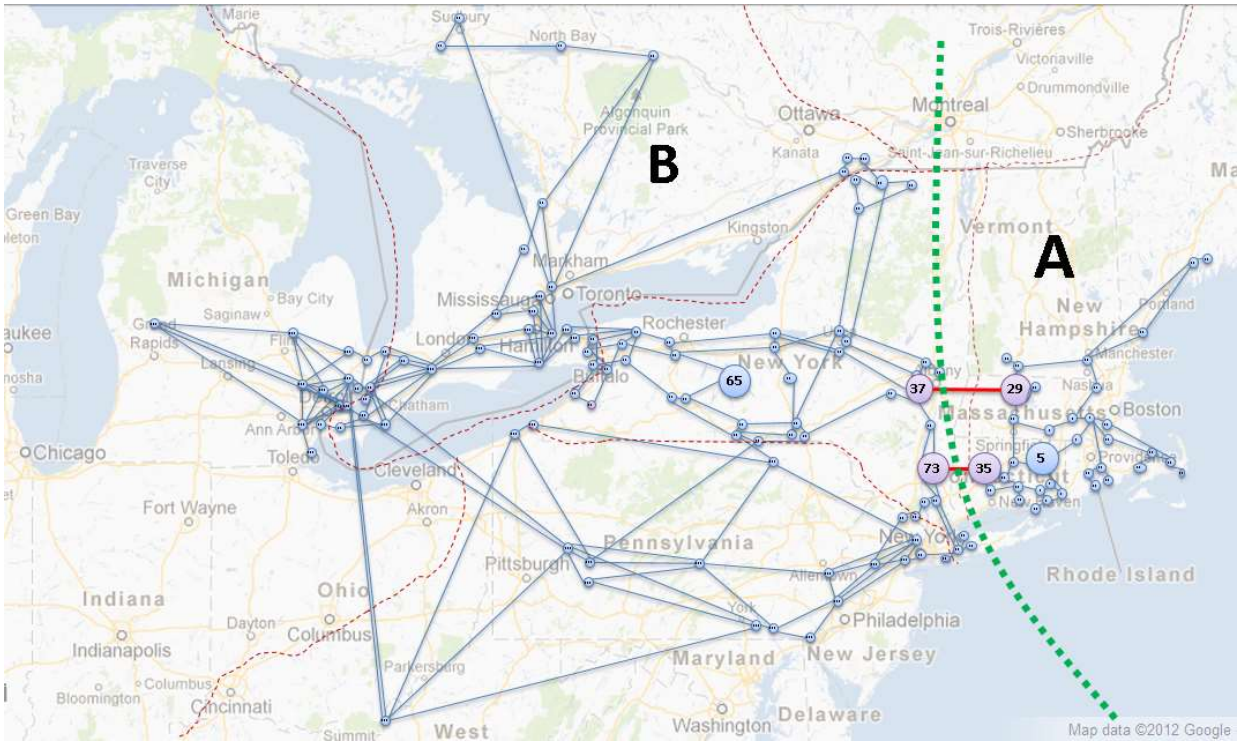

Figure A. 5. Diagram of 144-bus NPCC model for co-simulation test

Table A. 1. Summary of tie line information

Name	Line 37-29	Line 73-35
Voltage level	345 kV	345 kV
Resistant (R)	3.5×10^{-3} P.U.	2.3×10^{-3} P.U.
Reactance (X)	4.11×10^{-2} P.U.	3.63×10^{-2} P.U.
Susceptance (B)	0.7 P.U.	0.38 P.U.

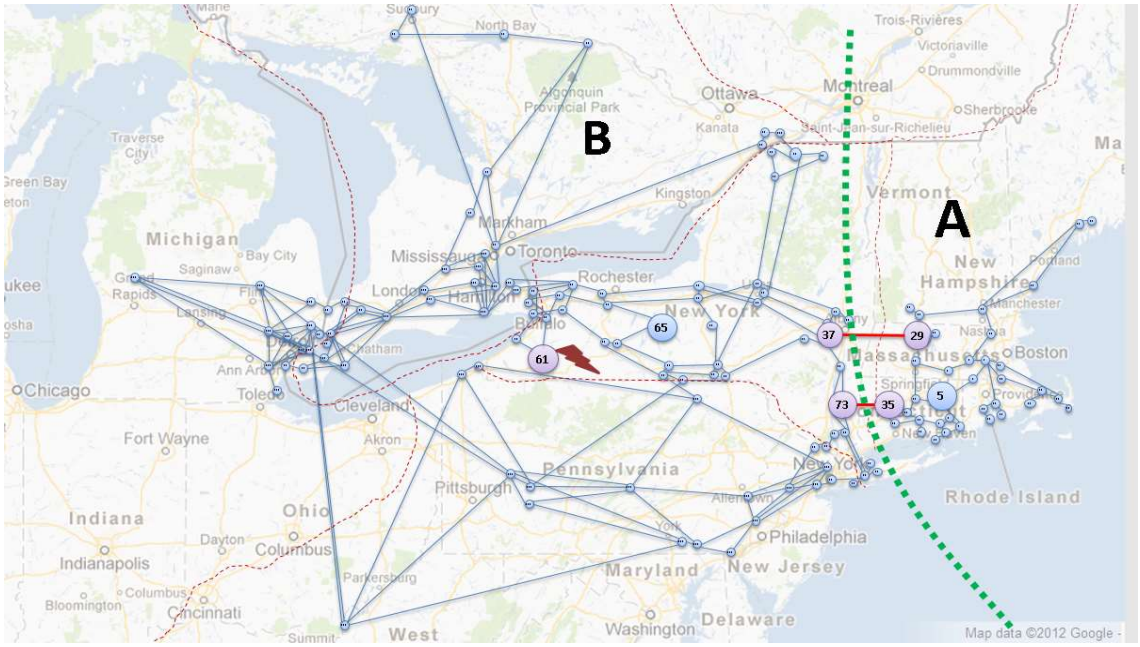

Figure A. 6. Generation trip at bus 61 in NPCC model

Figure A. 7. To Figure A. 10.

Pearson correlation coefficient, average and maximum deviation between the co-simulation and full system measurements are calculated to evaluate the co-simulation performance. The calculation windows from the disturbance applied to 10 seconds and calculation results are listed in Table A. 2. Generation trip co-simulation error evaluation. It is observed from comparison plots and calculation results that the co-simulation results are very close to the full system simulation.

B. Three-phase bus fault

A three-phase bus fault is applied at 230 kV Bus 62 in B subsystem at 1 second as shown in Figure A. 11. The bus fault is cleared at 1.1 seconds. Both co-simulation and full PSSE model execute dynamic simulation for 10 seconds. The comparison of power flows on the tie lines, and frequency and bus voltage at the observation bus are shown from Figure A. 12. to Figure A. 15.

Pearson correlation coefficient, average and maximum deviation between the co-simulation and full system measurements are calculated to evaluate the co-simulation performance. The calculation windows from the disturbance applied to 10 seconds and calculation results are listed in Table A. 3. Three-phase bus fault co-simulation error evaluation. It is observed from comparison plots and calculation results that the co-simulation results are very close to the full system simulation. It should be noticed that the maximum deviation of the two tie lines is significantly higher, which is caused by a spike when the disturbance was applied as shown in Figure A. 12 and Figure A. 13. The root cause of the spike is that it is assumed that when one subsystem executes dynamic simulation, the rest of the sub-systems hold constant in the co-simulation framework. As consequence, the status of sub-system B had rapid changes when the disturbance was applied and cleared, and the sub-system A remained at the status as before the

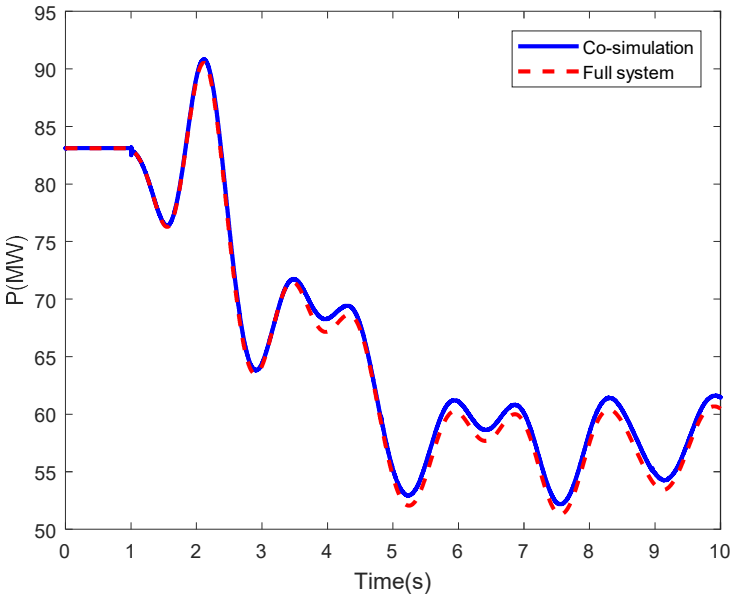

(a)

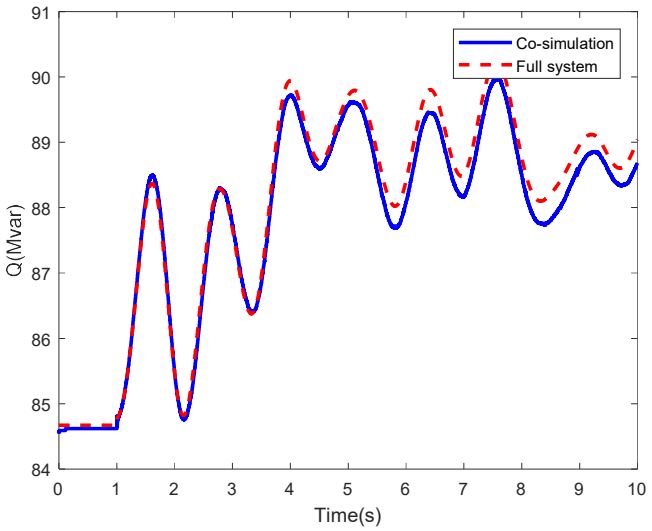

(b)

Figure A. 7. Tie line from Bus 73 to 35 power flow comparison with a generation trip: (a) active power; (b) reactive power.

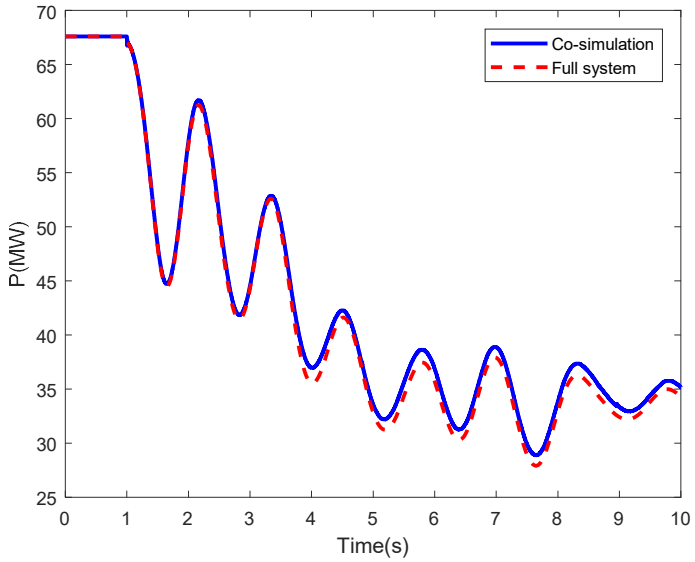

(a)

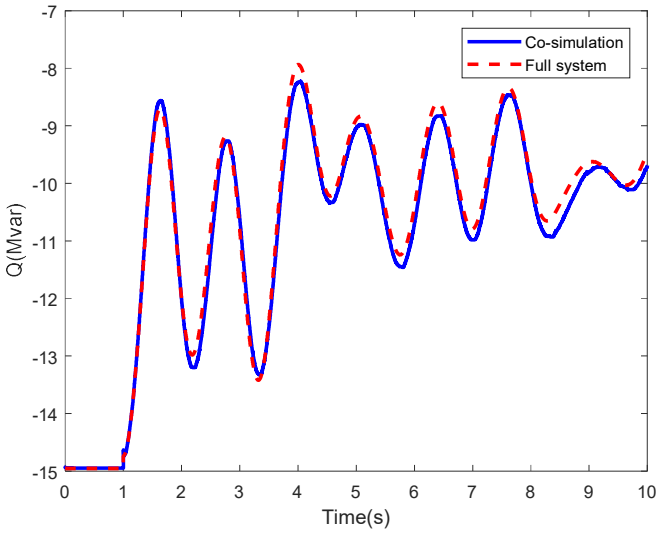

(b)

Figure A. 8. Tie line from Bus 37 to 29 power flow comparison with a generation trip: (a) active power; (b) reactive power.

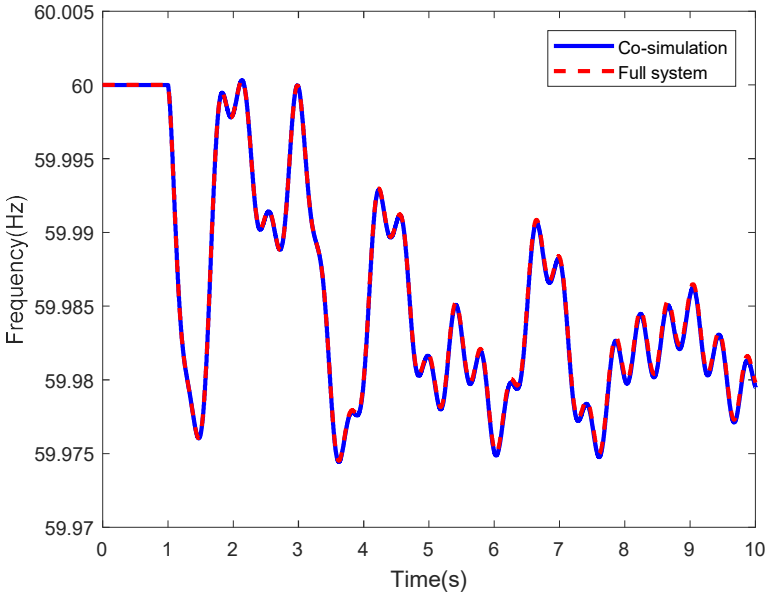

(a)

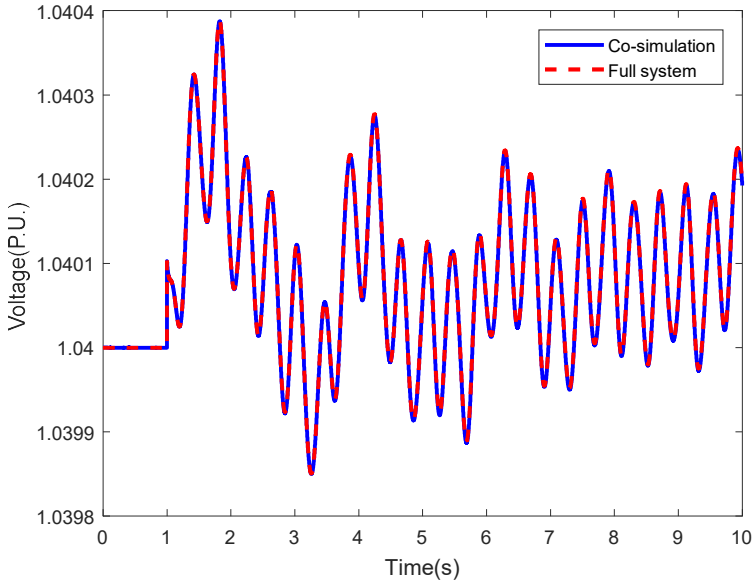

(b)

Figure A. 9. Bus 65 comparison with a generation trip: (a) Frequency; (b) Voltage.

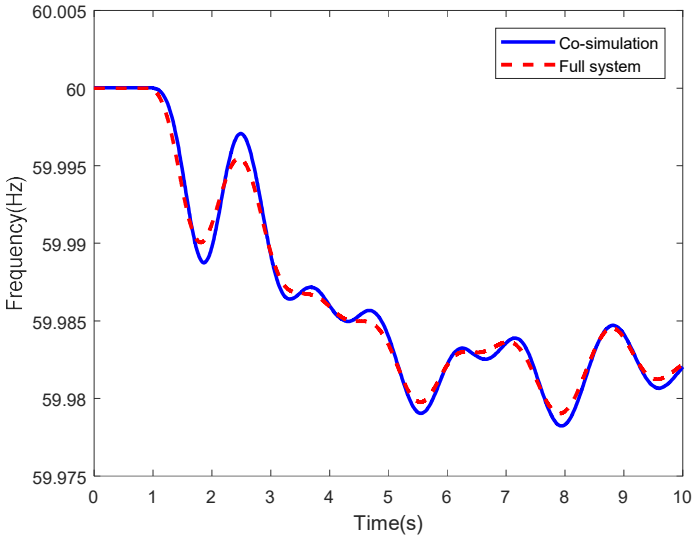

(a)

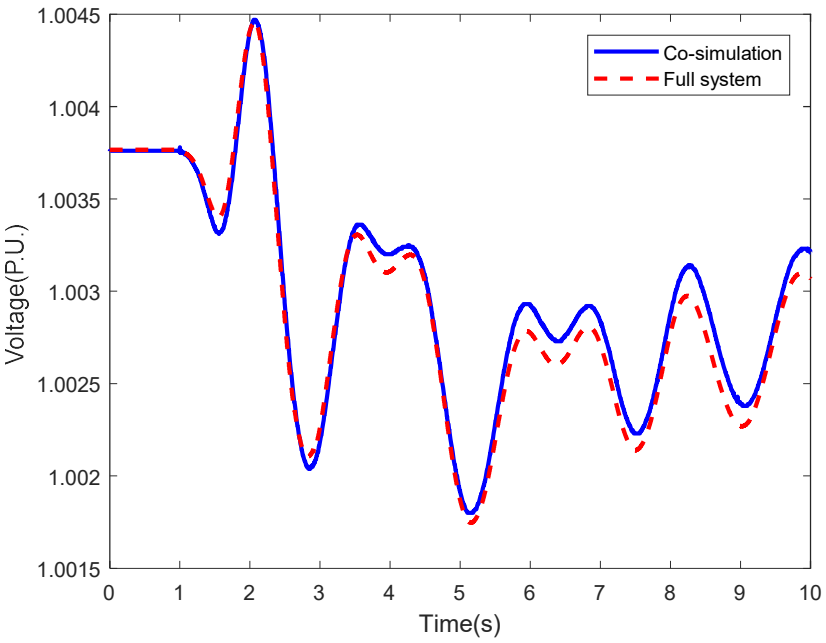

(b)

Figure A. 10. Bus 5 comparison with a generation trip: (a) Frequency; (b) Voltage.

Table A. 2. Generation trip co-simulation error evaluation

	Measurement type	Pearson correlation coefficient	Average deviation	Maximum deviation
Tie line from 73 to 35	Active power	0.9997	0.6756 MW	1.2367 MW
	Reactive power	0.9949	-0.1909 Mvar	0.4197 Mvar
Tie line from 37 to 29	Active power	0.9996	0.7612 MW	1.4544 MW
	Reactive power	0.9950	-0.1347 Mvar	0.3877 Mvar
Bus 65	Frequency	0.9999	-1.4193×10^{-4} Hz	3.5295×10^{-4} Hz
	Voltage	0.9994	-1.4149×10^{-6} P.U.	1.0276×10^{-4} P.U.
Bus 5	Frequency	0.9949	1.6123×10^{-5} Hz	1.7×10^{-3} Hz
	Voltage	0.9925	6.8620×10^{-5} P.U.	1.9182×10^{-4} P.U.

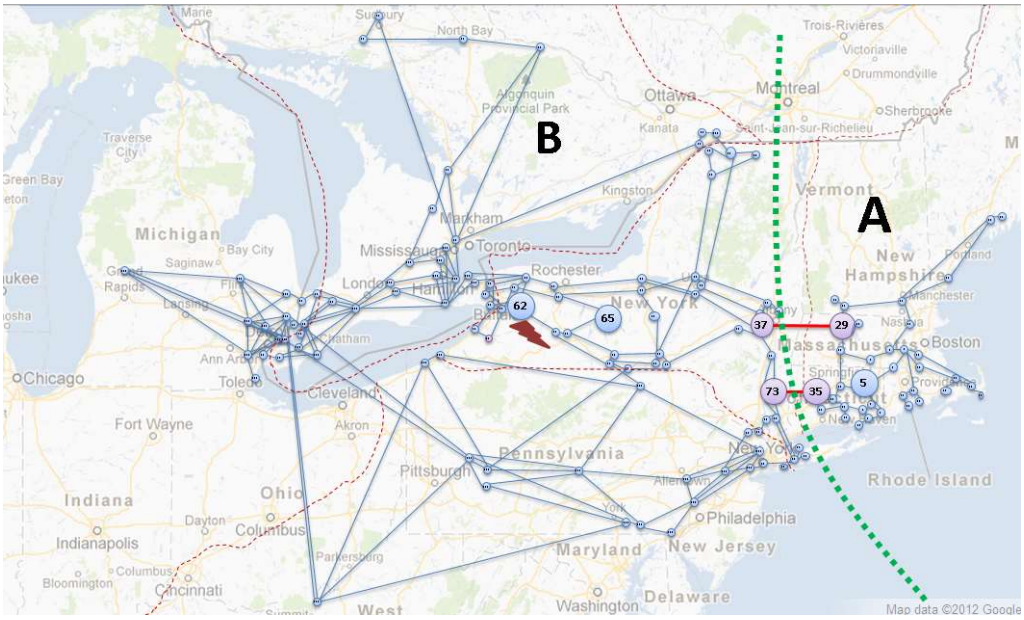

Figure A. 11. Three-phase bus fault at bus 62 in NPCC model

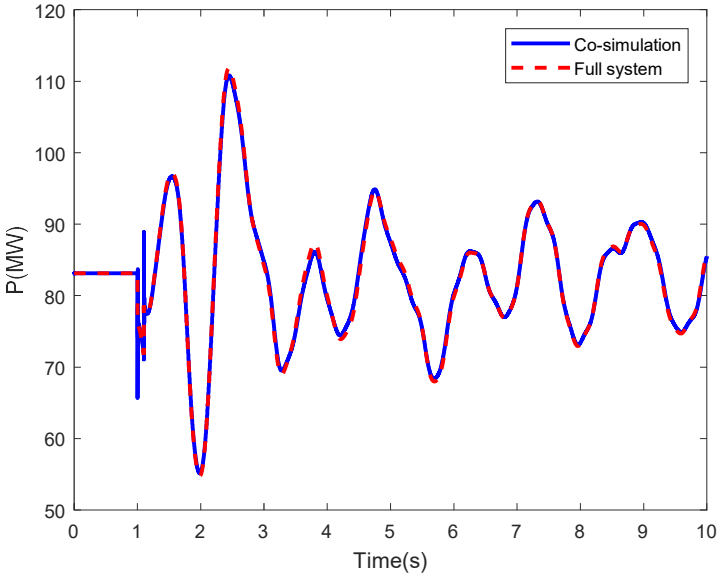

(a)

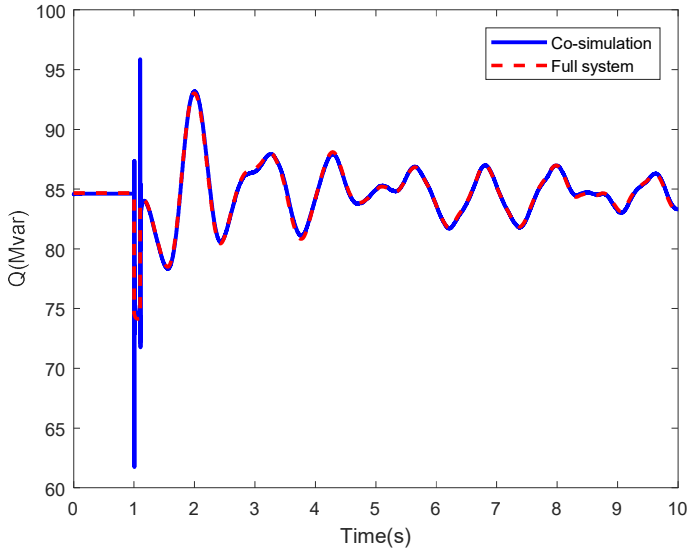

(b)

Figure A. 12. Tie line from Bus 73 to 35 power flow comparison with a three-phase bus fault: (a) active power; (b) active power.

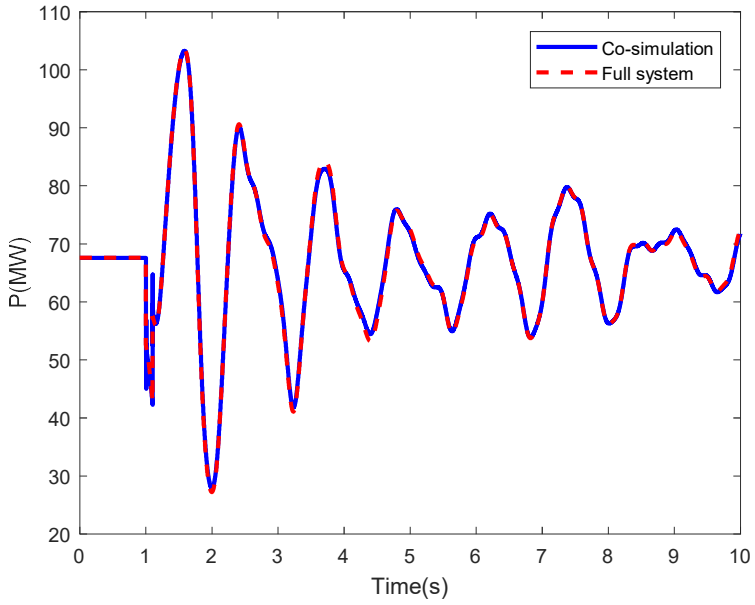

(a)

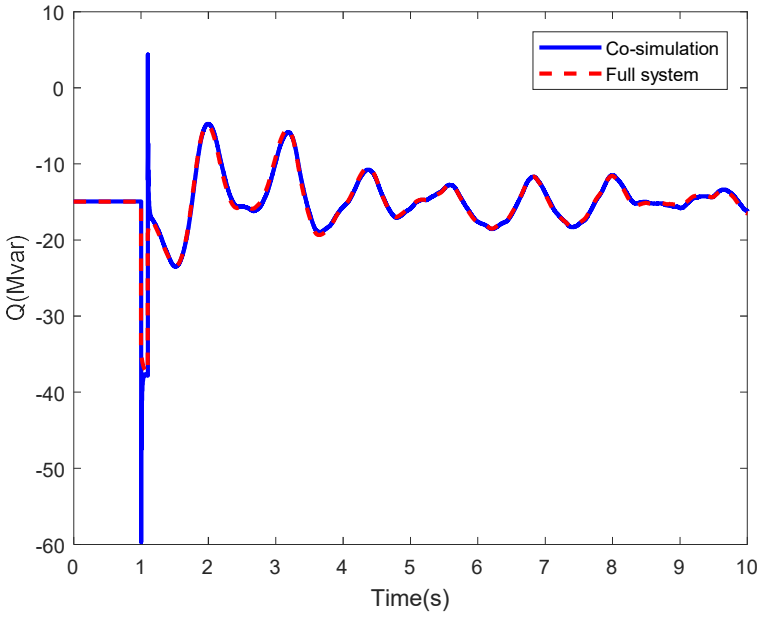

(b)

Figure A. 13. Tie line from Bus 37 to 29 power flow comparison with a three-phase bus fault: (a) active power; (b) active power.

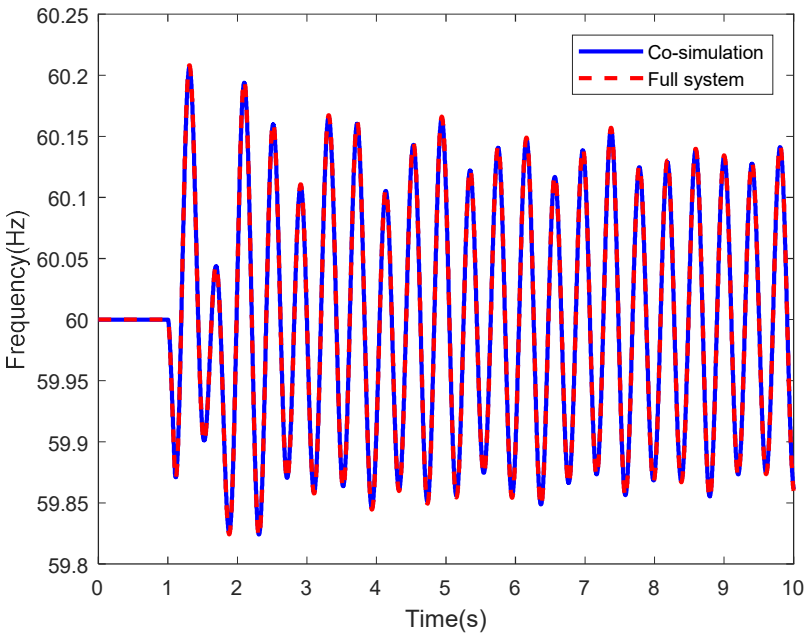

(a)

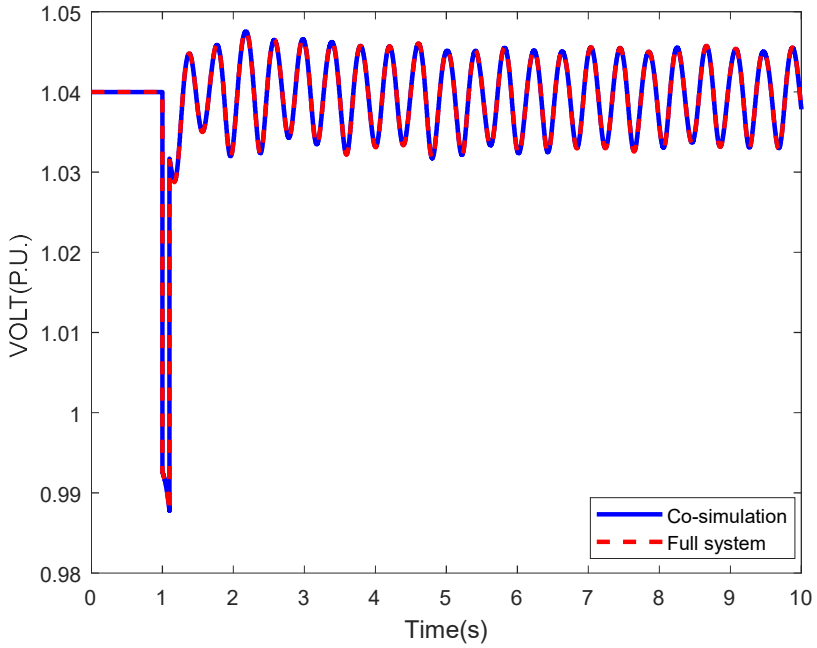

(b)

Figure A. 14. Bus 65 comparison with a three-phase bus fault: (a) Frequency; (b) Voltage.

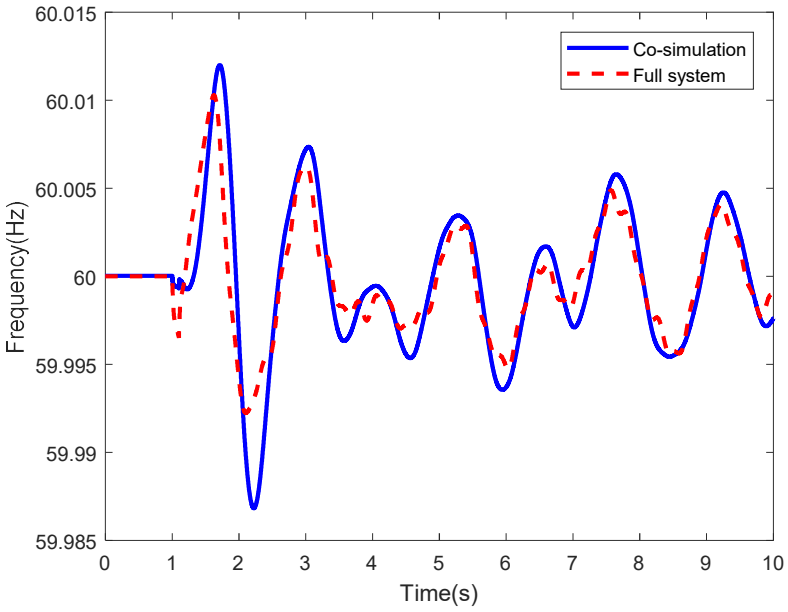

(a)

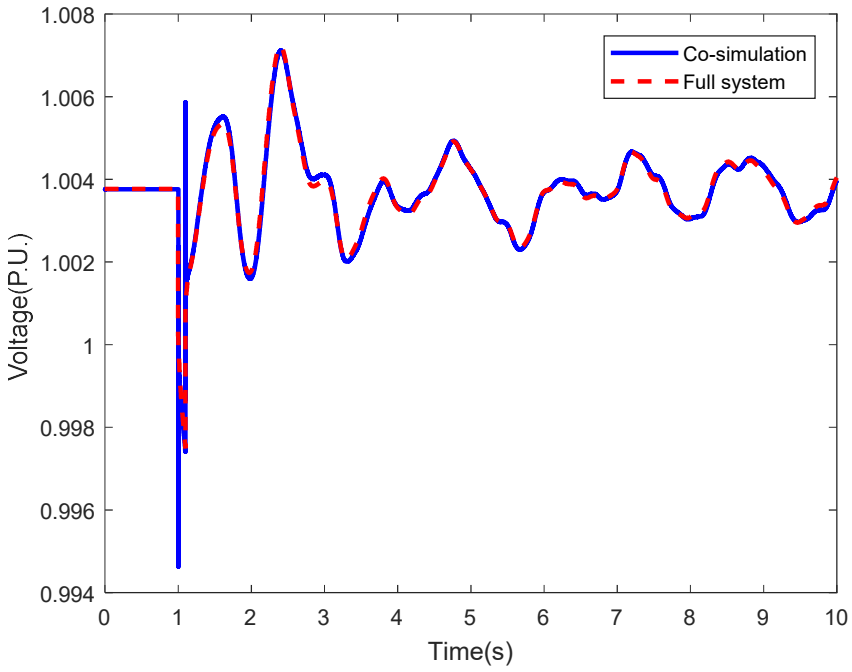

(b)

Figure A. 15. Bus 5 comparison with a three-phase bus fault: (a) Frequency; (b) Voltage.

Table A. 3. Three-phase bus fault co-simulation error evaluation

	Measurement type	Pearson correlation coefficient	Average deviation	Maximum deviation
Tie line from 73 to 35	Active power	0.9986	-2.45×10^{-2} MW	17.1565 MW
	Reactive power	0.9926	-8.1×10^{-3} Mvar	21.7055 Mvar
Tie line from 37 to 29	Active power	0.9991	8.68×10^{-3} MW	21.8424 MW
	Reactive power	0.9826	2.45×10^{-2} Mvar	41.8466 Mvar
Bus 65	Frequency	0.9978	-2.598×10^{-5} Hz	1.12×10^{-2} Hz
	Voltage	0.9835	2.5222×10^{-5} P.U.	4.39×10^{-2} P.U.
Bus 5	Frequency	0.9081	-6.7244×10^{-7} Hz	8×10^{-3} Hz
	Voltage	0.9914	5.9593×10^{-6} P.U.	8.4×10^{-3} P.U.

disturbance was applied and cleared. Then the imbalance status of the voltage at the boundary transmission line terminals lead into a power flow jump at the tie lines. The power flow deviation was corrected rapidly by the system as shown in Figure A. 12.and Figure A. 13.

C. Branch trip

A three-phase branch fault is applied at the branch from 91 to 98 in the subsystem B at 1 second as shown in Figure A. 16. The tie line parameters are listed in Table A. 4. NPCC branch 91 to 98 line parameters. The power flows of the branch from bus 91 are 423.6 MW and 139.6 Mvar respectively. The power flows of the branch from bus 98 are 445.7 MW and 17.5 Mvar respectively The Both co-simulation and full PSSE models execute dynamic simulation for 10 seconds. The comparison of power flows on the tie lines, and frequency and bus voltage at the observation bus are shown from Figure A. 17. To Figure A. 20.

Pearson correlation coefficient, average, and maximum deviation between the co-simulation and full system measurement are calculated to evaluate the co-simulation performance. The calculation windows from the disturbance applied to 10 seconds and calculation results are listed in Table A. 5. It is observed from comparison plots and calculation results that the co-simulation results are very close to the full system simulation. It should be noticed that the maximum deviation of the two tie-lines is significantly higher in most measurements, compared to the average deviation. It is caused by that the differences between co-simulation and full-PSSE model results increased after 6 seconds. The reason for the differences is that there is a status gap between subsystems in each co-simulation calculation step and the errors have been cumulated in the co-simulation process. Since this disturbance is relatively larger, compared to the generation trip and the bus fault cases, the cumulated error in the first several seconds is not obvious.

It is noted that the values of the simulation time step will impact the performance of

Table A. 4. NPCC branch 91 to 98 line parameters

Name	Line 37-29
Voltage level	345 kV
Resistant (R)	3.5×10^{-3} P.U.
Reactance (X)	4.11×10^{-2} P.U.
Susceptance (B)	0.7 P.U.

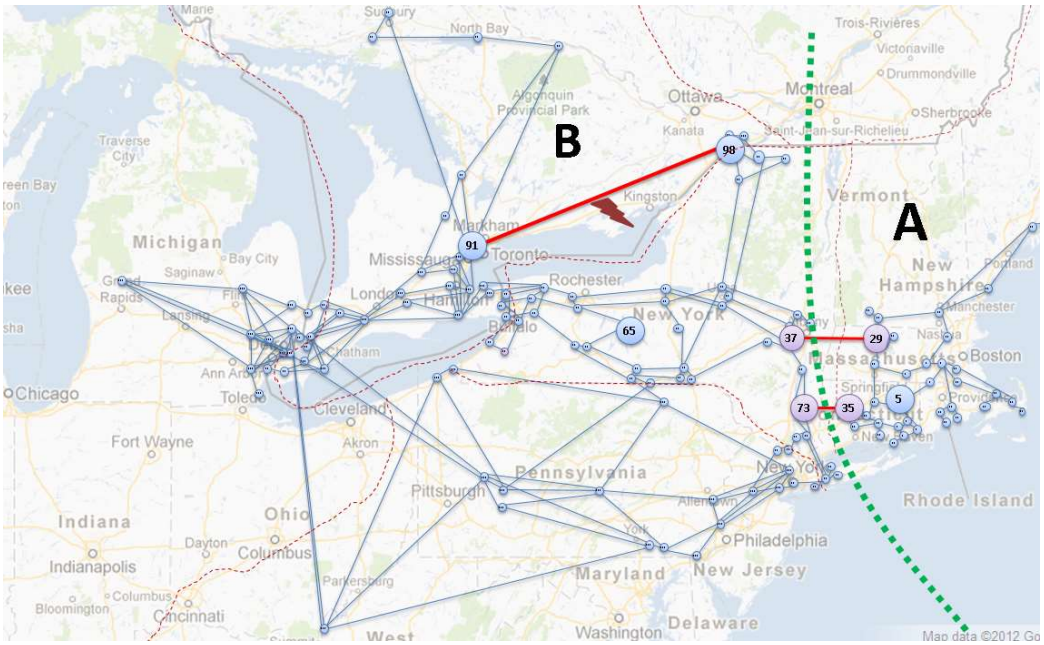

Figure A. 16. Branch trip from 91 to 98 in NPCC model

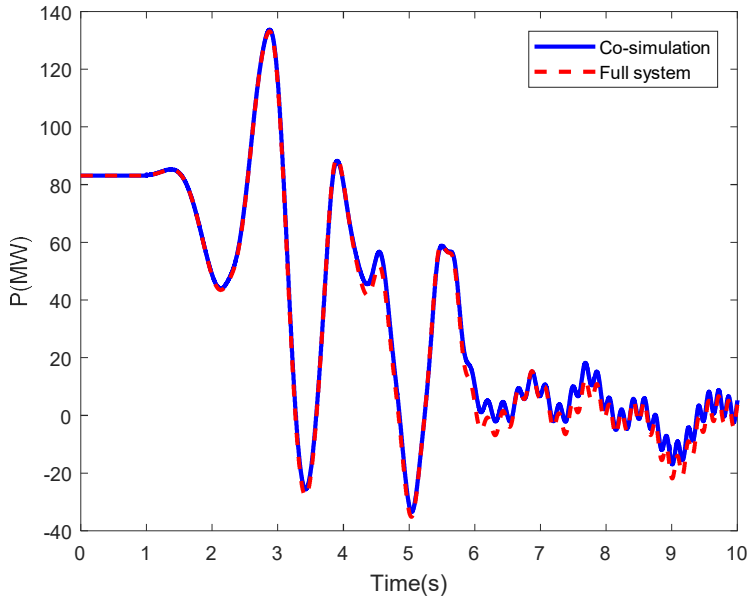

(a)

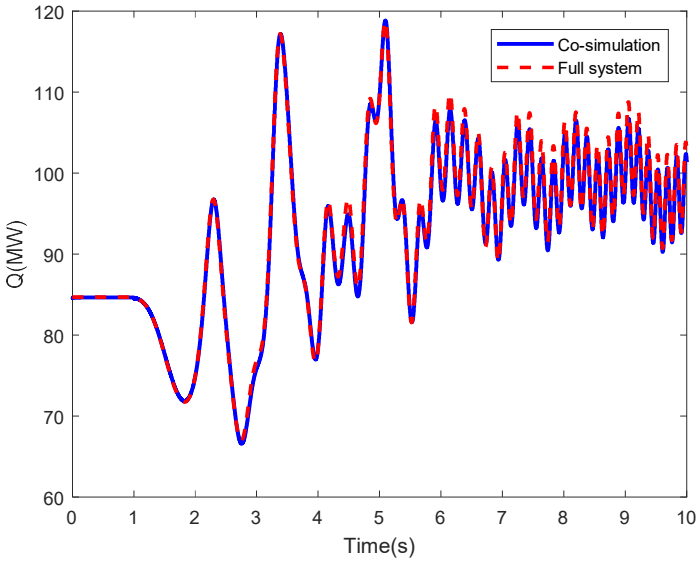

(b)

Figure A. 17. Tie line from Bus 73 to 35 power flow comparison with a branch trip: (a) active power; (b) active power.

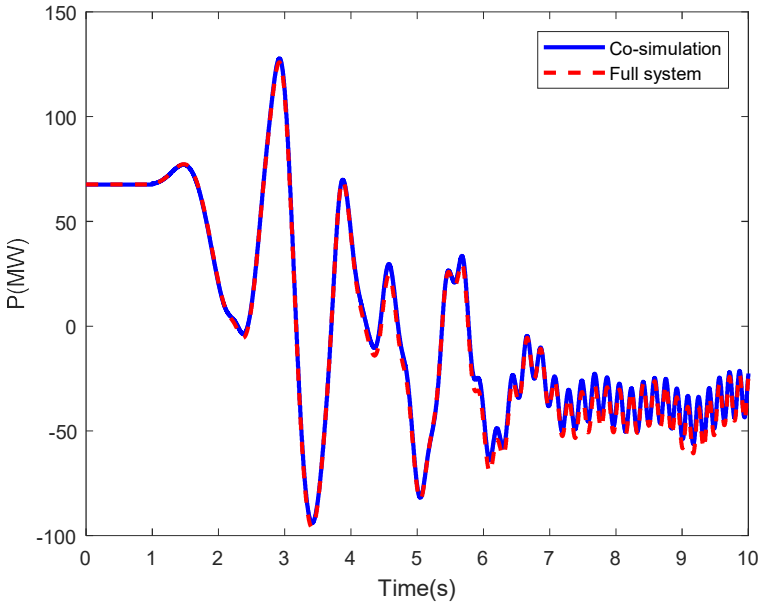

(a)

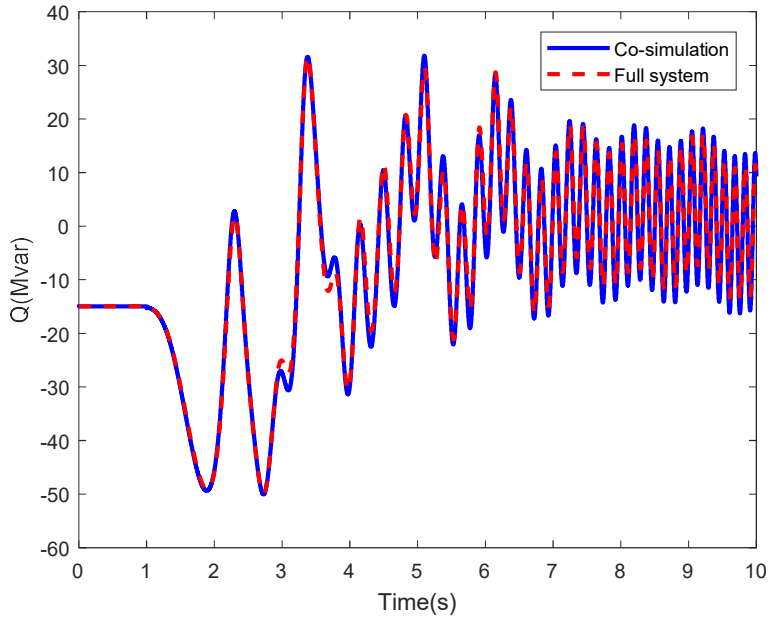

(b)

Figure A. 18. Tie line from Bus 37 to 29 power flow comparison with a branch trip: (a) active power; (b) active power.

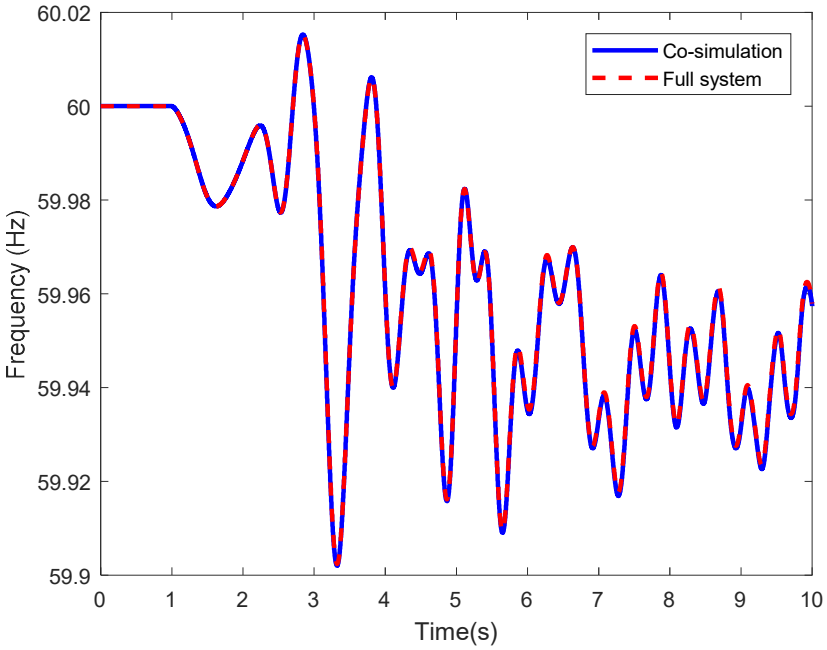

(a)

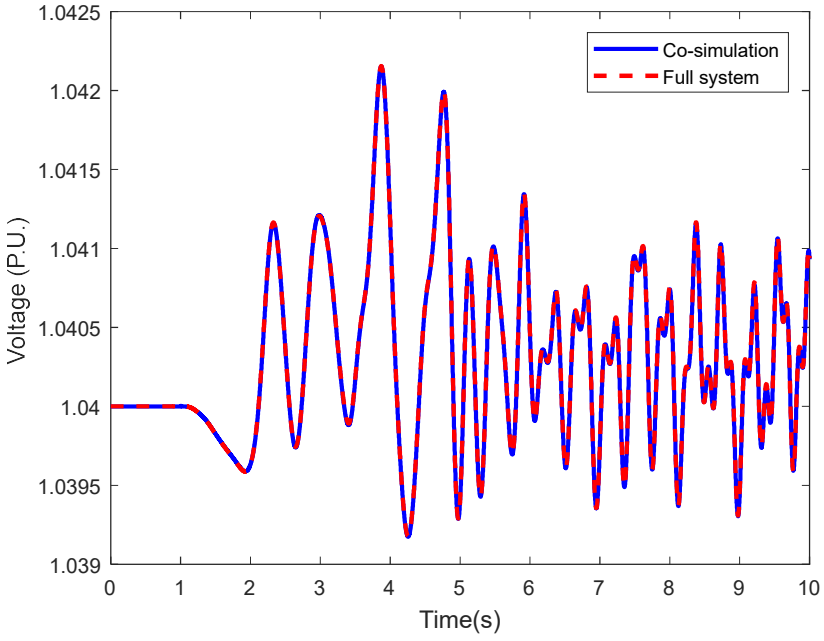

(b)

Figure A. 19. Bus 65 comparison with a branch trip: (a) Frequency; (b) Voltage.

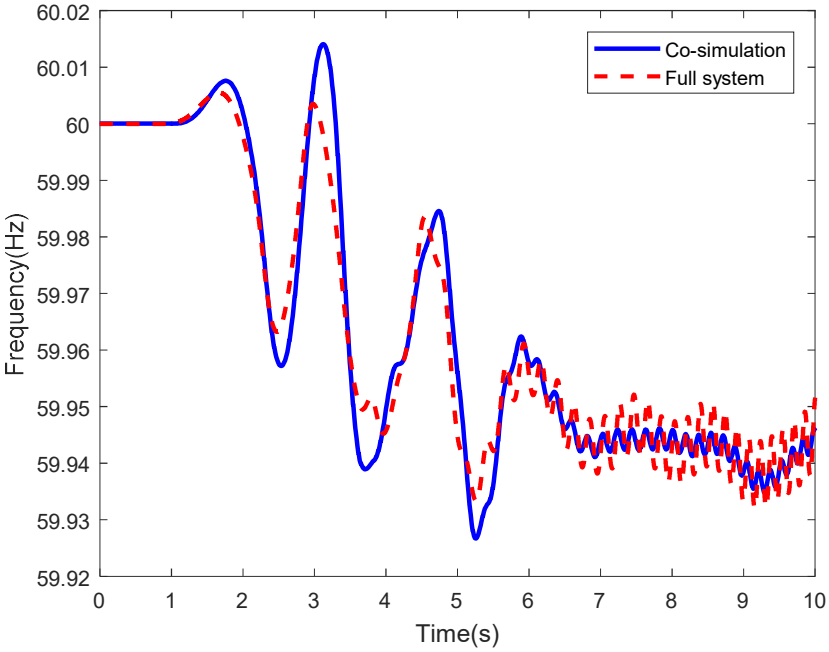

(a)

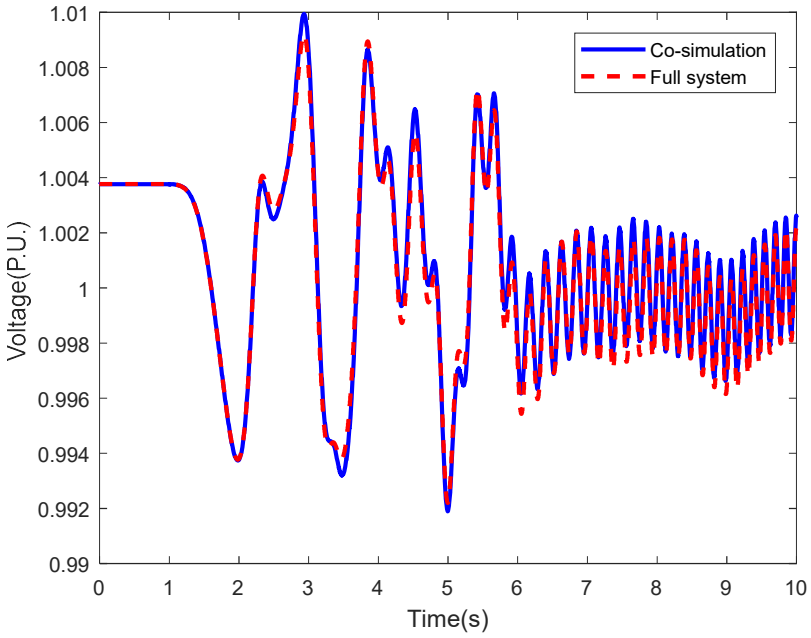

(b)

Figure A. 20. Bus 5 comparison with a branch trip: (a) Frequency; (b) Voltage.

Table A. 5. Branch trip co-simulation error evaluation

	Measurement type	Pearson correlation coefficient	Average deviation	Maximum deviation
Tie line from 73 to 35	Active power	0.9992	1.9717 MW	6.2949 MW
	Reactive power	0.9984	-0.5901Mvar	2.2178 Mvar
Tie line from 37 to 29	Active power	0.9992	2.1053 MW	7.3551 MW
	Reactive power	0.9921	-0.4442 Mvar	5.6323 Mvar
Bus 65	Frequency	0.9996	-4.1552×10^{-4} Hz	2.3×10^{-3} Hz
	Voltage	0.9988	-4.0401×10^{-6}P.U.	8.75×10^{-5} P.U.
Bus 5	Frequency	0.9731	1.3880×10^{-4} Hz	1.94×10^{-2} Hz
	Voltage	0.9932	2.1436×10^{-4} P.U.	1.1×10^{-3} P.U.

co- simulation in the aspects of the accuracy and running time. The error becomes large with an increasing time step. Moreover, When the simulation step is too large (e.g., >100ms), it will cause the simulation unable to converge. On the other hand, a small time step will increase the running time of the co-simulation. For the present time step setting of 1 ms, it will take approximately 15 minutes to run a 15-second dynamic co-simulation on the 140-bus NPCC system. Selecting a smaller time step, for example. 0.1 ms, will effectively reduce the deviation but increase simulation time significantly. Another limitation of the proposed framework is that if the disturbance location is too close to tie-lines, a spike will occur, which may cause the co-simulation unable to converge.

A.4. Simulation Study with large scale system and issues

To further validate the proposed co-simulation framework, large systems were used for testing. However, some issues were found during the test and remain an obstacle for employing the proposed framework with large systems. The issues are presented below and should be addressed in the future.

A. Creating a stable large scale system case

To create a valid and meaningful test case, the testing cases must have a stable PSS/E or PSLF only simulation case as the base case and one stable co-simulation case, which contains two subsystems. There are two ways to build a case with the requirements: (1). Split a large system and (2). Connect two independent systems with tie lines. For method (1), the subsystems in large systems are usually connected with multiple subsystems and it is difficult to find the right location to split a large system. Besides that, the split subsystems may become unstable, which can not be used in the co-simulation framework. This method has been used for the Great Britain system, Electric Reliability Council of Texas (ERCOT) system, and U.S. Eastern

Interconnection (EI) system, but none of them were split successfully. For method (2), it uses two stable systems and combines them into one model. Then connect the two systems with tie lines. The locations of the new tie lines are very critical for the joint system. If it is not selected appropriately, it may cause an unstable issue in the joint system. One safe way to connect two subsystems is that duplicate one system and connect the tie lines in similar locations of the two subsystems.

B. Converge issue in large systems

In the tests with large systems, a converge issue was found in the proposed framework. In the large system cases, when one subsystem has some changes during one simulation step, the changes are transferred to another subsystem. The changes of another subsystem will cause an opposite change at the boundary model, which is different from the case of the NPCC system. In this scenario, the changes of tie-line power flow will be amplified dramatically in several simulation steps. It can cause a system crash with small disturbances or operation points shifting. The reason for the two subsystems changing in two opposite directions is unknown. It will require a correction mechanism to rollback the simulation step and change the boundary conditions to adjust changes of the subsystems when the unstable issue happens. A correction mechanism in distributed simulation area is explained in [141] and it will be a potential improvement in the future.

A.5. Conclusion

This chapter proposes a time-domain co-simulation framework for transient stability analysis of multiple power system models which are connected via transmission lines. A middleware is developed to manage the power flow exchange and clock synchronization between simulators considering boundary model conditions. The requirement of model conversion of each

subsystem is eliminated, which guarantees user-defined models are preserved to allow maximum accuracy. The preliminary tests on PSS/E and PSLF co-simulation in the NPCC model demonstrate the validity and accuracy of the proposed framework.

Acknowledgment

This chapter is, in part, a reprint of the material in the paper: **X. Deng**, Z. Jiang, L. Sundaresh, W. Yao, W. Yu, W. Wang, and Y. Liu, " A Time-Domain Electromechanical Co-Simulation Framework for Power System Transient Analysis with Retainment of User Defined Models" in *Int. J. Electr. Power Energy Syst.,* Accepted.

Vita

Xianda Deng received his B.S. degree in electrical engineering from Guangxi University in 2005 and M.S. degree in electrical engineering from Arizona State University in 2012. He started his Ph. D study at the University of Tennessee, Knoxville, in January 2018. His research interests include wide-area power system monitoring, synchrophasor measurement applications, and data analysis for power system.